MEASUREMENT OF RESIDUAL STRESSES AND SOLVING THE INVERSE PROBLEM TO INFER DISLOCATION DISTRIBUTIONS

BY

KENNETH E SWARTZ

THESIS

Submitted in partial fulfillment of the requirements
for the degree of Master of Science in Mechanical Engineering
in the Graduate College of the
University of Illinois at Urbana-Champaign, 2016

Urbana, Illinois

Adviser:

Professor Armand Beaudoin

ABSTRACT

Residual stresses are present in the absence of external loads. All manufactured parts exhibit some degree of residual stress, which can drastically impact fatigue life. The simulation of these stresses has become exceedingly difficult as manufacturing processes have become more complex, and especially important as the desire to reduce over-designing to save on material costs has grown. As an alternative to computer simulations, a technique for measuring strains and then inferring an optimal dislocation distribution to generate the residual stress state is presented here. A continuum dislocation formulation is described in detail and optimization results are compared with a simpler discrete dislocation formulation. The ability of the optimization problem to match the full strain field is explored as regions of measurements and components of strain are withheld. The aim is to develop a technique to reduce the number of residual strain measurements necessary to fully characterize the residual stress in a manufactured part.

ACKNOWLEDGEMENTS

I would like to thank my adviser, Professor Armand Beaudoin, for his guidance through my first years of graduate school. Throughout our discussions he listened to my ideas and treated me as an equal. This created a unique environment that was very enjoyable to work in and helped me grow as a researcher in the process. I always felt as though he set my best interests as the top priority.

I would like to thank Professor Amit Acharya for his helpful discussions on continuum dislocation theory. The work in this thesis would not have been possible without theory that he has provided, and his helpful direction along the way was extremely beneficial.

I am very lucky to have worked with Professor Peter Kurath. His expertise in mechanical design was extremely helpful as I was designing load frame components. He was always willing to discuss designs and help with any problems in the lab, for which I am very grateful.

My labmates Kamalika Chaterjee and Tim Garbaciak were always very helpful. Kamalika's knowledge of x-ray experiments was especially valuable during out time at CHESS. Tim helped me learn how to set up experiments and use the necessary software for analysis. The x-ray experiments would not have been possible without the help of Chris Budrow and Peter Ko. Chris's load frame designs and ideas about machining notches into the specimen were very useful. Peter's macros were crucial during the crunch time of data collection. Professor Eric Miller and his student Dan Banco provided helpful assistance with the x-ray data processing.

I would like to thank Lance Hibbeler who has acted as a mentor to me since I worked for him as an undergraduate researcher in the summer of 2013. He was the first person who taught me how to perform proper research, and I credit many of my accomplishments since then to his guidance.

I would like to thank my parents for their constant support. They have always encouraged me to pursue education and taught me the importance of hard work and discipline from a young age.

This research was supported by the Air Force Office of Scientific Research under Contract No. FA9550-14-1-0369 and is based upon research conducted at the Cornell High Energy Synchrotron Source (CHESS), which is supported by the National Science Foundation and the National Institutes of Health/National Institute of General Medical Sciences under NSF award DMR-1332208.

TABLE OF CONTENTS

LIST OF SYMBOLS

d	Atomic Plane Spacing
D	Sample-to-Detector Distance
E	Young's Modulus
I	Area Moment of Inertia
M	Applied Moment
r	Diffraction Ring Radius
R	Error/Residual
u	Displacement
U	Distortion
$\mathbb{C}$	Constitutive Tensor
α	Primary phase in Ti-6Al-4V
$\tilde{\alpha}$	Dislocation Density
β	Secondary phase in Ti-6Al-4V
γ	Diffraction Angle
ε	Strain
θ	Scattering Angle
λ	Wavelength
ν	Poisson's Ratio
σ	Stress
χ	Incompatible Elastic Distortion

Superscripts

e	Elastic
p	Plastic
t	Total

Subscripts

b	Bending
c	Compatible
i	Incompatible
ext	External
max	Maximum
min	Minimum
pred	Predicted
r	Residual
y	Yield

CHAPTER 1: INTRODUCTION

1.1 Motivation

Stresses that remain in a body in the absence of applied loads are referred to as residual stresses. Residual stresses are present in all real materials to some degree. Despite a long history of study, residual stresses are still a challenging obstacle in manufacturing today. Any change to the temperature or physical shape of a material has the ability to create residual stress [17]. Residual stresses can have a significant impact on fatigue life, with compressive residual stresses typically increasing fatigue life and tensile residual stresses typically reducing fatigue life [19, 21, 23]. In either case, accurate knowledge of the residual stress state of a part is crucial when predicting its fatigue life. Analytical solutions are known for residual stress fields in simple geometries with simple loading conditions [16], but these solutions are limited for analyzing real engineering designs. Residual stresses may be predicted using numerical models, such as the finite element method [12], but numerical model accuracy becomes exceedingly unreliable for complex processing of engineering materials. Often it is most reliable to measure residual stresses, especially if the processing history of a part is unknown. There are both destructive, e.g. hole drilling, and non-destructive, e.g. x-ray diffraction, techniques for measuring residual stress [25]. This work seeks to provide an extension to non-destructive x-ray diffraction techniques. In short, a technique is presented to reduce the number of necessary measurements to characterize the residual stress in a part. A synchrotron x-ray source is used to measure *in situ* residual strains, which are then used in the inverse problem of determining the underlying dislocation density distribution. The complete residual stress state can then be calculated from the optimized dislocation distribution by solving two boundary value problems.

1.2 Residual Stress

A body that contains only residual stresses must still be in equilibrium. Thus, all residual stresses must balance out such that the sum of forces at each point is zero, or as it is often stated, the divergence of stress is zero at every point. Further, the residual stresses are caused by internal crystalline defects known as dislocations [17]. Plasticity and residual stresses are inherently linked by dislocations. Plastic flow occurs when a sufficient stress is applied to move dislocations through a body. Movement of these dislocations creates regions of internal tension and compression that remain even in the absence of external loads. Dislocations have an associated elastic stress field, which can be expressed in a closed-form expression for a single dislocation in an infinite plane in the plane strain condition [24]. The stress field from a single dislocation would be negligible on its own, but dislocation densities can be as high as 10^9-10^{10} mm of dislocation per cubic mm of material [7, 11], which can result in significant macro-scale stresses. The stress field resulting from an arrangement of many dislocations in an infinite plate can be determined by superposing the stress fields from each individual dislocation, since the stress fields are linearly elastic.

It would be impossible to take every dislocation into account when modeling a distribution of dislocations. It is much more feasible to consider the dislocation density throughout a body. Treating the dislocation distribution as a continuum rather than a set of discrete dislocations is justified by the large number of dislocations present in real crystalline materials [2, 11, 13, 14]. The theory of a dislocation continuum is presented in Chapter 4 and used to solve the inverse problem of inferring the dislocation density distribution throughout a body from residual strain measurements. Once the dislocation density distribution is known, the elastic strain and resulting stress can be calculated. The aim of this work is to develop a method to attain dislocation density information with a minimal number of strain measurements. The calculated residual stresses can then be used to better understand the expected material behavior, such as fatigue life.

1.3 Four-Point Bending

Four-point bending is an excellent experimental representation for the development of residual stress. A beam sufficiently loaded in four-point bending will simultaneously exhibit elastic and plastic deformation, and will render a predictable residual stress distribution upon unloading. A body that undergoes purely elastic deformation will return exactly to its initial configuration upon removal of the loads that drove the deformation. After plastic deformation, the body will not return to its initial configuration after removing the loads, and thus a permanent deformation has occurred. The deformation becomes permanent once dislocations begin to glide through a crystal structure, consequently changing the local micro-structure of the material, creating residual stresses. Drawing interpretation from Volterra dislocations, the material movement can be viewed as a redistribution of material through a process that involves cutting out material, moving it, and then welding it into place in a new location [11]. Some regions gain material leading to compressive residual stresses, while some regions lose material leading to tensile residual stresses. The combined effect of many dislocations moving in the same direction due to an externally applied load can cause parts to remain visibly warped after unloading due to the internal material movement. For example, if a coat hanger is bent slightly it will return to its original shape, however, after a certain level of deformation the bending becomes noticeably permanent.

An ideal beam loaded in four-point bending from applied forces F separated by a distance a, as pictured in Figure 1.1, has a region of uniform applied moment $M = Fa$ which behaves as pure bending. The normal stress distribution resulting from pure bending σ_b is portrayed schematically in Figure 1.2a and given by

$$\sigma_\mathrm{b}(y) = \frac{My}{I} \tag{1.1}$$

where M is the applied moment, y is the distance from the neutral axis, and I is the area moment of inertia of the cross-section [16]. This relation will not hold, however, if a large enough moment is applied such that the maximum predicted stress exceeds the yield stress of the material. The applied moment M_y that will cause yielding to first occur at the edges of the sample can be calculated by rearranging Equation (1.1) to

$$M_{\mathrm{y}} = \frac{\sigma_{\mathrm{y}} I}{y_{\mathrm{max}}} \tag{1.2}$$

where σ_{y} is the tensile yield strength of the material and y_{max} is the distance from the neutral axis to the edge of the sample. As the applied moment increases beyond this minimum value, the yield surface moves closer to the neutral axis as exemplified in Figure 1.2, which assumes a perfectly plastic material. Once plastic deformation has occurred, residual stresses will remain in the sample after the external loads are removed. The stress in the loaded state σ_{b} must be balanced by an external moment M_{ext} to enforce equilibrium. The magnitude of this external moment is calculated according to

$$M_{\mathrm{ext}} = t \int \sigma_{\mathrm{b}}(y)\, y \, \mathrm{d}y \tag{1.3}$$

where t is the sample thickness. There is an associated elastic stress distribution $\sigma_{\mathrm{ext}}(y)$, which can be calculated from Equation (1.1) using $M = M_{\mathrm{ext}}$. Removal of the applied loads will result in elastic unloading equal to the removal of $\sigma_{\mathrm{ext}}(y)$, thus the analytical solution to the residual stress σ_{r} is attained by subtracting $\sigma_{\mathrm{ext}}(y)$ from $\sigma_{\mathrm{b}}(y)$ [16], as portrayed in Figure 1.3.

1.4 Materials

Two materials were selected for this research due to their prevalence in the aerospace industry. Aluminum alloy 7075, which will be referred to as AA7075, was introduced by ALCOA in 1943 [5]. It has become very common in the aerospace industry due to its high strength to weight ratio and fatigue crack resistance [5]. Its approximate composition is given in Table 1.1 [5]. AA7075 is a desirable material choice for this study due to its relatively low Young's modulus (71.7 GPa) and high tensile yield strength (503 MPa) [3] compared to other structural materials. This combination of properties results in a high elastic strain at yield. Larger elastic strains can be measured using XRD with more relative accuracy than smaller strains by virtue of increasing the signal to noise ratio. A 9.525 mm thick plate of AA7075-T651 was purchased from McMaster Carr and used to make bending samples for the experiments discussed in Chapters 2-3. A Young's modulus of 71.7 GPa and a Poisson's ratio of 0.33 were taken as the elastic properties of AA7075 for all calculations in this work [3].

Titanium-6Al-4V, which will be referred to as Ti-64, is the most commonly used titanium alloy [15]. Many aircraft engines utilize Ti-64 in the low pressure early stages. The name stems from the alloy's composition which features 90% titanium, 6% aluminum and 4% vanadium. Ti-64 is a two-phase alloy consisting of an α-phase and a β-phase. The α-phase has a hexagonal close-packed (HCP) crystal structure, while the β phase has a body-centered cubic (BCC) crystal structure [15]. The complexity resulting from the interaction of the two phases makes Ti-64 an interesting material to study, and causes residual stress predictions to be especially difficult. A phase transition occurs at 882 °C in pure titanium, below which α-phase is present and above which β-phase is present [15]. At room temperature the β-phase may only exist in unison with α-phase. The properties of the α-phase are inherently anisotropic due to its HCP structure [15], however, an isotropic assumption may be used if a sufficient amount of grains are considered. A Young's modulus of 113.8 GPa and a Poisson's ratio of 0.342 are used for all α-phase stress calculations in this work [4]. The β-phase elastic properties cannot be directly measured at room temperature due its instability below 882 °C, thus only strains will be presented.

1.5 Preview

Chapter 2 outlines the experimental conditions as well as the theory and calculations used to determine residual strains. Chapter 3 discusses the experimental results and their validity. The inverse problem of determining optimal dislocation density distributions from residual strain measurements is discussed in detail in Chapter 4. The theory and formulations of the continuum dislocation calculation are presented, along with the inverse problem formulation and results. Chapter 4 ends with a discussion comparing the discrete and continuum approaches to the optimization of dislocation distributions.

1.6 Table

Element	Weight %
Al	87.1-91.4
Si	0.40
Fe	0.50
Cu	1.2-2.0
Mn	0.30
Mg	2.1-2.9
Cr	0.18-0.28
Zn	5.1-6.1
Ti	0.20
Others	0.15

Table 1.1 AA7075 Chemical Composition

1.7 Figures

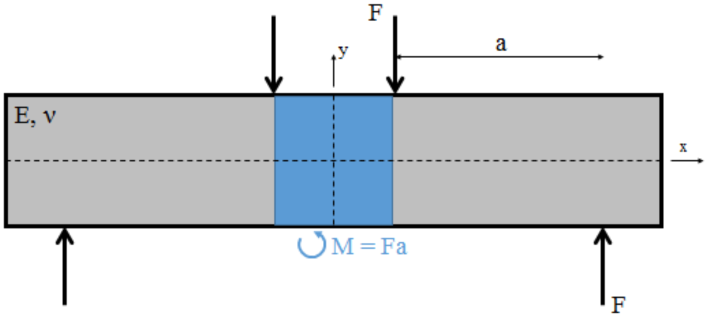

Figure 1.1 Four-Point Bending Schematic

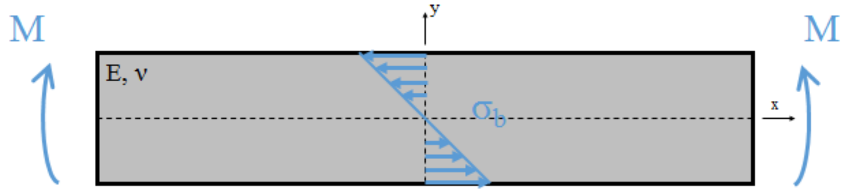

(a) Stress Distribution for Applied Moment M

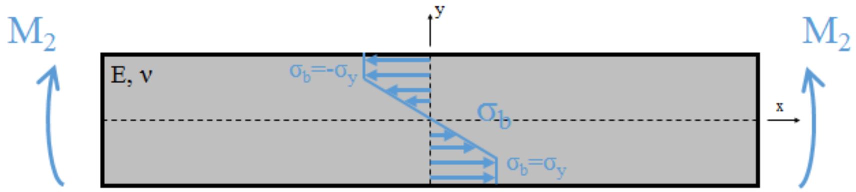

(b) Stress Distribution for Applied Moment M_2

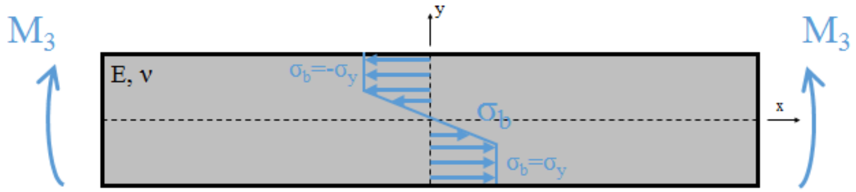

(c) Stress Distribution for Applied Moment M_3

Figure 1.2 Evolution of Yield Surface for $M_3 > M_2 > M$

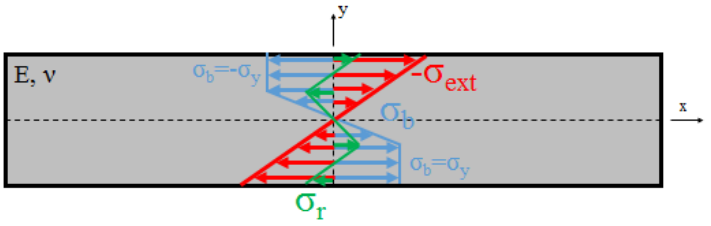

Figure 1.3 Residual Stress From Bending Schematic

CHAPTER 2: EXPERIMENTAL METHODS

2.1 X-Ray Diffraction

X-Ray diffraction (XRD) is a method used for measuring the lattice strains of a crystalline material. There are two types of XRD experiments, namely reflection geometry experiments and transmission geometry experiments. Reflection geometry experiments provide for the measurement of lattice strains of grains contained in a scattering volume very close to the surface of the sample. Transmission geometry experiments are set up to detect diffraction from x-rays transmitted through a sample, measuring lattice strains of grains throughout the body of the sample. Reflection geometry experiments have the benefit of requiring a much less powerful x-ray source than transmission geometry experiments, but lack the capability of determining internal strains. As x-ray technology has improved, transmission geometry experiments have gained the ability to non-destructively measure internal strains throughout increasingly thick samples. All XRD experiments performed in this work are transmission geometry experiments.

The basic principle used in XRD is Bragg's law, which relates wavelength of a monochromatic x-ray beam to scattering angles from a crystal lattice by

$$\lambda = 2d \sin\theta, \tag{2.4}$$

where λ is the x-ray wavelength, d is the atomic lattice spacing, and θ is the scattering angle [10]. Elastic normal strains can be measured using Bragg's law by measuring scattering angles before and after deformation, as illustrated schematically in Figure 2.1 [10]. Bragg's law for a strain-free crystal is expressed as

$$\lambda = 2d_0 \sin\theta_0, \tag{2.5}$$

where d_0 is the strain free lattice spacing and θ_0 is the strain free scattering angle. As a crystal undergoes an elastic strain the lattice spacing and scattering angle will both change. Assuming x-rays with the same wavelength were used to measure scattering angles before and after the elastic strain took place, Equations (2.4) and (2.5) can be combined such that

$$\lambda = 2d_0 \sin\theta_0 = 2d \sin\theta. \tag{2.6}$$

It follows that

$$\frac{d}{d_0} = \frac{\sin\theta_0}{\sin\theta}. \tag{2.7}$$

Substituting Equation (2.7) into the definition of a true normal strain yields

$$\varepsilon_\mathrm{n}^\mathrm{e} = \ln\frac{d}{d_0} = \ln\frac{\sin\theta_0}{\sin\theta}. \tag{2.8}$$

Shear strains cannot be measured directly, but may be calculated from various normal strain measurements. All stresses attained from XRD experiments are calculated via Hooke's law from the measured elastic strains [10].

An area detector consists of a 2D grid of pixels that measure scattered x-ray intensity. A diffraction image collected from an area detector consists of diffraction spots located around rings of varying radius. These diffraction rings may be scattered enough that individual spots can be distinguished, or filled in enough that the spots blend together to form full rings. Each grain in a polycrystalline material has a specific orientation of atomic planes. X-rays transmitting through the grain will refract off of many planes, resulting in distinct diffraction spots on the detector. The radial position r of the diffraction spot corresponds to the spacing between planes of the same family, and the azimuthal position of the diffraction spot γ corresponds to the orientation of the crystallographic family relative to the detector. As the grain size shrinks relative to the x-ray beam size, a larger number of grains are illuminated and thus a larger number of diffraction spots are present. These spots begin to overlap and at some ratio of grain size to x-ray beam size the spots overlap so much that they are indistinguishable, forming full diffraction rings. This result is often desirable if the macro-scale response of a material is preferred to the granular response.

The normal strain $\varepsilon_{\mathrm{n}}^{\mathrm{e}}$ measured by a θ shift at a point on the diffraction ring is a function of four orientation angles; γ, ω, ψ, and ϕ, which are pictured in Figure 2.2 [10]. Define a right-handed coordinate system $\boldsymbol{S}_1$, $\boldsymbol{S}_2$, and $\boldsymbol{S}_3$ centered and aligned with a sample as in Figure 2.3. Let $\boldsymbol{h}$ be a unit vector with its three components h_1, h_2, and h_3 given by

$$\begin{aligned}
h_1 &= \sin\theta\,(\sin\phi\sin\psi\sin\omega + \cos\phi\cos\omega) + \cos\theta\cos\gamma\sin\phi\sin\psi \\
&\quad - \cos\theta\sin\gamma\,(\sin\phi\sin\psi\cos\omega - \cos\phi\sin\omega) \\
h_2 &= -\sin\theta\,(\cos\phi\sin\psi\sin\omega - \sin\phi\cos\omega) - \cos\theta\cos\gamma\cos\phi\cos\psi \\
&\quad + \cos\theta\sin\gamma\,(\cos\phi\sin\psi\cos\omega + \sin\phi\sin\omega) \\
h_3 &= \sin\theta\cos\phi\sin\omega - \cos\theta\sin\gamma\cos\psi\cos\omega - \cos\theta\cos\gamma\sin\psi.
\end{aligned} \tag{2.9}$$

where γ is the angular position of a point on a diffraction ring, ω is the angle between the incident x-ray beam and the sample coordinate $\boldsymbol{S}_1$, ψ is the angle that the sample is rotated about its S_1 axis, and ϕ is the angle that the sample is rotated about its $\boldsymbol{S}_3$ axis [10]. Each experiment in this work was designed such that ω, ψ, and ϕ are held constant at $\pi/2$, 0, and 0, respectively. The components of $\boldsymbol{h}$ can consequently be reduced to

$$\begin{aligned}
h_1 &= \cos\theta\sin\gamma \\
h_2 &= -\cos\theta\cos\gamma \\
h_3 &= \sin\theta.
\end{aligned} \tag{2.10}$$

The normal strain measured by a θ shift at a point on the diffraction ring can then be related to the strain tensor components in indicial notation by [10]

$$\varepsilon_{\mathrm{n}}^{\mathrm{e}} = \varepsilon_{ij}^{\mathrm{e}}\, h_i\, h_j, \tag{2.11}$$

which expands to [10]

$$\varepsilon^{\mathrm{e}}_{\mathrm{n}} = h_1^2\,\varepsilon^{\mathrm{e}}_{xx} + 2h_1h_2\,\varepsilon^{\mathrm{e}}_{xy} + h_2^2\,\varepsilon^{\mathrm{e}}_{yy} + 2h_1h_3\,\varepsilon^{\mathrm{e}}_{xz} + 2h_2h_3\,\varepsilon^{\mathrm{e}}_{yz} + h_3^2\,\varepsilon^{\mathrm{e}}_{zz}. \tag{2.12}$$

The final three terms in Equation (2.12) can be neglected resulting in

$$\varepsilon^{\mathrm{e}}_{\mathrm{n}} = h_1^2\,\varepsilon^{\mathrm{e}}_{xx} + 2h_1h_2\,\varepsilon^{\mathrm{e}}_{xy} + h_2^2\,\varepsilon^{\mathrm{e}}_{yy}. \tag{2.13}$$

The justification for omitting the final three terms in Equation (2.12) is two-fold. The samples measured in this work are thin in the z-direction (3 mm) relative to the x- (80 mm) and y- (≈9 mm) directions. The main component of stress will be the bending component, or σ_{xx}. This combination lends itself to the plane stress condition, which says $\varepsilon^{\mathrm{e}}_{xz}$, $\varepsilon^{\mathrm{e}}_{yz}$, and $\varepsilon^{\mathrm{e}}_{zz}$ are equal to 0. In addition, the final three terms contain $\sin\theta$. The scattering angles for the experiments in this work were in the range of 0.05 to 0.2 radians. The final three terms contain a small shear strain component as well as the sine of a small angle, and consequently will be negligible in the calculation of $\varepsilon^{\mathrm{e}}_{xx}$, $\varepsilon^{\mathrm{e}}_{yy}$, and $\varepsilon^{\mathrm{e}}_{xy}$. Finally, substituting the expressions in Equation (2.10) into Equation (2.13) results in

$$\varepsilon^{\mathrm{e}}_{\mathrm{n}} = \cos^2\theta\sin^2\gamma\,\varepsilon^{\mathrm{e}}_{xx} - 2\cos^2\theta\sin\gamma\cos\gamma\,\varepsilon^{\mathrm{e}}_{xy} + \cos^2\theta\cos^2\gamma\,\varepsilon^{\mathrm{e}}_{yy}. \tag{2.14}$$

2.2 Digital Image Correlation

Digital image correlation (DIC) is a technique for measuring surface displacements on a body by comparing digital images of the body before and after deformation. A computer algorithm is used to track locations on the body to sub-pixel accuracy by locating small regions, referred to as subsets, and comparing their positions between images. The subsets can be tracked effectively if a discernible pattern is present. Random gray intensity patterns, known as speckle patterns, are often used although other options exist [18]. The ability of the method to capture a full displacement field with just a series of digital images makes DIC ideal for use in conjunction with XRD measurements. All DIC mentioned in this work refers to 2D DIC performed with a single camera.

The three main steps of the process include specimen preparation, image collection, and image analysis [18].

Specimen preparation is crucial for obtaining accurate displacement results. It is important that subsets of the speckle pattern are all somewhat different. If the subsets cannot be distinguished it is impossible for the computer to locate and compare the position of each subset between images, leading to reduced accuracy. A rough surface may be illuminated with white light to produce a speckle pattern, however, this does not always work well [18]. Black and white spray paint is a simple, yet effective method for producing the desired randomness of the pattern. A uniform pattern can cause issues with correlation as two subsets may look extremely similar. The size of the speckles, or regions of uniform gray intensity within the pattern, must correspond with the subset size. Speckles that are larger than the subset size will result in many identical subsets that are not easily tracked by the algorithm.

A reference image must be captured before any loading takes place. All subsequent images are compared with this image to determine the displacement of each subset. It is critical in 2D DIC that the optical axis of the camera is normal to the measurement surface [18]. To achieve accurate results the surface of the specimen must be flat and remain in the same plane throughout loading. Out-of-plane displacements lead to changes in magnification and consequently cause inaccuracies in the measurement [18]. Although it is not possible to remove completely, moving the camera far enough away from the specimen such that out of plane motion becomes negligible helps to improve accuracy. A combination of camera settings should be selected so that as much of the measurement surface can be as clearly focused as possible throughout the deformation. Trade offs between aperture size and focal length should be considered such that an appropriate “focused imaging volume” is selected for the experiment at hand [22].

A region of interest (ROI) where displacements are measured is defined in the reference image. The ROI is then then broken into many subsets that are tracked between images. A correlation criterion is used to compare each subset in the reference image to subsets in the deformed images. In this way the reference subsets are tracked between images to determine their displacements. The resulting displacement fields are then smoothed and differentiated to determine 2D strain fields. Further details on DIC image analysis algorithms are left to the references [18][22].

2.3 Strain Calculation

A diffraction image from a 2D area detector consists of diffracted x-ray intensity values collected on a grid of pixels. The experiment is designed such that the incident x-ray beam is normal to the detector and centered both horizontally and vertically in the grid. In reality the beam alignment will not be perfect, so diffraction images of cerium oxide powder suspended in vacuum grease were collected prior to each experiment. A python package designed for x-ray diffraction data analysis, HEXRD [6], was used to analyze these images to determine the sample-to-detector distance D as well as the location of the incident x-ray beam relative to the detector. The relationship between the diffraction ring radius r, the scattering angle θ, and the sample-to-detector distance D is given by $D = \frac{r}{\tan(2\theta)}$ and portrayed in Figure 2.4. Cerium oxide powder has known lattice spacings and thus known scattering angles for a given beam energy. The powder cannot support a stress, so the diffraction rings should be perfect circles. Measuring the radius of the rings allows the sample-to-detector distance to be calculated, and locating the center of the rings provides the incident x-ray beam location.

The particular detector used for this work was made of 2048 x 2048 pixels. A dark image was taken with a beam stop in place to record the ambient pixel readings. The intensity values recorded in the dark image were subtracted from each sample diffraction image to reduce the ambient noise in the readings. Pixels that have been over saturated in the past may give a constant reading regardless of the incoming x-ray intensity, but subtracting a dark image will remove these detector flaws from the analysis. Each pixel is assigned an x-coordinate and a y-coordinate based on a Cartesian coordinate system centered at the beam location. The Cartesian coordinates (x, y) are used to calculate polar coordinates (r, γ) according to

$$r = \sqrt{x^2 + y^2} \tag{2.15}$$

$$\gamma = \arctan\left(\frac{y}{x}\right). \tag{2.16}$$

An infinitesimal slice of an image corresponding to radial values along a single γ value is the result of x-rays diffracting from atomic planes that are normal to that γ. For actual data analysis a larger slice must be taken as an infinitesimal slice will not contain any pixels. In this work a slice consists of all points with a γ value within 0.1° of the desired γ value. A section of the slice between lower and upper radial limits is selected such that only one peak is present. The diffraction ring radius r is determined by taking the center of a two-sided Gaussian peak that is fit to this section of the slice. The relative error in the peak fit is given by

$$R_{\mathrm{rel}} = \frac{|y - \hat{y}|_2}{|y|_2} \tag{2.17}$$

where y is the recorded intensity values and $\hat{y}$ is the peak fit values. The scattering angle θ is then computed by $\theta = \frac{1}{2}\arctan\frac{r}{D}$. Scattering angles for a particular diffraction ring were determined at 360 γ values equally spaced around the diffraction ring. The elastic normal strain $\varepsilon_\gamma^{\mathrm{e}}$ can be calculated according to Equation (2.8) provided an unstressed scattering angle θ_0 is known.

An accurate values for θ_0 can be difficult to find, however, equilibrium can be leveraged to attain it. The internal stresses must be in equilibrium once the applied load is removed from the sample, i.e.,

$$\int_{y_{\min}}^{y_{\max}} \sigma_{xx}(y)\,\mathrm{d}y = 0 \tag{2.18}$$

along any vertical cross-section of the sample. An inverse problem was set up to determine θ_0 by selecting the value that would minimize the left side of Equation (2.18).

An initial guess for θ_0 is used to calculate normal strains $\varepsilon_\gamma^{\mathrm{e}}$ corresponding to each γ value. The normal strain are related to the 2D Cartesian elastic strain components $\varepsilon_{xx}^{\mathrm{e}}$, $\varepsilon_{yy}^{\mathrm{e}}$, and $\varepsilon_{xy}^{\mathrm{e}}$ according to Equation (2.14). The relative errors and amplitudes of the peak fits varied with γ due to the spottiness of the rings, and thus maximum relative error and minimum amplitude thresholds were set to determine which $\varepsilon_\gamma^{\mathrm{e}}$ values would be considered. Relating each of the qualifying $\varepsilon_\gamma^{\mathrm{e}}$ values to the Cartesian strain components results in a system of up to 360 equations for 3 unknowns. Linear least squares was used to solve the resulting overdetermined systems for $\varepsilon^{\mathrm{e}}_{xx}$, $\varepsilon^{\mathrm{e}}_{yy}$, and $\varepsilon^{\mathrm{e}}_{xy}$. Finally, the stress components are calculated from the strain components using Hooke's law for plane stress, isotropic materials given by

$$\begin{bmatrix} \sigma_{xx} \\ \sigma_{yy} \\ \sigma_{xy} \end{bmatrix} = \frac{E}{1-\nu^2} \begin{bmatrix} 1 & \nu & 0 \\ \nu & 1 & 0 \\ 0 & 0 & 1-\nu \end{bmatrix} \begin{bmatrix} \varepsilon^{\mathrm{e}}_{xx} \\ \varepsilon^{\mathrm{e}}_{yy} \\ \varepsilon^{\mathrm{e}}_{xy} \end{bmatrix} \tag{2.19}$$

where E is the Young's modulus and ν is the Poisson's ratio of the material. The integral in Equation 2.18 is then evaluated to determine if the choice of θ_0 satisfies equilibrium. Several iterations of this process are performed until a θ_0 is determined that minimizes the stress integral. The optimized θ_0 is taken as the unstressed scattering angle and is used to calculate the elastic strain components as described above. A sample of code that calculates the in-plane strain components from a single diffraction image assuming θ_0 is known is given in Appendix A.

The total strain in the sample was determined using DIC. Samples were first spray painted white before applying a mist of black paint to produce a random gray intensity pattern. A digital image was recorded before any loading, which serves as the reference image. Images taken at each subsequent load step were compared with the reference image to obtain total displacement fields, which were then differentiated to obtain total strain fields. A commercial 2D DIC code, Vic-2D 2009, was used to analyze the images for displacements and strains. At each spatial location where a diffraction image was taken, the closest DIC data point is taken as the total strain. It should be noted that there were some problems with calibrant smearing over the top part of the specimen resulting in poor correlation during image analysis. To alleviate this issue, the DIC data from the lower half of the sample was made negative and mirrored over the horizontal center line to create the expected total strain fields for the top half of the sample. The plastic strain at each data point was then calculated by subtracting the elastic strain from the total strain.

2.4 Experiment Details

Four-point bending experiments were performed to create residual stress distributions in both AA7075 and Ti-64 samples. Loads were applied such that the yield surface traveled a noticeable distance into the sample. Strain measurements were performed at the Cornell High Energy Synchrotron Source (CHESS) using x-ray diffraction techniques. Diffraction images were taken at a series of increasing load steps and then after removing the applied loads. The resulting residual strain measurements are used in Chapter 4 to solve the inverse problem of inferring dislocation density distributions. Similar work has been performed using energy dispersive x-ray diffraction to measure *in situ* bending strains before and after yielding in Titanium-6Al-4V samples [9].

2.4.1 Aluminum 7075 Experiment

A simple rectangular beam sample was cut from a plate of AA7075. The dimensions of the sample were 80 mm × 9.525 mm × 3 mm. A screw load frame, which is pictured with the sample in place in Figure 2.5, was used to load the sample in 4-point bending. Load steps were determined by turning the actuation screw by a set amount. Diffraction images were collected at five load steps; before loading, after 1 turn of the screw, after 2 total turns of the screw, after 3 total turns of the screw, and after removing the applied load. At each load step a single diffraction image was taken at 205 spatial locations, consisting of 5 locations in the x-direction with a spacing of 3 mm, and 41 locations in the y-direction with a spacing of 0.25 mm. The beam energy used for this sample was 47 keV. The incident x-ray beam was 2 mm wide in the x-direction and 0.2 mm tall in the y-direction. A summary of the experimental conditions is given in Table 2.1.

2.4.2 Titanium-6Al-4V Experiment

Samples of Ti-64 were machined out of a rolled plate. The base sample dimensions were 80 mm × 7.44 mm × 3 mm. This sample was different from the AA7075 sample, however, in that it had two semi-circle notches of radius 1.25 mm machined out of the top and bottom of the sample at the horizontal midpoint. A different load frame was used for this sample, seen with the sample in Figure 2.7, that was equipped with a torsion motor and a load cell. Diffraction images were taken at 4 load steps; before loading, at 1000 N of applied force, at 2000 N of applied force, and after removing the applied force. At each load step diffraction images were taken at 533 spatial locations consisting of 13 locations in the x-direction with a spacing of 1 mm and 41 locations in the y-direction with a spacing of 0.2 mm. The beam energy used for this sample was 42 keV. The incident x-ray beam was 2 mm wide in the x-direction and 0.2 mm tall in the y-direction. A summary of the experimental conditions is given in Table 2.1.

2.5 Summary

AA7075 and Ti-64 samples were loaded in four-point bending past the point of yield and then relaxed. Residual strain measurements were performed at CHESS using a monochromatic beam along with a 2D area detector. X-ray scattering angles were measured to determine *in situ* elastic strains before and after plastic deformation took place. Diffraction images were taken at a series of points to create a 2D map of the strain field at a series of load steps. HEXRD was used to determine the beam position relative to the detector as well as the sample-to-detector distance. Two-sided Gaussian peak fits were used determine diffraction ring radii r, from which scattering angles θ were computed in conjunction with the sample to detector distance. Normal strains were computed using the scattering angle of a diffraction ring along with a reference scattering angle θ_0. The reference scattering angle was determined by solving an inverse problem that required stresses in the sample to be in equilibrium. The normal strains corresponding to several diffraction vectors $\varepsilon^{\mathrm{e}}_{\gamma}$ were computed and related to the three 2D strain components, $\varepsilon^{\mathrm{e}}_{xx}$, $\varepsilon^{\mathrm{e}}_{yy}$, and $\varepsilon^{\mathrm{e}}_{xy}$, via Equation (2.14). A least squares analysis was used to solve the overdetermined system for the strain components, which were related to the stresses by the plane stress, isotropic Hooke's law. The same components of total strain were determined using DIC, and the plastic strain components were determined using the relation $\varepsilon^{\mathrm{p}} = \varepsilon^{\mathrm{t}} - \varepsilon^{\mathrm{e}}$.

2.6 Table

Sample	AA7075	Ti-64
Number of Data Points (x, y)	205 (5, 41)	533 (13, 41)
x-spacing	3 mm	1 mm
y-spacing	0.25 mm	0.2 mm
beam energy	47 keV	42 keV
beam width (x-direction)	2 mm	2 mm
beam height (y-direction)	0.2 mm	0.2 mm

Table 2.1 Experiment Details

2.7 Figures

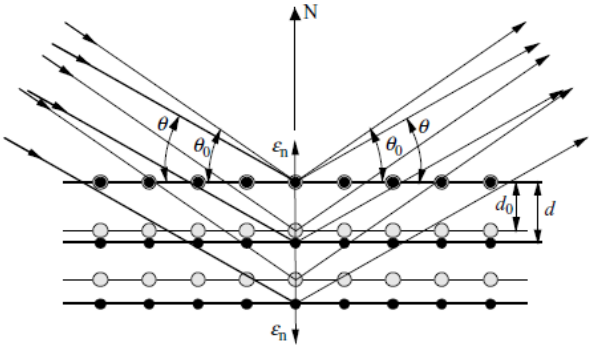

Figure 2.1 Schematic of Bragg's Law [10]

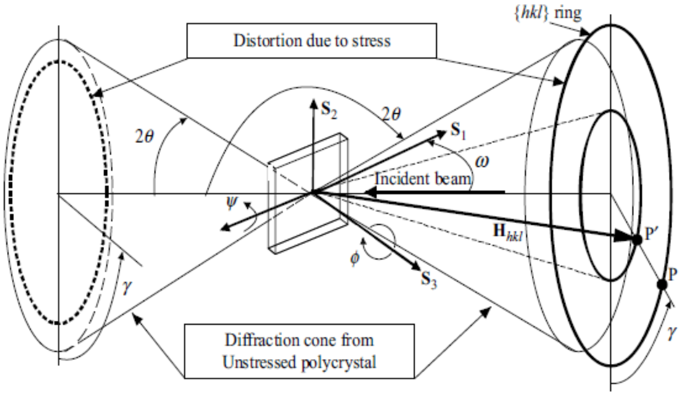

Figure 2.2 Schematic of XRD Angles [10]

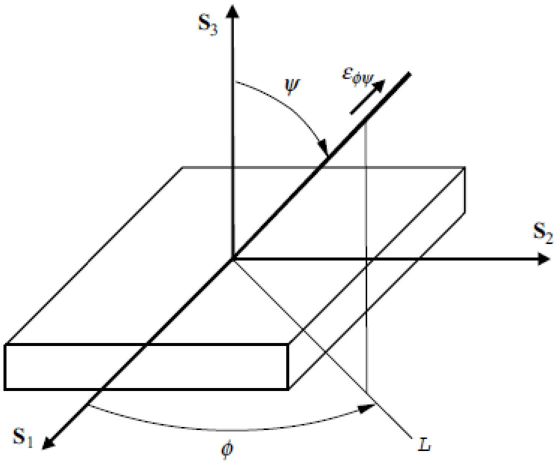

Figure 2.3 Schematic of Sample Coordinate System [10]

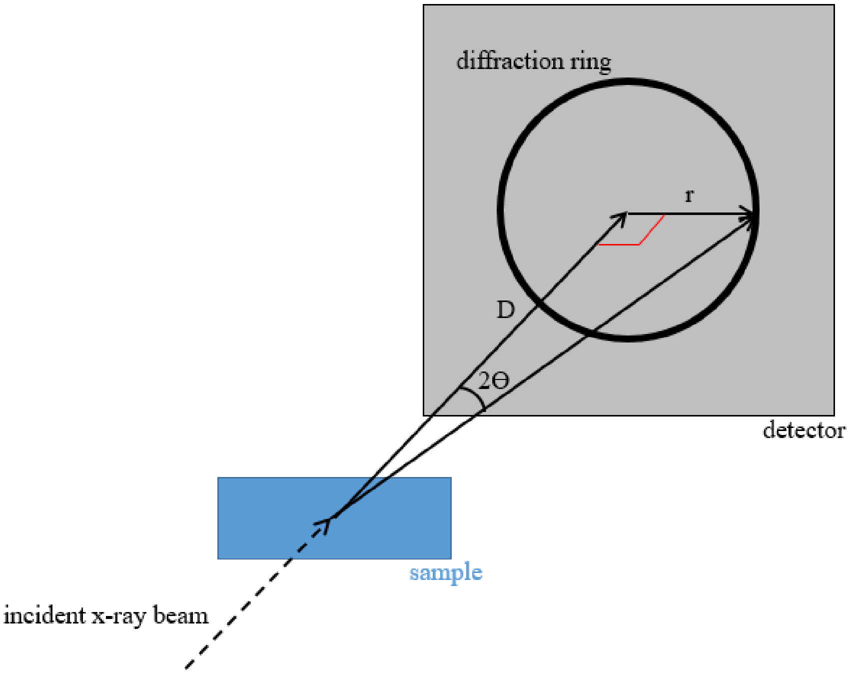

Figure 2.4 Detector Distance Calculation Schematic

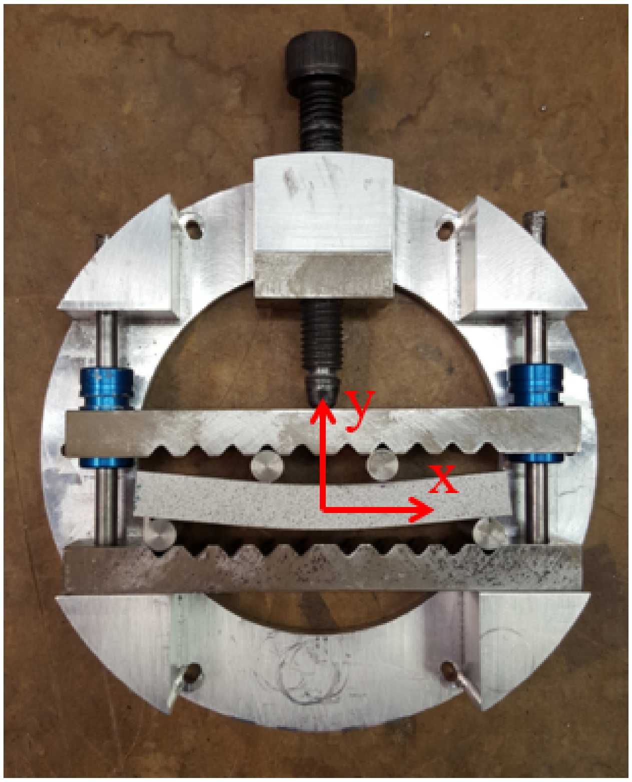

Figure 2.5 Load Frame Used With AA7075 Samples

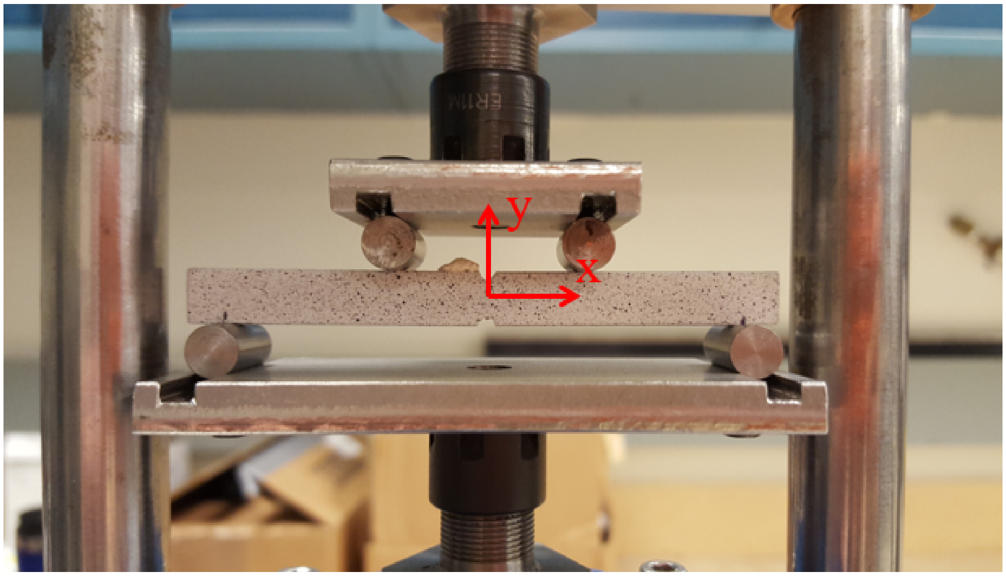

Figure 2.6 Ti-64 Sample

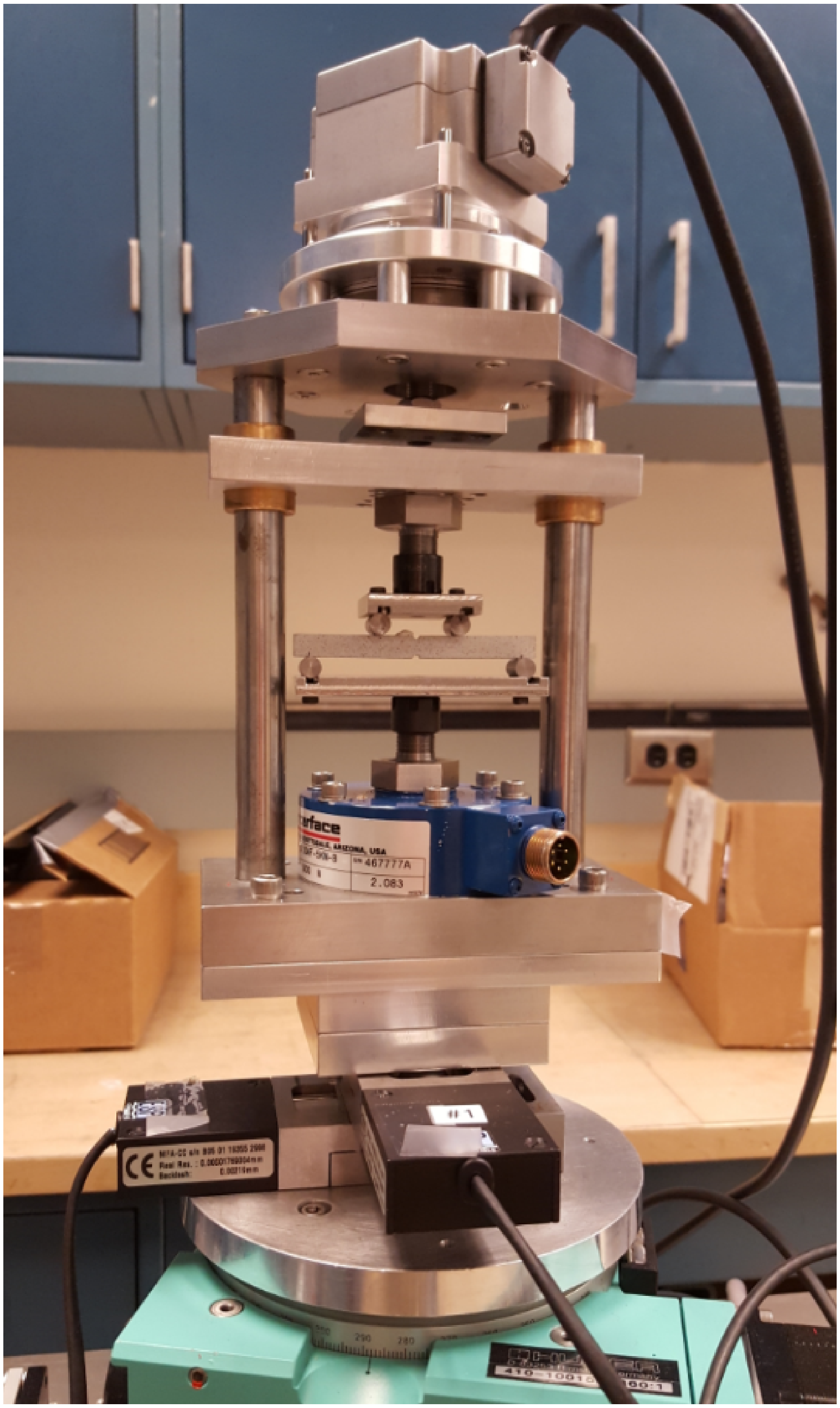

Figure 2.7 Load Frame Used With Ti-64 Samples

CHAPTER 3: EXPERIMENTAL RESULTS AND DISCUSSION

3.1 Aluminum Alloy 7075 Experiment

The diffraction ring corresponding to the (311) planar family was used to gauge all elastic strains from the 4-point bending experiment detailed in Section 2.4.1. An example diffraction image from AA7075 is displayed in Figure 3.1, and a plot of pixel intensity vs. 2θ is presented in Figure 3.2 with the (311) peak specified. The grid of measurement points on the AA7075 sample was contained in the region of constant moment between the two load pins. This region is illustrated schematically in Figure 1.2a. Due to the constant moment, strain values showed little variation with respect to x-coordinate. Stress and strain data from this experiment will therefore be presented as line plots with each data point at a particular y-coordinate representing an average value across all five x-positions. Elastic strains from each load step are presented in Figure 3.3. Stresses calculated from these elastic strains via Equation 2.19 are presented in Figure 3.4. A uniaxial (xx) stress state for each load step is observed, which is associated with pure bending.

XRD measurements revealed there was very little residual stress present before the experiment. After 1 turn of the screw there is a linear σ_{xx} profile, which is indicative of elastic behavior. However, after 2 turns of the screw, the σ_{xx} profile is no longer linear, but reaches a maximum absolute value around 500 MPa. This maximum value corresponds to the yield strength of the material, above which plastic flow begins. The observed yield stress agrees with the reported yield stress of AA7075 [5]. After 3 turns of the screw the yield surface moves toward the neutral axis, while the maximum stress remains very close to the reported yield stress. Only the linear region between $y = -1$ mm and $y = 1$ mm remains free of plasticity. After the load is removed there is both compressive and tensile residual stress. Figure 3.7 serves as a validation of the experimental measurements. The experimental bending stress $\sigma_\mathrm{b} = \sigma_{xx}$ is plotted first. The predicted elastic stress change upon unloading $\Delta\sigma$ can be calculated from the internal moment in the sample as discussed in Section 1.3. The predicted residual stress σ_{pred} is then given by $\sigma_{\text{pred}} = \sigma_{\text{b}} + \Delta\sigma$. The predicted residual stress is then compared with the measured residual stress σ_{r}. The close agreement between predicted and measured residual stresses serves as further proof of a pure bending state and further confidence in the measurement techniques.

The behavior of the residual stress can be explained by the dislocation movement underlying the plastic flow. The top of the sample (positive y-coordinate) yielded in compression and the bottom of the sample (negative y-coordinate) yielded in tension after 3 complete turns of the actuation screw. The sample was visibly bent such that the middle of the sample (x-coordinates close to 0) moved down while the edges of the sample (x-coordinates far from 0) moved up. Consequently, the bottom surface of the sample elongated while the top surface shortened. The deformation of the sample must have been due to dislocation movement rather than just atomic stretching, as evidenced by the permanent nature of the deformation. Material left the top region of the sample in order for it to permanently shorten, while material entered the bottom region of the sample in order for it to permanently elongate. Upon unloading the sample there was compressive residual stress at the bottom surface due to the addition of material into this region, while there was tensile residual stress at the top surface due to removal of material from this region. In the unloaded state internal stresses must arise in order for the sample to be in equilibrium, i.e. below the neutral axis a tensile stress counteracts the compressive residual stress along the bottom surface of the sample, and above the neutral axis a compressive stress counteracts the tensile residual stress along the top surface of the sample.

All strains measured from XRD are elastic, as discussed in Section 2.1. DIC was used to measure the total strains, since the deformations in the experiment were small. Knowledge of the elastic and total strains allowed the plastic strains to be computed via $\varepsilon^{\text{p}} = \varepsilon^{\text{t}} - \varepsilon^{\text{e}}$. For the AA7075 results the DIC measurements were averaged in the x-direction to produce a one-dimensional strain vs. y-coordinate profile. These averaged results were used in the calculation of plastic strain. For the case of pure bending the total strain is equal to the elastic strain in the linear region of the curve near the neutral axis where yielding has not taken place, and it can be determined outside of this region using a linear extrapolation. The elastic, plastic, and total strain components of ε_{xx} are plotted in Figure 3.5. The total strain measurements in this figure agree with the bending theory in that they match the elastic strain measurements where yielding had not taken place and they follow an extrapolated linear fit in the regions where yielding had taken place.

Figure 3.6 compares each load step for the elastic, plastic, and total components of ε_{xx}. The regions that contain plastic strain correspond with the regions where elastic strain reached a maximum absolute value, or where yielding occurred. The regions that contain no plastic strain correspond to linear elastic strain regions, or where yielding did not occur. There was no measurable change in plastic strain upon unloading due to the permanent nature of plastic deformation.

3.2 Titanium-6Al-4V Experiment

Elastic strains were also measured from the 4-point bending experiment detailed in Section 2.4.2. The diffraction rings corresponding to the (100) and (200) planar families were used to measure the strains in the α- and β-phases, respectively. An example diffraction image from Ti-64 is displayed in Figure 3.8, and a plot of pixel intensity vs. 2θ is presented in Figure 3.9 with the (100) and (200) peaks specified. As in the AA7075 experiment, the grid of measurement points was contained in the region of constant moment between the two load pins. This experiment contrasted with the AA7075 experiment in that notches cut out of the sample created regions of stress concentration leading to non-uniform strain profiles in both the x- and y-directions. Consequently, strain measurements from this experiment will be presented as scatter plots. Bending strain ($\varepsilon^{\mathrm{e}}_{xx}$) measurements from the α-phase are plotted in Figure 3.10 and compared with β-phase strains plotted in Figure 3.11. The highest strains were seen directly adjacent to the notches, which is also where the largest residual strains were measured. The transverse strains ($\varepsilon^{\mathrm{e}}_{yy}$) are plotted in Figures 3.12 and 3.13, while the shear strains ($\varepsilon^{\mathrm{e}}_{xy}$) are plotted in Figures 3.14 and 3.15. For all strain components the β-phase exhibited strains with larger magnitude than the α-phase.

3.3 Figures

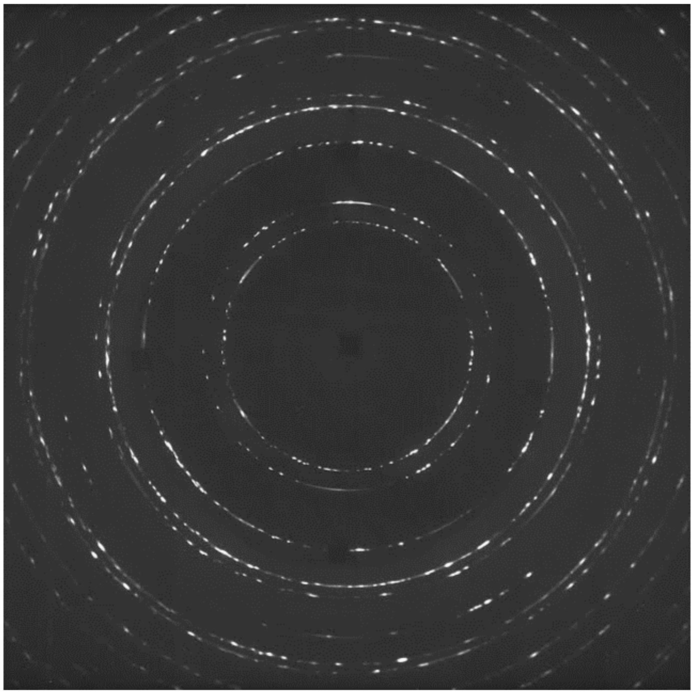

Figure 3.1 Diffraction Image from AA7075

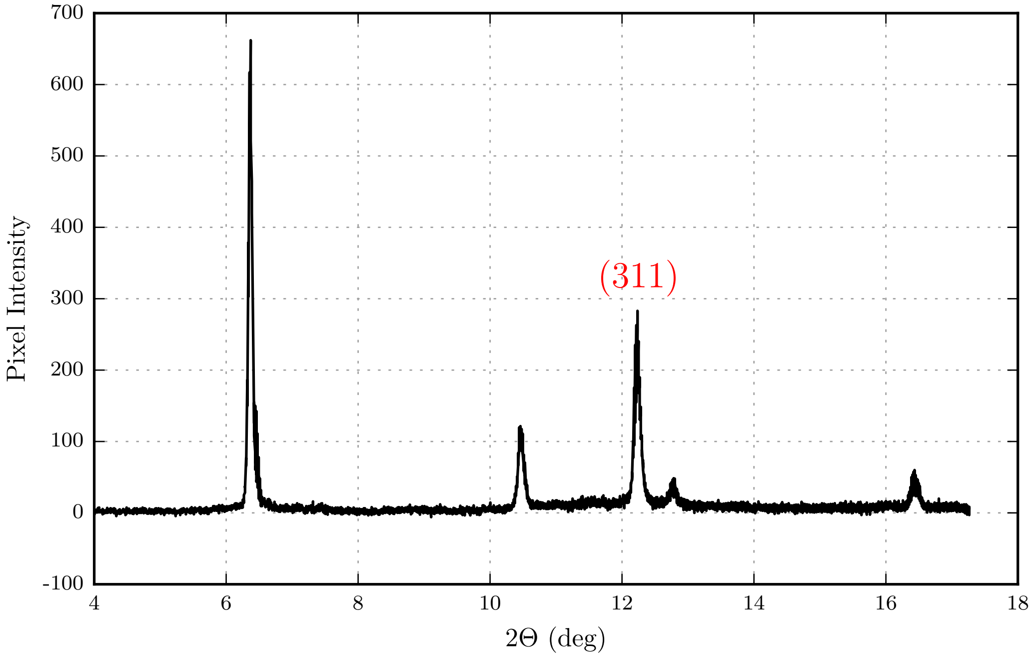

Figure 3.2 AA7075 Planar Family Spectrum

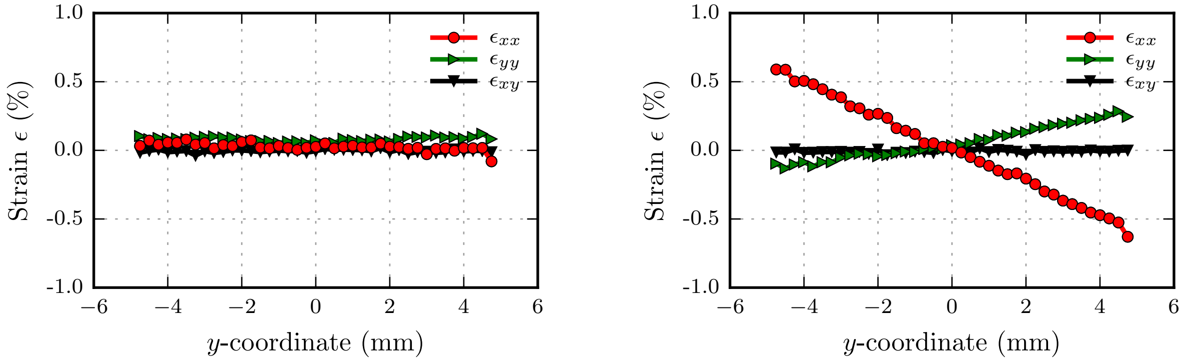

(a) Before loading

(b) 1 turn of screw

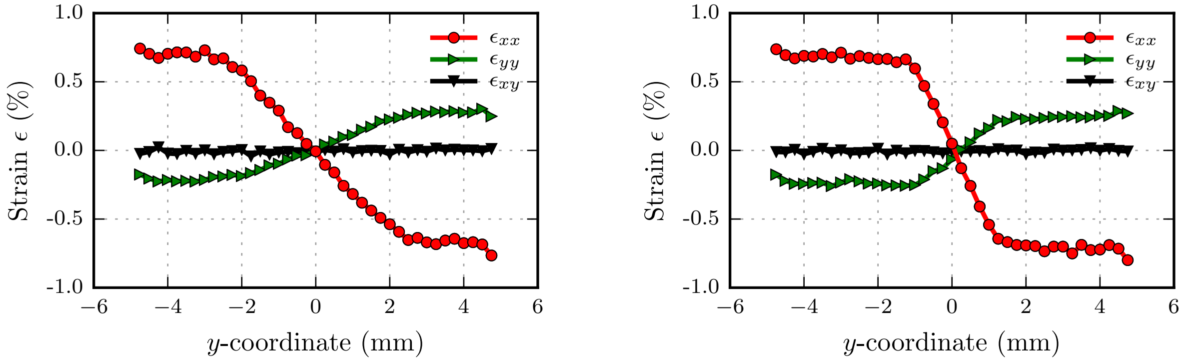

(c) 2 turns of screw

(d) 3 turns of screw

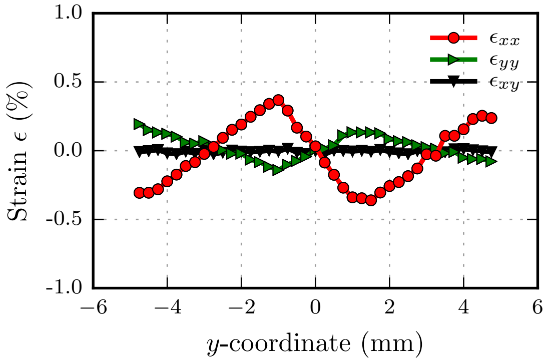

(e) After unloading

Figure 3.3 AA7075 ε^{e} Averaged in x vs. y-position

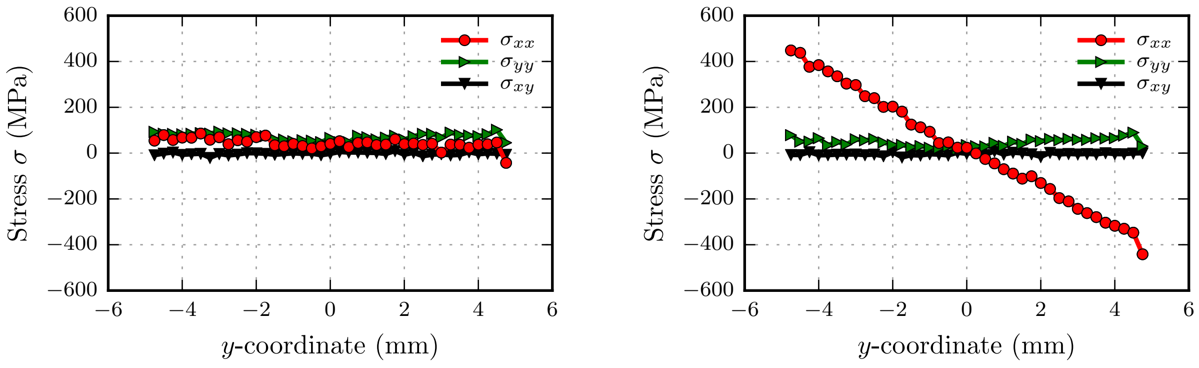

(a) Before loading (b) 1 turn of screw

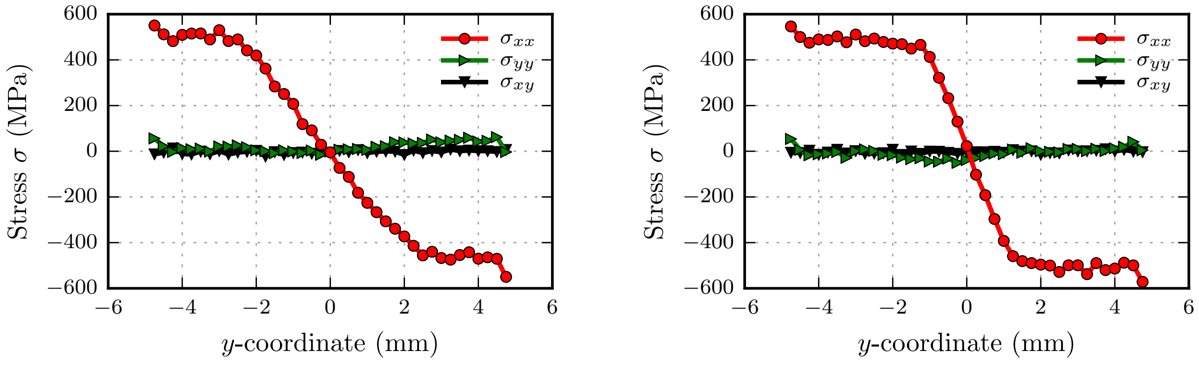

(c) 2 turns of screw (d) 3 turns of screw

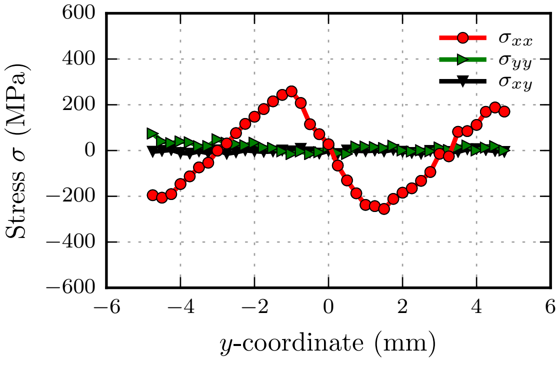

(e) After unloading

Figure 3.4 AA7075 σ Averaged in x vs. y-position

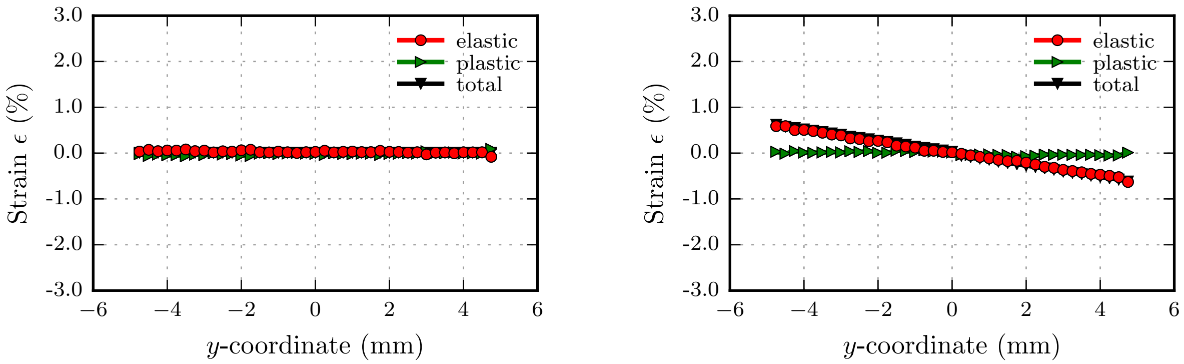

(a) Before loading

(b) 1 turn of screw

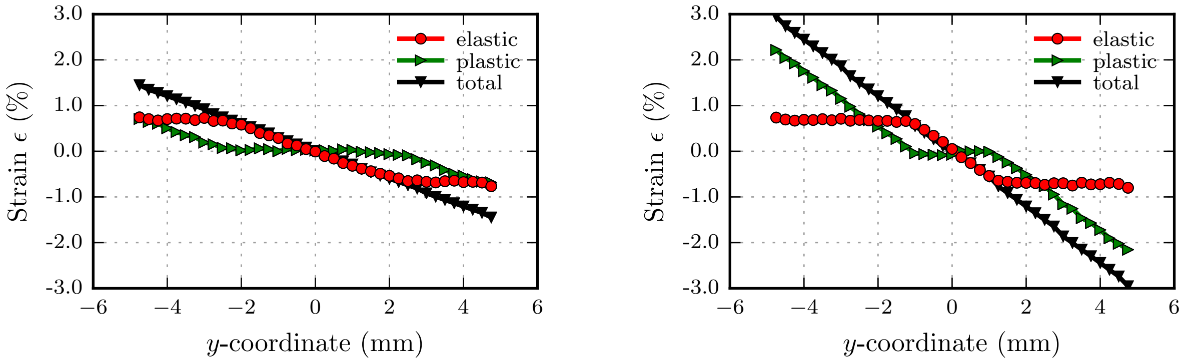

(c) 2 turns of screw

(d) 3 turns of screw

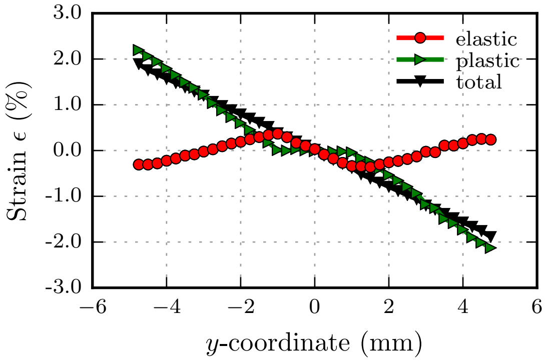

(e) After unloading

Figure 3.5 AA7075 ε_{xx} Averaged in x vs. y-position

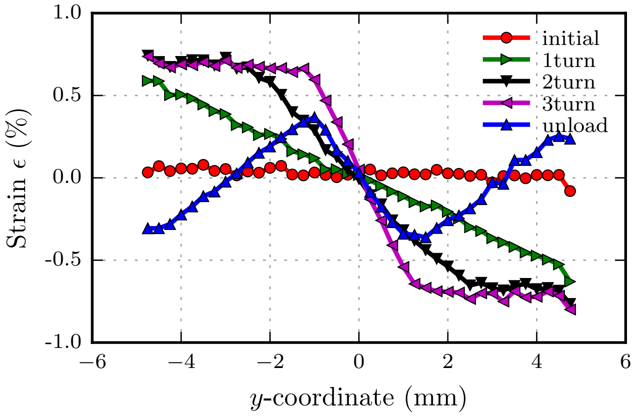

(a) Averaged $\varepsilon^{\mathrm{e}}_{xx}$ vs. y-position

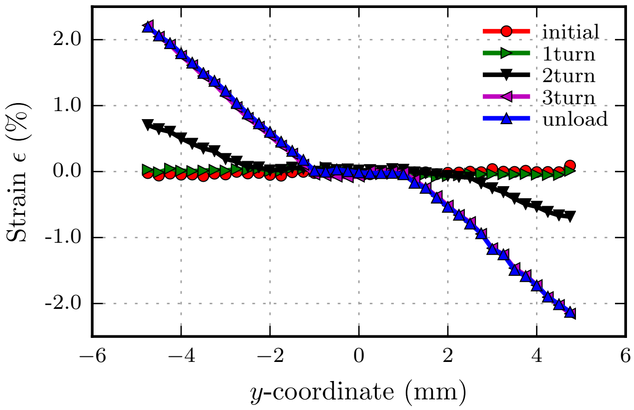

(b) Averaged $\varepsilon^{\mathrm{p}}_{xx}$ vs y-position

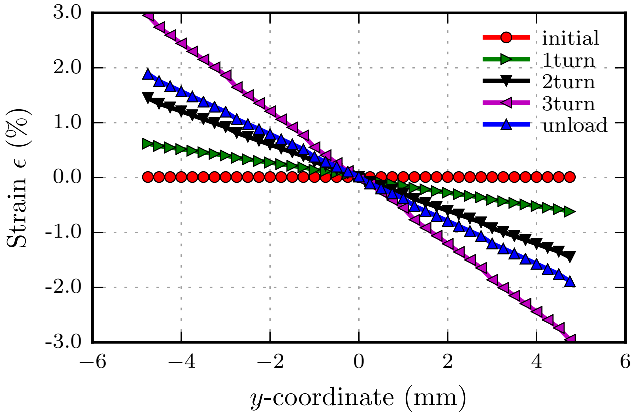

(c) Averaged $\varepsilon^{\mathrm{t}}_{xx}$ vs. y-position

Figure 3.6 AA7075 ε_{xx} Averaged in x vs. y-position

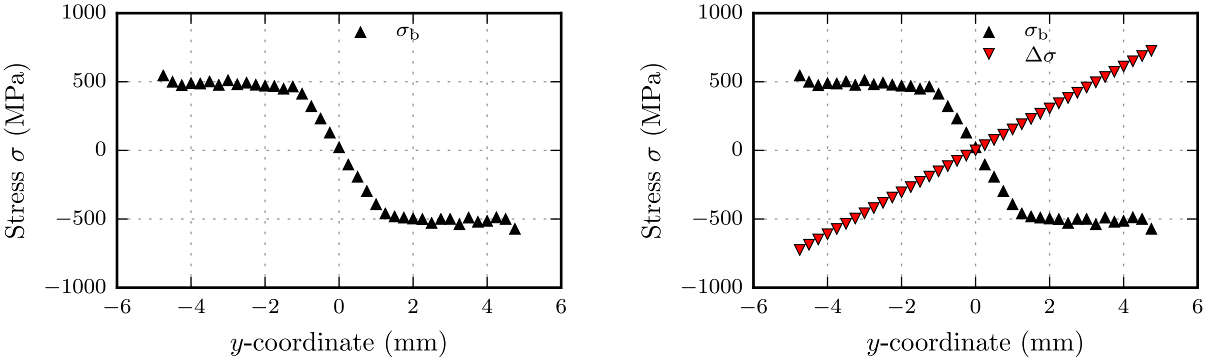

(a) Measured Bending Stress (b) Predicted Stress Relaxation

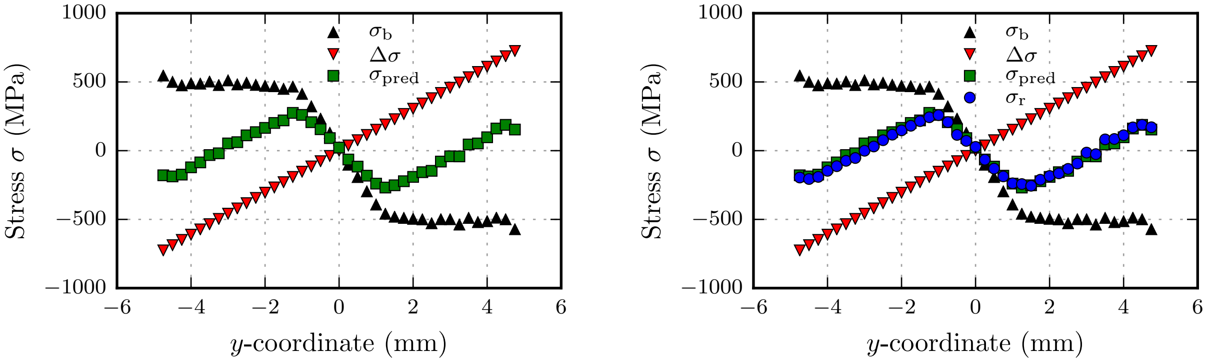

(c) Predicted Residual Stress (d) Comparison With Measured Residual Stress

Figure 3.7 AA7075 Residual Stress Validation

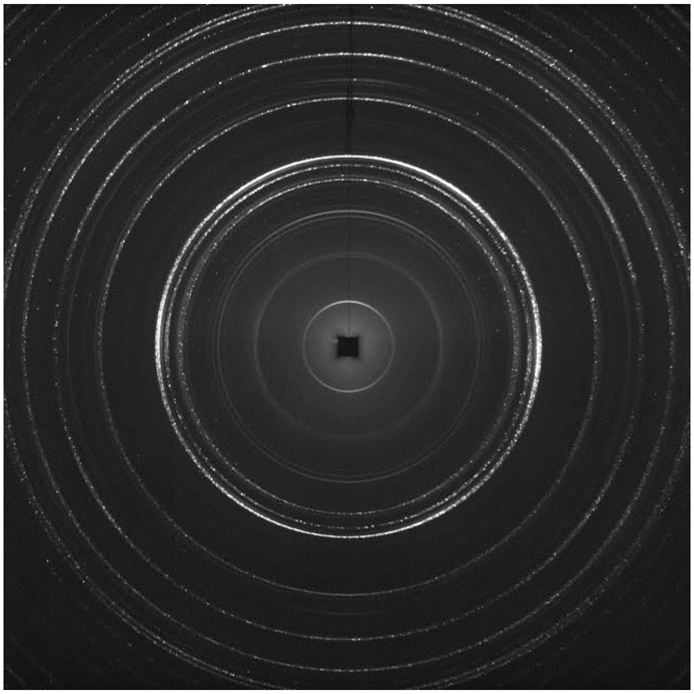

Figure 3.8 Diffraction Image from Ti-64

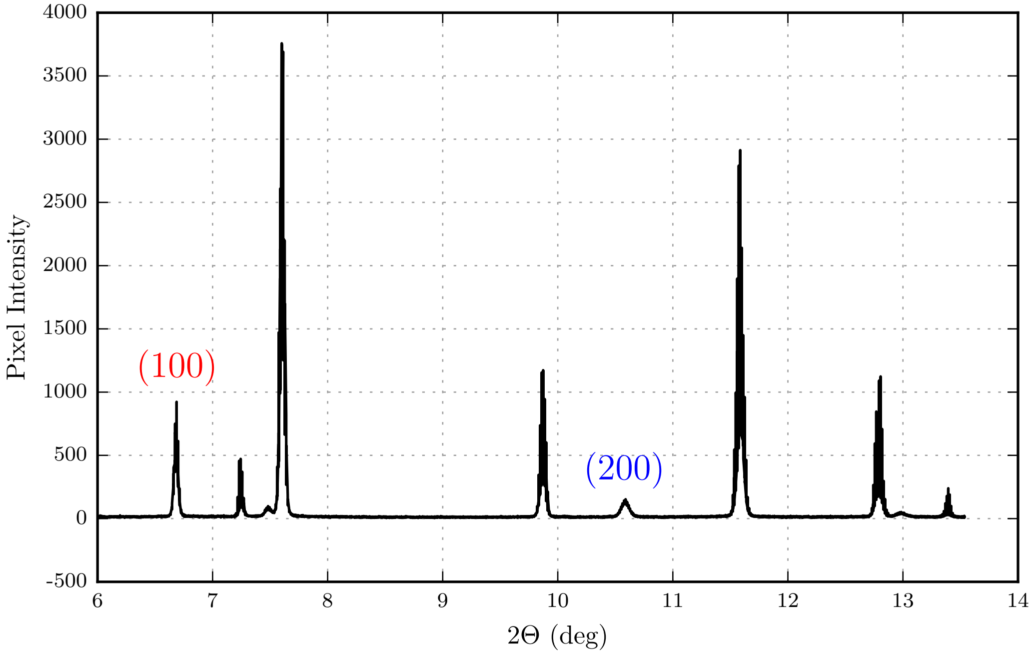

Figure 3.9 Ti-64 Planar Family Spectrum

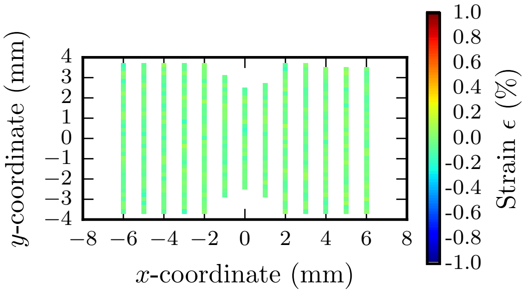

(a) Before loading

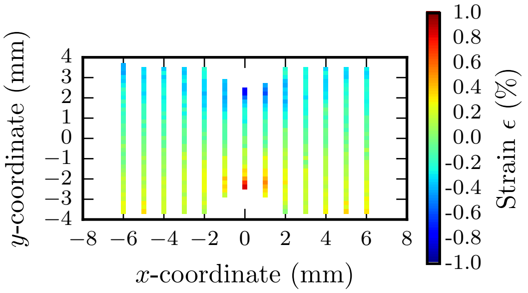

(b) 1000 N Applied Load

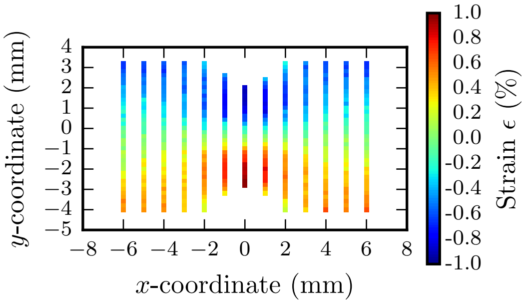

(c) 2000 N Applied Load

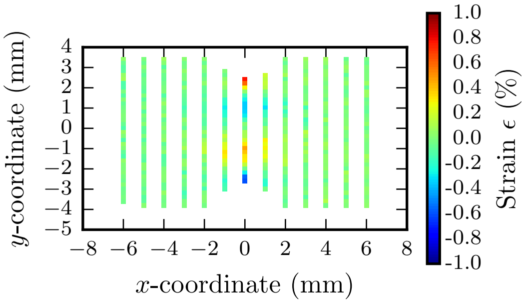

(d) After unloading

Figure 3.10 Ti-64 α-phase $\varepsilon^{\mathrm{e}}_{xx}$

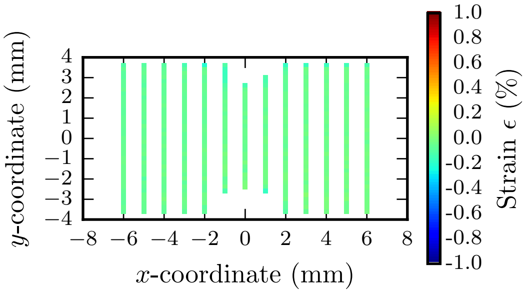

(a) Before loading

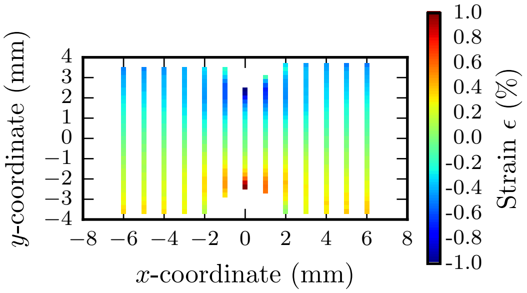

(b) 1000 N Applied Load

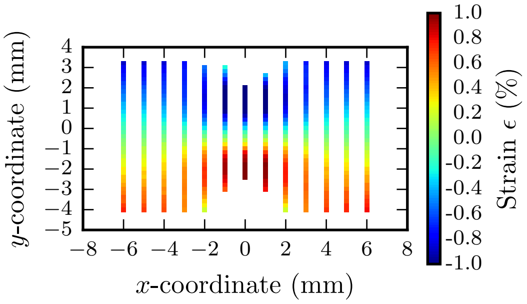

(c) 2000 N Applied Load

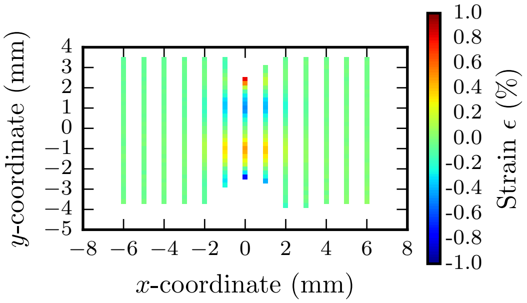

(d) After unloading

Figure 3.11 Ti-64 β-phase $\varepsilon^{\mathrm{e}}_{xx}$

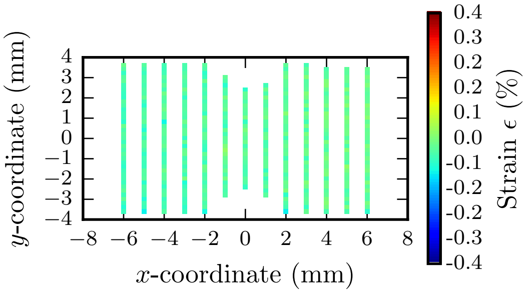

(a) Before loading

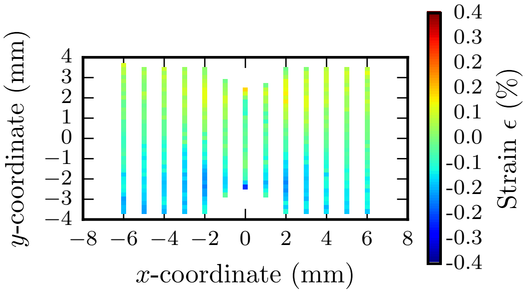

(b) 1000 N Applied Load

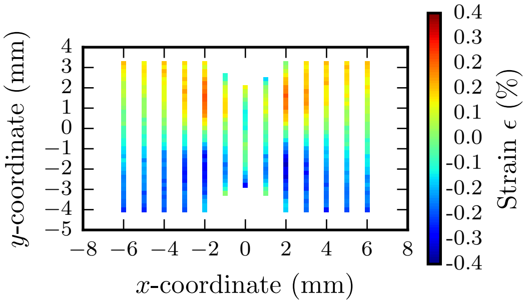

(c) 2000 N Applied Load

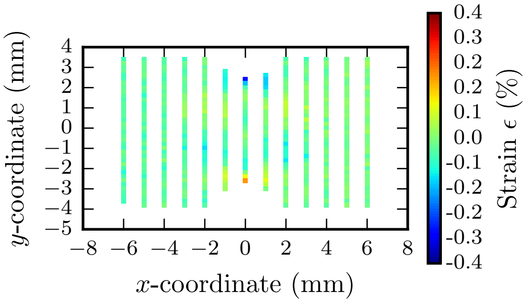

(d) After unloading

Figure 3.12 Ti-64 α-phase $\varepsilon^{\mathrm{e}}_{yy}$

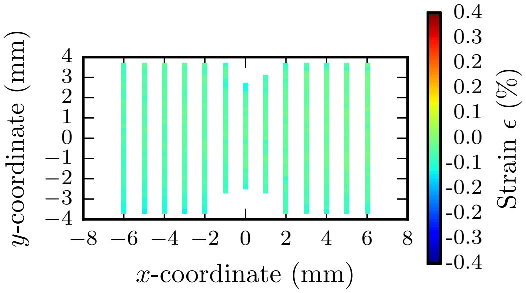

(a) Before loading

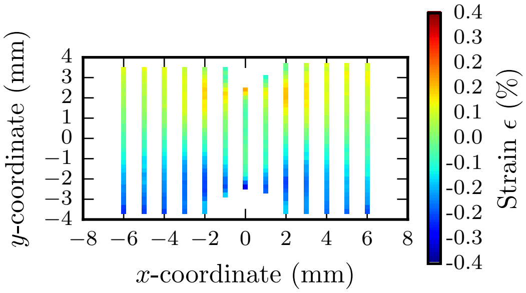

(b) 1000 N Applied Load

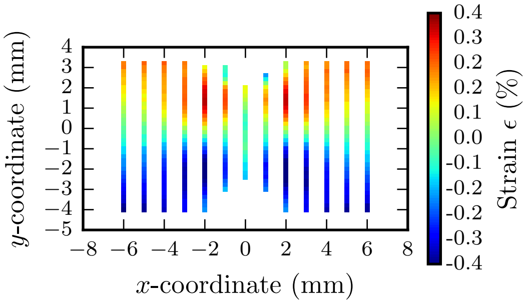

(c) 2000 N Applied Load

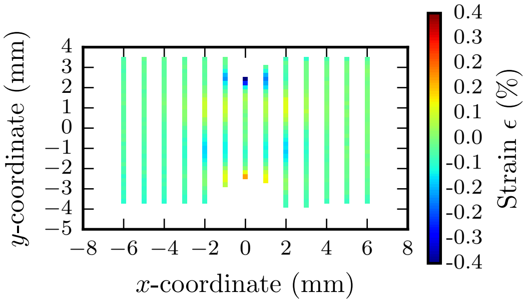

(d) After unloading

Figure 3.13 Ti-64 β-phase $\varepsilon^{\mathrm{e}}_{yy}$

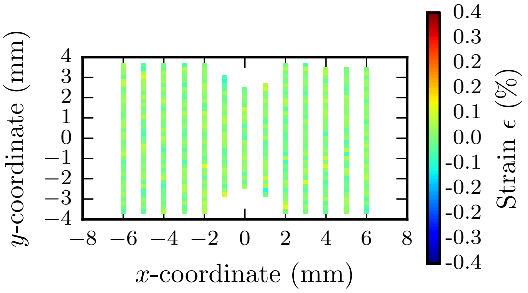

(a) Before loading

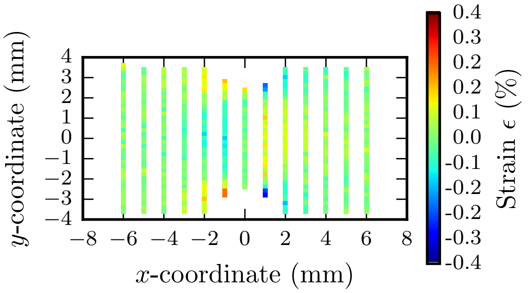

(b) 1000 N Applied Load

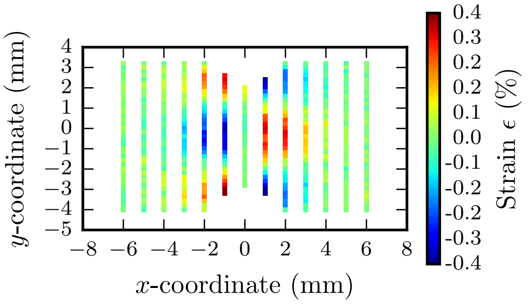

(c) 2000 N Applied Load

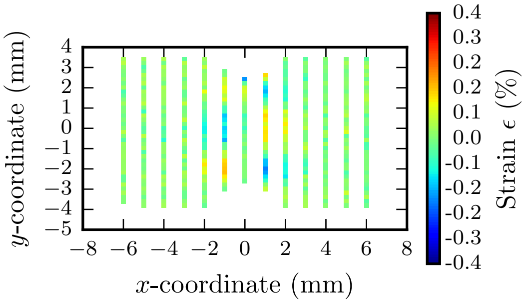

(d) After unloading

Figure 3.14 Ti-64 α-phase $\varepsilon^{\mathrm{e}}_{xy}$

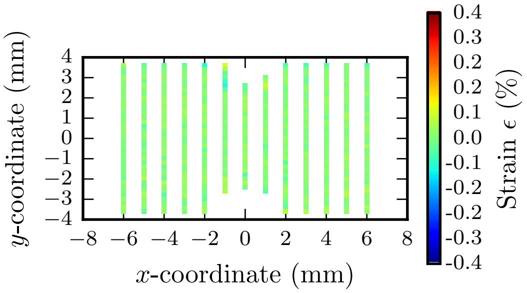

(a) Before loading

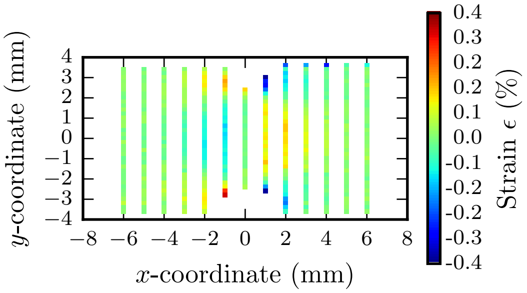

(b) 1000 N Applied Load

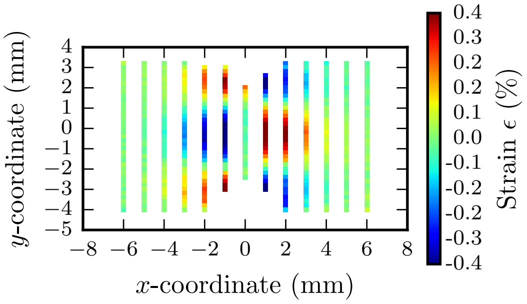

(c) 2000 N Applied Load

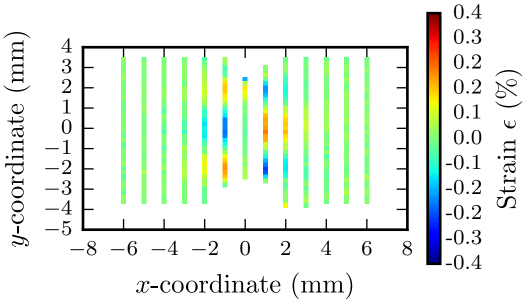

(d) After unloading

Figure 3.15 Ti-64 β-phase $\varepsilon^{\mathrm{e}}_{xy}$

CHAPTER 4: DISLOCATION DENSITY DISTRIBUTION INVERSE PROBLEM

4.1 Theory

Dislocations are so prevalent in a real material that it would be impossible to model all of them for the samples studied in this work. There are two approaches to modeling dislocations, namely discrete and continuum. As its name suggests, a discrete dislocation formulation treats dislocations as discrete objects with associated stress fields. Dislocation dynamics during plastic flow are often modeled in this way. The discrete dislocations in the model can represent single atomic dislocations in a simulation of one or a few grains, or they may represent a group of dislocations in a simulation of a polycrystalline material. The stress field from a dislocation is linear with respect to Burgers vector, as mentioned in Section 1.2, which allows for many atomic dislocations to be represented by a smaller number of model dislocations with larger Burgers vectors. The alternative to treating dislocations as discrete objects is to view their distribution as a continuum with a spatially varying density. Plasticity models based on continuously distributed dislocations have been developed [2, 11] that provide a means for calculating strain fields from dislocation density distributions by solving two boundary value problems (BVP).

A body that is in equilibrium in the absence of body loads will satisfy

$$\operatorname{div} \boldsymbol{\sigma} = 0, \tag{4.20}$$

where $\boldsymbol{\sigma}$ is the second-order Cauchy stress tensor, at every point in the body. The stress tensor is related to the strain tensor through a constitutive relation, which for small deformations is given by

$$\boldsymbol{\sigma} = \mathbb{C}\left[\boldsymbol{E}^{\epsilon}\right], \tag{4.21}$$

where $\mathbb{C}$ is the fourth-order constitutive tensor and $\boldsymbol{E}^{\epsilon}$ is the second-order small strain tensor. A distortion tensor $\boldsymbol{U}$ can be defined such that

$$\boldsymbol{U} \equiv \nabla \boldsymbol{u}. \tag{4.22}$$

where $\boldsymbol{u}$ is the displacement field. The distortion, analogously to strain, may be broken into elastic and plastic parts by

$$\boldsymbol{U} = \boldsymbol{U}^{\mathrm{e}} + \boldsymbol{U}^{\mathrm{p}}, \tag{4.23}$$

The small strain tensor is related to the elastic distortion by

$$E^{\epsilon} = \mathrm{sym}\left(\boldsymbol{U}^{\mathrm{e}}\right), \tag{4.24}$$

so it follows that

$$\boldsymbol{\sigma} = \mathbb{C}\left[\mathrm{sym}\left(\boldsymbol{U}^{\mathrm{e}}\right)\right]. \tag{4.25}$$

The constitutive tensor has inherent symmetries that will only allow it to see the symmetric part of the second-order tensor it operates on, deeming the symmetric operator in Equation (4.25) unnecessary. Consequently, under the small strain assumption the constitutive relation is

$$\boldsymbol{\sigma} = \mathbb{C}\left[\boldsymbol{U}^{\mathrm{e}}\right]. \tag{4.26}$$

The distortion tensor can be expressed as sum of a compatible projection and an incompatible projection, which will be noted by $\boldsymbol{U}_{\mathrm{c}}$ and $\boldsymbol{U}_{\mathrm{i}}$ respectively. The compatible projection lies in a gradient, while the incompatible projection lies in a curl. These projections are orthogonal, as displayed by the fact that $\mathrm{curl}\left(\nabla \boldsymbol{a}\right) = 0$ for any vector field $\boldsymbol{a}$. A compatible elastic distortion is given by

$$\boldsymbol{U}_{\mathrm{c}}^{\mathrm{e}} = \nabla \boldsymbol{u}, \tag{4.27}$$

and it follows that $\mathrm{curl}\, \boldsymbol{U}_{\mathrm{c}}^{\mathrm{e}} = 0$. If the elastic distortion is fully compatible, *i.e.* $\boldsymbol{U}^{\mathrm{e}} = \boldsymbol{U}_{\mathrm{c}}^{\mathrm{e}}$, the definition of the small strain tensor given in Equation (4.24) becomes

$$E^{\epsilon} = \frac{1}{2}\left(\nabla \boldsymbol{u} + (\nabla \boldsymbol{u})^{\mathrm{T}}\right), \tag{4.28}$$

and the constitutive relation becomes

$$\boldsymbol{\sigma} = \mathbb{C}\left[\nabla \boldsymbol{u}\right]. \tag{4.29}$$

The important underlying assumption leading to these relations is that of a fully compatible $\boldsymbol{U}^{\mathrm{e}}$. While this assumption is widely used in solid mechanics to determine displacements, it cannot be used if the effect of dislocations is considered. Dislocations introduce incompatibilities into $\boldsymbol{U}^{\mathrm{e}}$, which is exemplified by observing the lack of closure of the Burgers circuit that is created upon introducing a dislocation into a crystal lattice. As such the curl of the elastic distortion is no longer zero, and will be described by [11][2]

$$\operatorname{curl} \boldsymbol{U}^{\mathrm{e}} = \tilde{\boldsymbol{\alpha}} \tag{4.30}$$

where $\tilde{\boldsymbol{\alpha}}$ is the second-order dislocation density tensor. The components of the $\tilde{\boldsymbol{\alpha}}$ tensor have idealized physical representations [2]. The first index represents the Burgers vector direction, and the second index represents the dislocation line direction. The diagonal components (11, 22, 33) can therefore be thought of as idealized screw dislocations, while the off-diagonal components (12, 13, 21, 23, 31, 32) can be thought of as idealized edge dislocations. As mentioned above, $\boldsymbol{U}^{\mathrm{e}}$ may be expressed as a sum of its compatible and incompatible projections, or

$$\boldsymbol{U}^{\mathrm{e}} = \boldsymbol{U}^{\mathrm{e}}_{\mathrm{c}} + \boldsymbol{U}^{\mathrm{e}}_{\mathrm{i}}. \tag{4.31}$$

Substituting Equation (4.31) into Equation (4.30) gives

$$\operatorname{curl}\left(\boldsymbol{U}^{\mathrm{e}}_{\mathrm{c}} + \boldsymbol{U}^{\mathrm{e}}_{\mathrm{i}}\right) = \tilde{\boldsymbol{\alpha}}. \tag{4.32}$$

Since $\boldsymbol{U}_\mathrm{c}^\mathrm{e}$ lies in a gradient, its curl will always be zero reducing Equation (4.32) to

$$\operatorname{curl} \boldsymbol{U}_\mathrm{i}^\mathrm{e} = \tilde{\boldsymbol{\alpha}}. \tag{4.33}$$

To ease notation $\boldsymbol{U}_\mathrm{i}^\mathrm{e}$ will be referred to as $\boldsymbol{\chi}$ hereafter and thus

$$\operatorname{curl} \boldsymbol{\chi} = \tilde{\boldsymbol{\alpha}}. \tag{4.34}$$

4.1.1 Incompatible Elastic Distortion Boundary Value Problem

A BVP may be solved to determine $\boldsymbol{\chi}$ if $\tilde{\boldsymbol{\alpha}}$ is known throughout the body [20]. Physical observation leads to a constraint of

$$\operatorname{div} \boldsymbol{\chi} = 0, \tag{4.35}$$

which requires that dislocations do not end in the body. A boundary condition of

$$\boldsymbol{\chi}\boldsymbol{n} = 0, \tag{4.36}$$

where $\boldsymbol{n}$ is the unit normal vector, is placed on all boundaries to complete the BVP. A least squares finite element formulation is used to solve for $\boldsymbol{\chi}$. A residual is stated such that Equations (4.34) and (4.35) are enforced throughout the interior of the body [1], given by

$$\mathrm{R} = \frac{1}{2}\int_{\Omega} (\operatorname{curl}\boldsymbol{\chi} - \tilde{\boldsymbol{\alpha}}) \cdot (\operatorname{curl}\boldsymbol{\chi} - \tilde{\boldsymbol{\alpha}})\ \mathrm{dV} + \frac{1}{2}\int_{\Omega} (\operatorname{div}\boldsymbol{\chi} \cdot \operatorname{div}\boldsymbol{\chi})\ \boldsymbol{dV} \tag{4.37}$$

Equation (4.36) is strictly enforced on the boundary elements and will not be discussed further in this derivation. Equation (4.37) can be expanded into

$$\mathrm{R} = \frac{1}{2}\int_{\Omega} (\operatorname{curl}\boldsymbol{\chi} \cdot \operatorname{curl}\boldsymbol{\chi} - 2\operatorname{curl}\boldsymbol{\chi} \cdot \tilde{\boldsymbol{\alpha}} + \tilde{\boldsymbol{\alpha}} \cdot \tilde{\boldsymbol{\alpha}})\ \mathrm{dV} + \frac{1}{2}\int_{\Omega} (\operatorname{div}\boldsymbol{\chi} \cdot \operatorname{div}\boldsymbol{\chi})\ \mathrm{dV} \tag{4.38}$$

Minimization of this residual can be achieved by equating its variation to zero. Taking the variation of Equation (4.38) with respect to $\boldsymbol{\chi}$ yields

$$\delta\mathrm{R} = \int_{\Omega} \left(\frac{1}{2} (\delta \operatorname{curl}\boldsymbol{\chi} \cdot \operatorname{curl}\boldsymbol{\chi} + \operatorname{curl}\boldsymbol{\chi} \cdot \delta\operatorname{curl}\boldsymbol{\chi}) - \tilde{\boldsymbol{\alpha}} \cdot \delta\operatorname{curl}\boldsymbol{\chi} + \frac{1}{2} (\delta\operatorname{div}\boldsymbol{\chi} \cdot \operatorname{div}\boldsymbol{\chi} + \operatorname{div}\boldsymbol{\chi} \cdot \delta\operatorname{div}\boldsymbol{\chi}) \right) \mathrm{dV} \tag{4.39}$$

which can be reduced to

$$\delta \mathrm{R} = \int_{\Omega} (\delta \,\mathrm{curl}\, \boldsymbol{\chi} \cdot \mathrm{curl}\, \boldsymbol{\chi} - \tilde{\boldsymbol{\alpha}} \cdot \delta \,\mathrm{curl}\, \boldsymbol{\chi} + \delta \,\mathrm{div}\, \boldsymbol{\chi} \cdot \mathrm{div}\, \boldsymbol{\chi})\, \mathrm{dV} \tag{4.40}$$

and equivalently expressed as

$$\delta \mathrm{R} = \int_{\Omega} (\delta \,\mathrm{curl}\, \boldsymbol{\chi} \cdot (\mathrm{curl}\, \boldsymbol{\chi} - \tilde{\boldsymbol{\alpha}}) + \delta \,\mathrm{div}\, \boldsymbol{\chi} \cdot \mathrm{div}\, \boldsymbol{\chi}) \;\, \mathrm{dV} \tag{4.41}$$

Equation (4.41) can be expressed in indicial notation as

$$\delta \mathrm{R} = \int_{\Omega} \Big(e_{ijk} \; \delta \chi_{rk,j} \, (e_{imn} \, \chi_{rn,m} - \tilde{\alpha}_{ri}) + \delta \chi_{ij,j} \, \chi_{im,m} \Big) \;\, \mathrm{dV} \tag{4.42}$$

where e_{ijk} is the permutation operator. Since Equation (4.42) must hold over the whole domain, it may be enforced over each element of a finite element formulation. At this point weight and shape functions may be introduced [1] in indicial notation respectively as

$$\delta \chi_{rk} = \mathrm{N}^{\mathrm{A}} \delta \chi_{rk}^{\mathrm{A}}, \tag{4.43}$$

and

$$\chi_{rn} = \mathrm{N}^{\mathrm{B}} \chi_{rn}^{\mathrm{B}} \tag{4.44}$$

where A and B are the indices of the finite element nodes. The usual convention of summing over repeated indices holds here and as such there will be as many terms as there are nodes in each element. The weight and shape functions can be differentiated as necessary to be used with the curl and div operators, which gives

$$\delta \chi_{rk,j} = \frac{\partial \mathrm{N}^{\mathrm{A}}}{\partial x_j} \delta \chi_{rk}^{\mathrm{A}}, \tag{4.45}$$

$$\delta\chi_{ij,j} = \frac{\partial \mathrm{N}^{\mathrm{A}}}{\partial x_j}\delta\chi^{\mathrm{A}}_{ij}, \tag{4.46}$$

$$\chi_{rn,m} = \frac{\partial \mathrm{N}^{\mathrm{B}}}{\partial x_m}\chi^{\mathrm{B}}_{rn}, \tag{4.47}$$

and

$$\chi_{im,m} = \frac{\partial \mathrm{N}^{\mathrm{B}}}{\partial x_m}\chi^{\mathrm{B}}_{im} \tag{4.48}$$

since the nodal values of $\boldsymbol{\chi}$ and $\delta\boldsymbol{\chi}$ are constants with respect to position. Substituting Equations (4.45) - (4.48) into Equation (4.42), produces

$$\delta\mathrm{R} = \int_{\Omega}\left(e_{ijk}\,\frac{\partial \mathrm{N}^{\mathrm{A}}}{\partial x_j}\delta\chi^{\mathrm{A}}_{rk}\left(e_{imn}\,\frac{\partial \mathrm{N}^{\mathrm{B}}}{\partial x_m}\chi^{\mathrm{B}}_{rn} - \tilde{\alpha}_{ri}\right) + \frac{\partial \mathrm{N}^{\mathrm{A}}}{\partial x_j}\delta\chi^{\mathrm{A}}_{ij}\,\frac{\partial \mathrm{N}^{\mathrm{B}}}{\partial x_m}\chi^{\mathrm{B}}_{im}\right)\,\mathrm{dV} \tag{4.49}$$

Setting the resulting expression for $\delta\mathrm{R}$ equal to zero in order to minimize R and factoring the weighting function nodal values out of the integral yields

$$\delta\mathrm{R} = \delta\chi^{\mathrm{A}}_{rk}\left[\int_{\Omega}\left(e_{ijk}\,\frac{\partial \mathrm{N}^{\mathrm{A}}}{\partial x_j}\left(e_{imn}\,\frac{\partial \mathrm{N}^{\mathrm{B}}}{\partial x_m}\chi^{\mathrm{B}}_{rn} - \tilde{\alpha}_{ri}\right) + \delta_{ri}\delta_{kj}\frac{\partial \mathrm{N}^{\mathrm{A}}}{\partial x_j}\frac{\partial \mathrm{N}^{\mathrm{B}}}{\partial x_m}\chi^{\mathrm{B}}_{im}\right)\,\mathrm{dV}\right] = 0 \tag{4.50}$$

The arbitrariness of the weighting functions allows $\delta\chi^{\mathrm{A}}_{rk} \neq 0$ and so Equation (4.39) is equivalently expressed as

$$\int_{\Omega}\left(e_{ijk}\,\frac{\partial \mathrm{N}^{\mathrm{A}}}{\partial x_j}\left(e_{imn}\,\frac{\partial \mathrm{N}^{\mathrm{B}}}{\partial x_m}\chi^{\mathrm{B}}_{rn} - \tilde{\alpha}_{ri}\right) + \frac{\partial \mathrm{N}^{\mathrm{A}}}{\partial x_k}\delta_{mn}\frac{\partial \mathrm{N}^{\mathrm{B}}}{\partial x_m}\chi^{\mathrm{B}}_{rn}\right)\,\mathrm{dV} = 0. \tag{4.51}$$

The nodal values of $\boldsymbol{\chi}$ can be factored out of the integral resulting in

$$\left[\int_{\Omega}\left(e_{ijk}\,\frac{\partial \mathrm{N}^{\mathrm{A}}}{\partial x_j}e_{imn}\,\frac{\partial \mathrm{N}^{\mathrm{B}}}{\partial x_m} + \frac{\partial \mathrm{N}^{\mathrm{A}}}{\partial x_k}\,\frac{\partial \mathrm{N}^{\mathrm{B}}}{\partial x_n}\right)\,\mathrm{dV}\right]\chi^{\mathrm{B}}_{rn} = \int_{\Omega} e_{ijk}\,\frac{\partial \mathrm{N}^{\mathrm{A}}}{\partial x_j}\tilde{\alpha}_{ri}\,\mathrm{dV} \tag{4.52}$$

The expressions in brackets multiplied by χ^{B}_{rn} can be assembled and viewed as a global stiffness matrix, while the right hand side of the equation can be viewed as a global load vector. Solving this linear system will determine the nodal values of χ. The value of χ at any point in the domain can then be interpolated using the shape functions and these nodal values.

4.1.2 Equilibrium Boundary Value Problem

The displacement field can be determined by solving the equilibrium problem presented in Equation (4.20). The strong form of the BVP is presented as

$$\begin{aligned}
&\nabla \cdot \boldsymbol{\sigma} = 0 && \text{in } \mathit{\Omega} \\
&\boldsymbol{\sigma} = \mathbb{C}\left[\boldsymbol{U}^{\mathrm{e}}\right] && \\
&\boldsymbol{\sigma}\boldsymbol{n} = \boldsymbol{s}^{\mathrm{p}} && \text{on } \mathrm{A}^{\mathrm{t}} \\
&\boldsymbol{u} = \boldsymbol{u}^{\mathrm{p}} && \text{on } \mathrm{A}^{\mathrm{u}}
\end{aligned} \tag{4.53}$$

where $\boldsymbol{s}^{\mathrm{p}}$ is the prescribed traction over the surface A^{t} and $\boldsymbol{u}^{\mathrm{p}}$ is the prescribed displacement over the surface A^{u}. In the presence of dislocations the elastic distortion is no longer compatible, and so $\boldsymbol{U}^{\mathrm{e}} \neq \nabla\boldsymbol{u}$. In fact $\boldsymbol{U}^{\mathrm{e}}$ cannot be stated directly in terms of $\boldsymbol{u}$, so a substitution will be made after manipulating Equation (4.23) into $\boldsymbol{U}^{\mathrm{e}} = \boldsymbol{U} - \boldsymbol{U}^{\mathrm{p}}$. The constitutive relation therefore becomes

$$\boldsymbol{\sigma} = \mathbb{C}\left[\boldsymbol{U} - \boldsymbol{U}^{\mathrm{p}}\right]. \tag{4.54}$$

Substituting the definition of $\boldsymbol{U}$ from Equation (4.22) and expressing $\boldsymbol{U}^{\mathrm{p}}$ as the sum of its compatible and incompatible projections yields

$$\boldsymbol{\sigma} = \mathbb{C}\left[\nabla\boldsymbol{u} - \boldsymbol{U}_{\mathrm{c}}^{\mathrm{p}} - \boldsymbol{U}_{\mathrm{i}}^{\mathrm{p}}\right]. \tag{4.55}$$

It is obvious from the definition of $\boldsymbol{U}$ in Equation (4.22) that $\boldsymbol{U}_{\mathrm{i}} = 0$. That is to say that the curl of the distortion is zero, since it is defined by a gradient. This result does not mean, however, that the elastic and plastic distortions both have zero incompatible projections. Rather their sum is zero, which leads to

$$\boldsymbol{\chi} = \boldsymbol{U}_{\mathrm{i}}^{\mathrm{e}} = -\boldsymbol{U}_{\mathrm{i}}^{\mathrm{p}}. \tag{4.56}$$

$\boldsymbol{U}_{\mathrm{c}}^{\mathrm{p}}$ will be assumed to have no effect on the stress field and therefore will be neglected in the constitutive relation. The incompatible constitutive equation is finally given as

$$\boldsymbol{\sigma} = \mathbb{C}\left[\nabla \boldsymbol{u} + \boldsymbol{\chi}\right]. \tag{4.57}$$

After $\boldsymbol{\chi}$ is determined by solving the BVP formulated in Section 4.1.1, $\boldsymbol{u}$ is the only unknown and can therefore be determined. Equation 4.53 can alternatively be expressed in a weak form with use of Equation (4.57) as

$$\int_{\Omega} \boldsymbol{w} \cdot \left(\operatorname{div} \mathbb{C}\left[\nabla \boldsymbol{u} + \boldsymbol{\chi}\right]\right)\, \mathrm{dV} - \int_{\mathrm{A}^{\mathrm{t}}} \boldsymbol{w} \cdot \left(\mathbb{C}\left[\nabla \boldsymbol{u} + \boldsymbol{\chi}\right] \boldsymbol{n} - \boldsymbol{s}^{\mathrm{p}}\right)\, \mathrm{da} + \int_{\mathrm{A}^{\mathrm{u}}} \boldsymbol{w} \cdot \left(\boldsymbol{u} - \boldsymbol{u}^{\mathrm{p}}\right)\, \mathrm{da} = 0 \tag{4.58}$$

where $\boldsymbol{w}$ is an arbitrary weighting function. The displacement on A^{u} will be prescribed a priori so its corresponding term in the weak form may be ignored for now. A relation can be derived [8] such that

$$\operatorname{div}\left(\boldsymbol{A}^{\mathrm{T}} \boldsymbol{b}\right) = \nabla \boldsymbol{b} \cdot \boldsymbol{A} + \boldsymbol{b} \cdot \left(\operatorname{div} \boldsymbol{A}\right), \tag{4.59}$$

which can be rearranged into

$$\boldsymbol{b} \cdot \left(\operatorname{div} \boldsymbol{A}\right) = \operatorname{div}\left(\boldsymbol{A}^{\mathrm{T}} \boldsymbol{b}\right) - \nabla \boldsymbol{b} \cdot \boldsymbol{A}. \tag{4.60}$$

In this case let $\boldsymbol{b} = \boldsymbol{w}$ and $\boldsymbol{A} = \mathbb{C}\left[\nabla \boldsymbol{u} + \boldsymbol{\chi}\right]$, and Equation (4.61) can be written as

$$\int_{\Omega} \left(\operatorname{div}\left(\left(\mathbb{C}\left[\nabla \boldsymbol{u} + \boldsymbol{\chi}\right]\right)^{\mathrm{T}} \boldsymbol{w}\right) - \nabla \boldsymbol{w} \cdot \mathbb{C}\left[\nabla \boldsymbol{u} + \boldsymbol{\chi}\right]\right)\, \mathrm{dV} - \int_{\mathrm{A}^{\mathrm{t}}} \boldsymbol{w} \cdot \left(\mathbb{C}\left[\nabla \boldsymbol{u} + \boldsymbol{\chi}\right] \boldsymbol{n} - \boldsymbol{s}^{\mathrm{p}}\right)\, \mathrm{da} = 0 \tag{4.61}$$

The divergence theorem can be employed to move the first term in the body integral to a surface integral resulting in

$$\int_{\Omega} -\nabla \boldsymbol{w} \cdot \mathbb{C}\left[\nabla \boldsymbol{u} + \boldsymbol{\chi}\right]\, \mathrm{dV} + \int_{\partial\Omega} \left(\mathbb{C}\left[\nabla \boldsymbol{u} + \boldsymbol{\chi}\right]\right)^{\mathrm{T}} \boldsymbol{w} \cdot \boldsymbol{n}\, \mathrm{da} - \int_{\mathrm{A}^{\mathrm{t}}} \boldsymbol{w} \cdot \left(\mathbb{C}\left[\nabla \boldsymbol{u} + \boldsymbol{\chi}\right] \boldsymbol{n} - \boldsymbol{s}^{\mathrm{p}}\right)\, \mathrm{da} = 0 \tag{4.62}$$

Using the definition of the transpose of second-order tensor given by [8],

$$\boldsymbol{A}^{\mathrm{T}}\boldsymbol{b} \cdot \boldsymbol{c} = \boldsymbol{b} \cdot \boldsymbol{A}\boldsymbol{c}, \tag{4.63}$$

and with $\boldsymbol{b} = \boldsymbol{w}$, $\boldsymbol{A} = \mathbb{C}\left[\nabla\boldsymbol{u} + \boldsymbol{\chi}\right]$, and $\boldsymbol{c} = \boldsymbol{n}$, Equation (4.64) can be expressed as

$$\int_{\Omega} -\nabla\boldsymbol{w} \cdot \mathbb{C}\left[\nabla\boldsymbol{u} + \boldsymbol{\chi}\right]\ \mathrm{dV} + \int_{\partial\Omega} \boldsymbol{w} \cdot \left(\mathbb{C}\left[\nabla\boldsymbol{u} + \boldsymbol{\chi}\right]\boldsymbol{n}\right)\ \mathrm{da} - \int_{\mathrm{A}^{\mathrm{t}}} \boldsymbol{w} \cdot \left(\mathbb{C}\left[\nabla\boldsymbol{u} + \boldsymbol{\chi}\right]\boldsymbol{n} - \boldsymbol{s}^{\mathrm{p}}\right)\ \mathrm{da} = 0. \tag{4.64}$$

The surface $\partial\Omega$ is the union of A^{u} and A^{t}. As mentioned previously, the displacement on A^{u} will be prescribed a priori, so the surface integral over $\partial\Omega$ can be replaced with a surface integral over A^{t}. This allows the integral over $\partial\Omega$ to cancel with the first term in the boundary condition integral over A^{t} in Equation (4.64). The resulting equation is

$$\int_{\Omega} -\nabla\boldsymbol{w} \cdot \mathbb{C}\left[\nabla\boldsymbol{u} + \boldsymbol{\chi}\right]\ \mathrm{dV} + \int_{\mathrm{A}^{\mathrm{t}}} \boldsymbol{w} \cdot \boldsymbol{s}^{\mathrm{p}}\ \mathrm{da} = 0. \tag{4.65}$$

The linearity of both $\mathbb{C}$ and the dot product allows Equation (4.65) to be equivalently expressed as

$$\int_{\Omega} \left(-\nabla\boldsymbol{w} \cdot \mathbb{C}\left[\nabla\boldsymbol{u}\right] - \nabla\boldsymbol{w} \cdot \mathbb{C}\left[\boldsymbol{\chi}\right]\right)\ \mathrm{dV} + \int_{\mathrm{A}^{\mathrm{t}}} \boldsymbol{w} \cdot \boldsymbol{s}^{\mathrm{p}}\ \mathrm{da} = 0. \tag{4.66}$$

Since Equation (4.65) should hold over the entire domain, we can enforce it upon individual elements. At this point shape functions will be introduced to facilitate the finite element formulation. Let the displacement vector at any position inside an element be represented by the dot product of the shape functions evaluated at that position and the corresponding nodal displacements, or

$$\boldsymbol{u} = \mathrm{N}^{\mathrm{A}}\boldsymbol{u}_k^{\mathrm{A}} \tag{4.67}$$

where A is the index of the shape function, i.e. the sum will include as many terms as there are shape functions. The weighting function can be expressed in a similar fashion by

$$\boldsymbol{w} = \mathrm{N}^{\mathrm{B}}\boldsymbol{w}_i^{\mathrm{B}} \tag{4.68}$$

where B is the index of the shape function. Differentiating Equations (4.67) and (4.68) leads to

$$\nabla \boldsymbol{u} = \frac{\partial u_k}{\partial x_l} = \frac{\partial \mathrm{N}^{\mathrm{A}}}{\partial x_l} \boldsymbol{u}_k^{\mathrm{A}} \tag{4.69}$$

and

$$\nabla \boldsymbol{w} = \frac{\partial w_i}{\partial x_j} = \frac{\partial \mathrm{N}^{\mathrm{B}}}{\partial x_j} \boldsymbol{w}_i^{\mathrm{B}}. \tag{4.70}$$

Equations (4.69) and (4.70) can be substituted into the body integral of Equation (4.66), which can be enforced over each element and is expressed in its indicial form

$$-\int_{\Omega_{\mathrm{e}}} \frac{\partial \mathrm{N}^{\mathrm{B}}}{\partial x_j} w_i^{\mathrm{B}} \, \mathbb{C}_{ijkl} \, \frac{\partial \mathrm{N}^{\mathrm{A}}}{\partial x_l} u_k^{\mathrm{A}} \, \mathrm{dV} - \int_{\Omega_{\mathrm{e}}} \frac{\partial \mathrm{N}^{\mathrm{B}}}{\partial x_j} w_i^{\mathrm{B}} \, \mathbb{C}_{ijkl} \, \chi_{kl} \, \mathrm{dV} = 0 \tag{4.71}$$

The surface integral from Equation (4.66) will be evaluated over the appropriate boundary faces. The arbitrary weighting function, w_i^{B}, and the nodal displacements, u_k^{A}, can be pulled out of each integral since their values do not dependent on position inside the element. Each term can then be divided by the weighting function, which will effectively remove it from the expression. Moving the second term to the right hand side of the equation leads to

$$\left(\int_{\Omega_{\mathrm{e}}} \frac{\partial \mathrm{N}^{\mathrm{B}}}{\partial x_j} \frac{\partial \mathrm{N}^{\mathrm{A}}}{\partial x_l} \, \mathbb{C}_{ijkl} \, \mathrm{dV} \right) u_k^{\mathrm{A}} = \left(- \int_{\Omega_{\mathrm{e}}} \frac{\partial \mathrm{N}^{\mathrm{B}}}{\partial x_j} \, \mathbb{C}_{ijkl} \, \chi_{kl} \, \mathrm{dV} \right). \tag{4.72}$$

where the quantity in the parenthesis on the left is the local stiffness matrix and the quantity in the parenthesis on the right is the local load vector. The incompatible elastic distortion is essentially acting as a load vector on the displacements.

4.2 Inverse Problem Formulation

The forward problem of calculating the strain field from a known dislocation distribution has been laid out in Section 4.1. The inverse problem of determining a dislocation distribution from a known strain field will require the use of nonlinear programming. The goal here is to determine the underlying dislocation fields that are causing the residual strains presented in Chapter 3. Knowledge of the dislocation distributions will lead to a deeper understanding of the material state. It could be argued that since the strain fields have already been measured there is little additional value added upon determining the dislocation distributions. The hope is that as the technique is developed further the number of strain measurements can be reduced without losing information about the full strain field. This could mean reducing the number of strain components that are measured, or reducing the number of spatial locations where strain is measured.

Inverse problems are solved for both the AA7075 and Ti-64 samples. To isolate residual strains, only measurements taken in the absence of applied loads are considered. A calculation domain is first discretized into a mesh of nodes that are connected together to make elements. It should be noted that the entire samples must be included in the calculation domain so that appropriate boundary conditions can be established. Stress free boundary conditions are suitable for the equilibrium BVP since there are no external loads, and $\boldsymbol{\chi n} = 0$ is taken as the boundary condition anywhere a material ends for the incompatible elastic distortion BVP. Each node is assigned an $\tilde{\boldsymbol{\alpha}}$ tensor consisting of 9 independent values. For thin samples under plane stress conditions only dislocations with an in plane (x-y) Burgers vector and an out of plane dislocation line (z), i.e. $\tilde{\alpha}_{13}$ and $\tilde{\alpha}_{23}$, are significant to the strain calculation. In each iteration of the inverse problem the least squares finite element formulation described in Section 4.1.1 is used to solve for $\boldsymbol{\chi}$. The calculated $\boldsymbol{\chi}$ is then used in the equilibrium problem described in Section 4.1.2 to calculate the displacements. Once the displacement field is known the in-plane strain components are calculated and then compared with the XRD measurements. It can be proven that a constant dislocation distribution will produce a strain field that is equal to zero everywhere [11]. This result ensures that a one-to-one mapping between strain fields and dislocation distributions does not exist, as any strain field will be unchanged by adding a constant value to the entire dislocation distribution. In mathematical terms this means that the inverse problem of determining a dislocation distribution causing a strain field has infinite solutions, and is thus ill-posed. To create a well-posed problem the dislocation distribution must be pinned down in some fashion to remove the addition of an arbitrary constant dislocation distribution. To these ends, constraints are added such that the square of the dislocation distribution integrals are within a set tolerance to zero across the domain.

The optimization problem is stated as

$$\begin{aligned} &\underset{p}{\text{minimize}} \quad f(p) \\ &\text{such that} \quad g_i(p) \leq 0,\ i = 1,2 \end{aligned} \tag{4.73}$$

where the objective function is given by

$$f(p) = \sum_{j}^{N_{\text{node}}} \left(\varepsilon^{\text{e(j)}}_{xx,\text{meas}} - \varepsilon^{\text{e(j)}}_{xx,\text{calc}}\right)^2 + \left(\varepsilon^{\text{e(j)}}_{yy,\text{meas}} - \varepsilon^{\text{e(j)}}_{yy,\text{calc}}\right)^2 + \left(\varepsilon^{\text{e(j)}}_{xy,\text{meas}} - \varepsilon^{\text{e(j)}}_{xy,\text{calc}}\right)^2 \tag{4.74}$$

and the constraint functions are given by

$$g_1(p) = \left(\int_{\Omega} \tilde{\alpha}_{13}\ \text{dV}\right)^2 - \rho \tag{4.75}$$

$$g_2(p) = \left(\int_{\Omega} \tilde{\alpha}_{23}\ \text{dV}\right)^2 - \rho \tag{4.76}$$

where Ω is the calculation domain and ρ is the desired tolerance. The dislocation densities can be assumed to be constant with z-coordinate since only edge dislocations with dislocation lines along the z-axis are considered. Each line of nodes with a common x- and y-coordinate, but varying z-coordinates, is assumed to have the same $\tilde{\boldsymbol{\alpha}}$. The number of optimization parameters becomes $2\ N_x\ N_y$ where N_x is the number of nodes in the x-direction and N_y is the number of nodes in the y-direction.

4.3 Aluminum Alloy 7075 Results

The first objective is to show that the inverse problem formulation outlined in Section 4.2 is capable of producing realistic $\tilde{\boldsymbol{\alpha}}$ distributions from input strain measurements. Taking the calculation domain to be the whole sample, which is necessary to determine appropriate boundary conditions, is problematic considering that XRD measurments were only taken in a small region in the center of the sample. This problem will be initially addressed by replacing the XRD measurements with results from a finite element simulation of the experiment. It is understood that in practice this would defeat the purpose of solving the inverse problem, but it will serve to meet the first objective.

The commercial software package ABAQUS was used to solve for displacements in an elasto-plastic finite element simulation. The AA7075 sample was considered the computational domain and a perfectly plastic assumption was used with a yield stress of 500 MPa. Pressure loads were applied at the location of each load pin with equal magnitudes such that the calculated strains were very similar to the experimental strains for the 4th load step which corresponded with 3 complete turns of the actuation screw. Residual strains were then calculated in ABAQUS by removing the pressure loads. Scatter plots of the XRD strain measurements from both the loaded and unloaded states are presented in Figure 4.1. These same results were presented in Chapter 3 as a line plot, but a scatter plot is better suited here so that the size of the XRD measurement region can be compared with the computational domain from the ABAQUS simulation. Scatter plots of the strains calculated from ABAQUS in the loaded and unloaded state are presented in Figure 4.3. The XRD and ABAQUS strains are compared quantitatively in Figure 4.4, and it is clear from these plots that the data sets from both load steps are in close agreement, i.e. ABAQUS was able to accurately predict the residual strains upon removing the pressure loads.

A dislocation distribution was calculated by solving the inverse problem outlined in Section 4.2 using the residual strains from the ABAQUS simulation as the measured data. It was determined through initial coarse simulations that the $\tilde{\alpha}_{23}$ values remained very close to zero, and so to reduce computational cost only the $\tilde{\alpha}_{13}$ values were optimized in the results presented here. As such the number of optimization parameters is reduced from $2\ N_x\ N_y$ to $N_x\ N_y$ and only the first constraint from Equation (4.75) is enforced. The AA7075 sample was discretized into a 3D mesh consisting of 20 elements in the x-direction, 10 elements in the y-direction, and 2 elements in the z-direction. The mesh is pictured in the x-y plane with an equal aspect raio in Figure 4.1. Matlab was used to solve both BVPs for the incompatible elastic distortion and displacement fields. The global stiffness matrices for each BVP are only factored once at the beginning of the optimization, which reduced the computation time of one iteration by about an order of magnitude, yet computation time was still a limiting factor in the resolution of the simulations. As the mesh is refined there is an increase in computation time for each iteration, which includes solving both BVPs, along with an increased number of parameters and therefore number of iterations necessary to find a local minimum. These two effects combine to create a rapid increase in computation time as the mesh is refined. The optimized strain contours, comparison between ABAQUS and optimized strains, and the optimized $\tilde{\alpha}_{13}$ distribution is presented in Figure 4.5. The optimization succeeded in matching the ABAQUS reasonably well for each component of strain, especially considering the coarseness of the mesh. Further, the optimized $\tilde{\alpha}_{13}$ distribution has a physical analogy which will be discussed in Section 4.5.

One of the goals of this project is to reduce the number of XRD measurements needed to gain a full understanding of a residual stress state. To these ends, a very similar optimization was performed using the ABAQUS data in which only $\varepsilon^{\mathrm{e}}_{xx}$ was compared with the optimized strains in the objective function, i.e.

$$f(p) = \sum_{j}^{N_{\mathrm{node}}} \left(\varepsilon^{\mathrm{e(j)}}_{xx,\mathrm{meas}} - \varepsilon^{\mathrm{e(j)}}_{xx,\mathrm{calc}}\right)^2 . \tag{4.77}$$

Results from this optimization are presented in Figure 4.6. As before, the optimization was able to match all three components of strain and produce a realistic $\tilde{\alpha}_{13}$ distribution. It appears that very little information about the material state was lost by only comparing the $\varepsilon^{\mathrm{e}}_{xx}$ rather than all three strain components. It should be noted that $\varepsilon^{\mathrm{e}}_{xx}$ was the dominant component of strain, but the algorithm's ability to infer almost the same dislocation behavior using only one component of strain is promising.

The next step is to investigate the behavior of the optimized solution when the input measurements do not cover the whole computational domain, as would be the case in practice. For this optimization problem the XRD measurements presented in Chapter 3 are compared with the calculated strains, and so only nodes in the center of the sample where XRD measurements were taken are considered in the objective function. This technique leaves much of the domain uncontrolled. The results from the optimization are displayed in Figure 4.7. These results show that a significant amount of information is lost through only supplying the objection function with the XRD measurements. The strain field is matched quite well inside the XRD measurement region, but the optimized strains do not follow the behavior suggested by the ABAQUS model outside of the measurement region. The optimization has no way of knowing that the strain field trends to zero quickly outside of the load pins, and the optimized $\tilde{\alpha}_{13}$ behavior appears to be somewhat random without a physical basis.

The ABAQUS model displayed strain contours that were constant with x-coordinate inside the load pins, but rapidly decayed outside of them. To guide the simulation towards the true strain field columns of zero strain values were added to the XRD measurements as displayed in Figure 4.8. The actual strain values would not be exactly zero here, but zero will serve as a close enough approximation. This technique seems to help the optimization reach the strain field, as displayed by the results in Figure 4.9. The addition of the zero strain values gives enough information to the optimizer so that an appropriate dislocation arrangement can be determined. The overall character of the strain behavior was captured by the input measurements and thus an accurate representation was obtained from the optimization. Results from an optimization that used the technique of adding zero values but only optimized against $\varepsilon^{\mathrm{e}}_{xx}$ are presented in Figure 4.10. It appears that restricting two components of strain caused the optimization to severely misrepresent the strain behavior outside the measurement region, despite its reasonable match inside the measurement region. It cannot be concluded whether this trend will hold for all loading conditions, but for the case of four-point bending it is important to supply multiple strain components that characterize the full field residual strain behavior.

The results suggest that the inverse problem formulated here is very capable of determining an $\tilde{\alpha}$ distribution to match a strain field if the objective function is supplied with the entire strain field. If measurements are supplied from a small region such that behavior outside the region is not captured at all, the optimization behaves poorly. The key finding, however, is that the optimization can reasonably match the full strain field if enough measurements are supplied such that the essence of the strain behavior is captured by the measurements.

4.4 Titanium-6Al-4V Results

The dislocation distribution inverse problem was only solved for the Ti-64 α-phase, since the β-phase elastic properties are not known. The main contrast with the AA7075 results is the strain concentrations caused by the notches machined into the samples. The mesh used for these calculations is pictured in Figure 4.11. The behavior of the strain field is such that it reaches a maximum at the horizontal location of the notches, and then decays towards the left and right boundaries. The XRD measurements are presented again in Figure 4.12, with the x- and y-limits of the plot set such that the measurement region can be compared with the size of the sample. The strain behavior turned out to be significant in that the Ti-64 XRD measurements showed a trend toward zero strain that was not exhibited by the AA7075 measurements. In short, the essence of the strain behavior over the entire specimen is captured by the strain measurements, and so adding additional zero strain data points to guide the solution was not necessary. The results from an optimization that only considered the XRD measurements in the objective function are displayed in Figure 4.13. The results of this optimization support the conjecture made in Section 4.3; the essence of the full field strain behavior was captured by the measurements that were accessed by the objective function, and therefore the optimization was able to reasonably match the full field strain behavior with a realistic dislocation distribution. Another calculation was performed that only used the $\varepsilon^{\mathrm{e}}_{xx}$ component of the XRD measurements in the objective function. The results from this optimization, presented in Figure 4.14, show a deteriorated agreement between the measured and calculated strains. Further, unrealistic oscillations are seen in the $\tilde{\alpha}_{13}$ distribution. As was the case with the AA7075 results, it appears that multiple strain components that capture the essence of the full field strain behavior are required for the optimization to produce a reasonable match with the experiment.

4.5 Comparison of Dislocation Modeling Techniques

Until now the only method for optimizing a dislocation arrangement to match a strain field is that of continuum dislocations presented in Sections 4.1-4.2. Throughout the course of the project, however, a method utilizing discrete dislocations was also extensively studied. In this method the analytical solution for a plane-strain edge dislocation in an infinite plate was employed. The linearity of the analytical dislocation strain field allows the strain field from an arrangement of dislocations to be calculated through superposing the strain fields from each individual dislocation. A sample of code that performs this calculation is given in Appendix B. A set number of in-plane discrete edge dislocations were placed in a computational domain. The x-location, y-location, Burgers vector magnitude, and orientation of each dislocation was treated as an optimization parameter leading to $4\mathrm{N_d}$ parameters for $\mathrm{N_d}$ dislocations. The parameters were varied until a local minimum in the difference between the calculated and measured strain values was reached. The downfall of the method comes when strains near the boundary are desired. The analytical solutions used in the calculation are derived from an infinite plate assumption. In order to mimic a material boundary image dislocations were used to enforce zero stress boundary conditions. Image dislocations are a mirror image of a dislocation located on the opposite side of a free surface. The strain calculation simply superposes the image dislocation strain field with the original dislocation strain field. Image dislocation behavior is not entirely physical though as each component of stress is set to zero at the boundaries, rather than just the normal stress. This method is much easier to code and orders of magnitude faster to compute.

Despite the simplicity of the method, the optimized strains agreed quite well with measured strains. Contours of the measured strain components are compared with the optimized strain contours for the AA7075 sample in Figure 4.15. The optimized discrete dislocations are overlaid on the calculated strain contours. The measured and calculated strains are compared along the $x = 0$ line in Figure 4.17. Free surface boundaries were placed at the minimum and maximum y-coordinate of the measured data points, which explain why each strain component approaches zero at the minimum and maximum y-coordinate. The calculation domain only included the measurement region since vertical free surfaces could easily be excluded on the left and right side of the measurement region. The physical representation of the $\tilde{\alpha}_{13}$ distribution discussed in Section 4.3 is easier to see here. Comparing the $\tilde{\alpha}_{13}$ distribution given in Figure 4.5 with the discrete dislocations displayed in Figure 4.15 gives insight to a physical representation. Regions of negative $\tilde{\alpha}_{13}$ located near the top and bottom of the domain in Figure 4.5 correspond to the negative edge dislocations in Figure 4.15, while the region of positive $\tilde{\alpha}_{13}$ located in the middle of the domain in Figure 4.5 corresponds to the positive edge dislocations in Figure 4.15. The method lost some accuracy when only the $\varepsilon^{\mathrm{e}}_{xx}$ measurements were supplied to the objective function. Strain contours are displayed in Figure 4.16, and a line plots comparing the XRD measurements to the optimized strains is in Figure 4.18. At first glance there is an obvious discrepancy between the measured and calculated $\varepsilon^{\mathrm{e}}_{xy}$. This could be due to the lack of a periodic boundary condition, which would be more appropriate since the effect of material on both sides of the domain is not included in the model. The trend in the $\varepsilon^{\mathrm{e}}_{yy}$ calculation matches that of the measurements, despite this component being withheld from the objective function.

Discrete dislocation optimization results for the Ti-64 sample are displayed in Figure 4.19. Only contour plots from this calculation are presented as the inherent 2D nature of the strain fields caused by the notches prevents a line plot from conveying the ability of the method. It is clear from these contours that the magnitudes are not in close agreement, but the overall trends are captured. More interestingly, the trends in all three strain components are still captured when only the $\varepsilon^{\mathrm{e}}_{xx}$ component is supplied to the objective function, as seen in the results presented in Figure 4.20. The discrete dislocation method proved to be useful to quickly determine an approximate layout of the dislocation distribution, and was reliable if strain values are desired “far” from a boundary. In real applications this will likely not be the case as boundary behavior is especially important to fatigue behavior. To calculate realistic full field behavior both BVPs must be solved so that equilibrium is ensured and boundary conditions are enforced. That is not to say that the discrete dislocation optimization does not have its place as a quick first calculation.

4.6 Figures

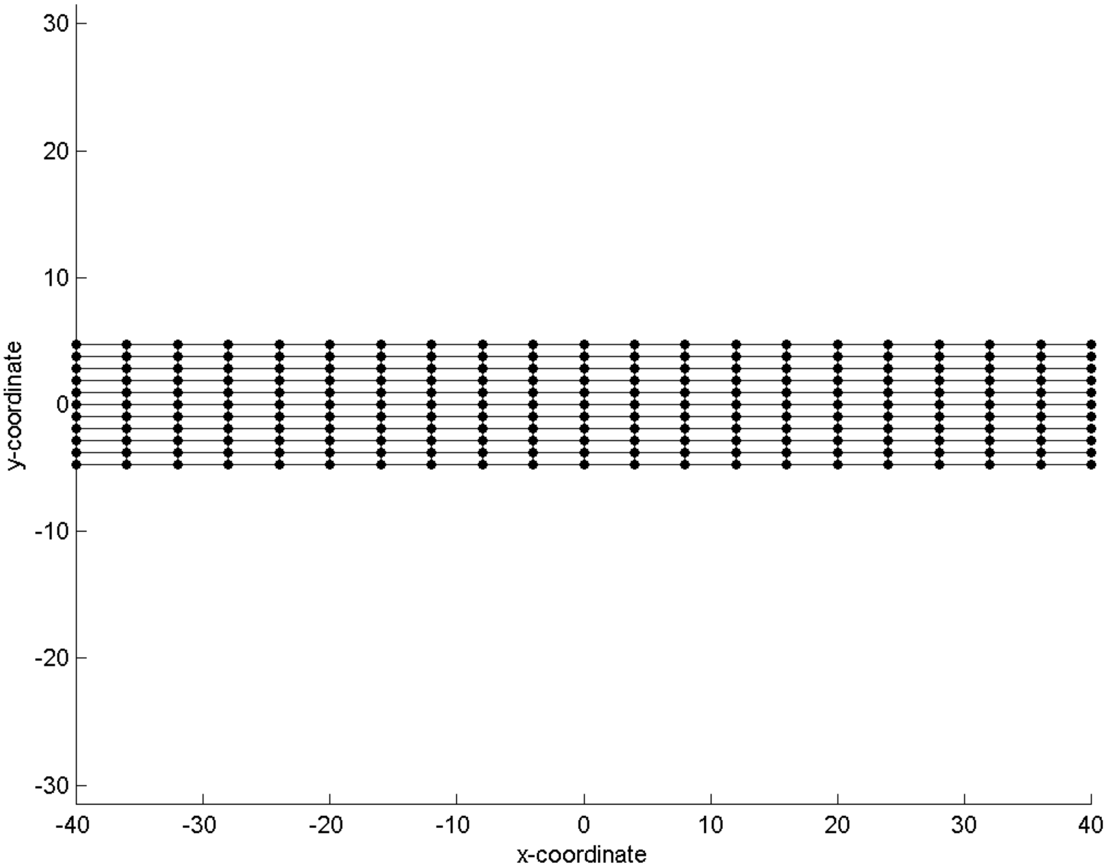

Figure 4.1 Mesh Used for AA7075 Continuum Dislocation Calculations

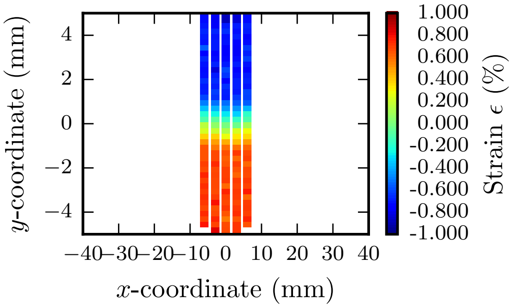

(a) Loaded XRD ε^{e}_{xx}

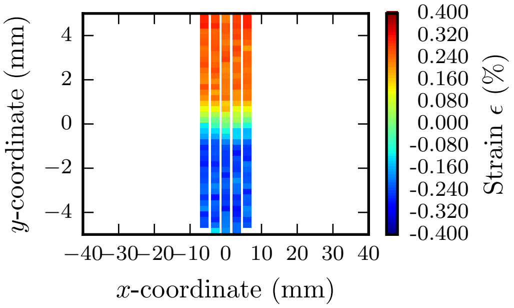

(b) Loaded XRD ε^{e}_{yy}

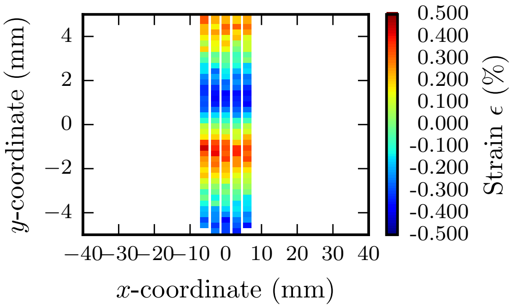

(c) Residual XRD ε^{e}_{xx}

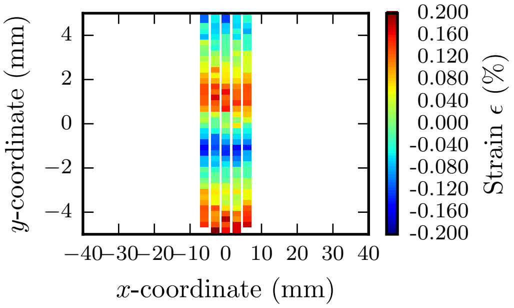

(d) Residual XRD ε^{e}_{yy}

Figure 4.2 AA7075 XRD Measurements

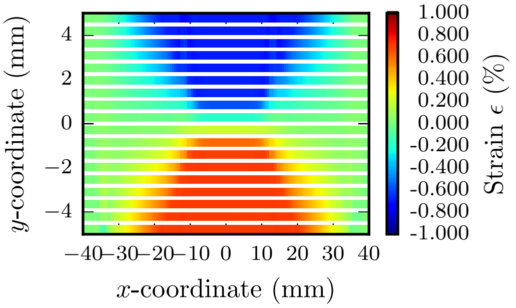

(a) Loaded ABAQUS ε^{e}_{xx}

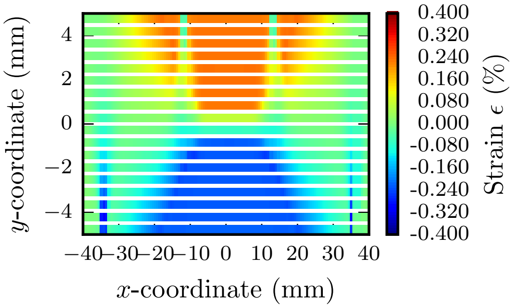

(b) Loaded ABAQUS ε^{e}_{yy}

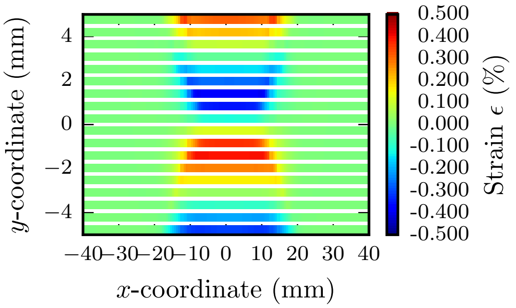

(c) Residual ABAQUS ε^{e}_{xx}

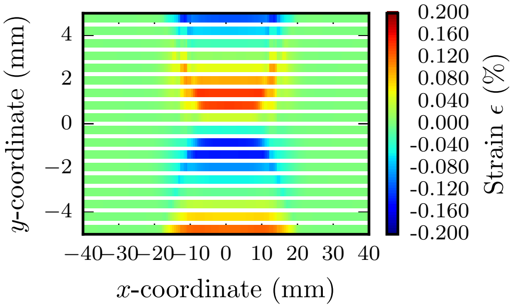

(d) Residual ABAQUS ε^{e}_{yy}

Figure 4.3 ABAQUS Calculations

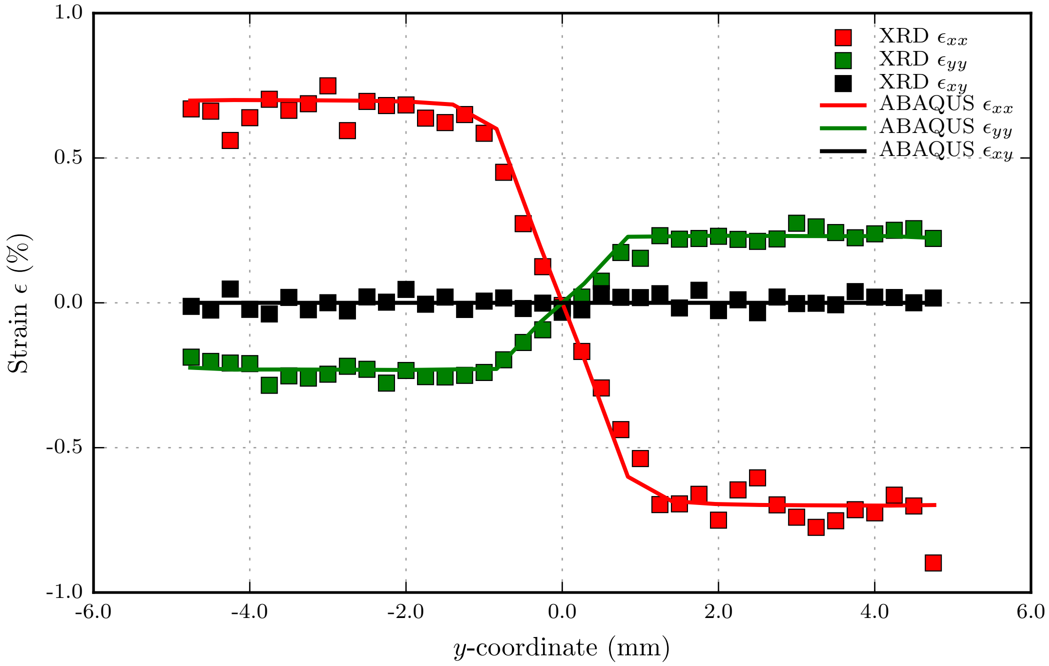

(a) Loaded State

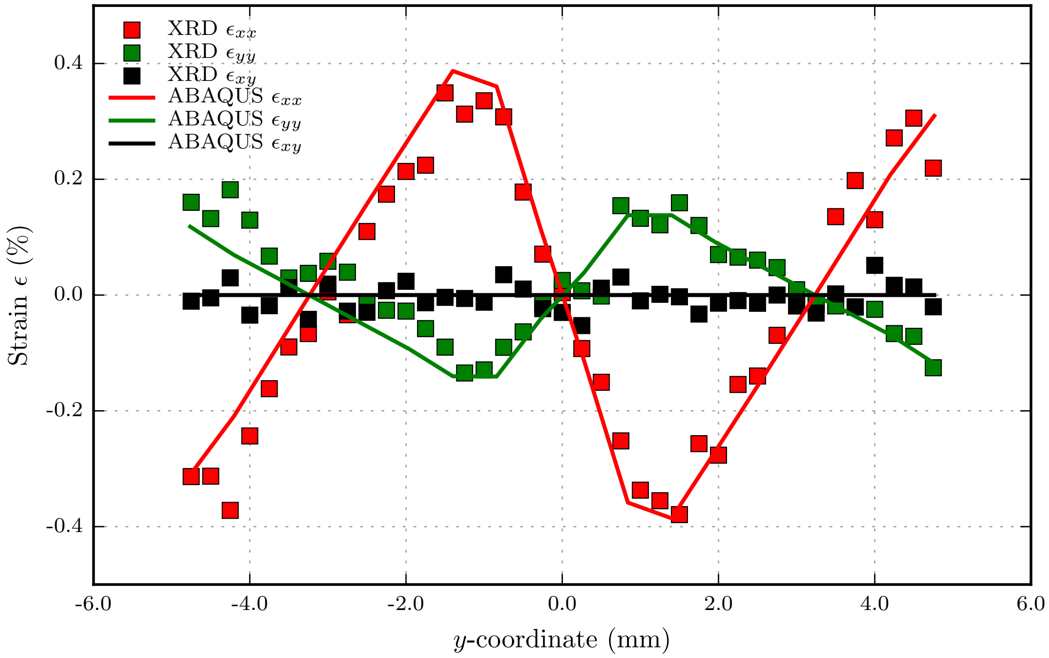

(b) Residual State

Figure 4.4 Comparison of AA7075 XRD Measurements to ABAQUS Calculations

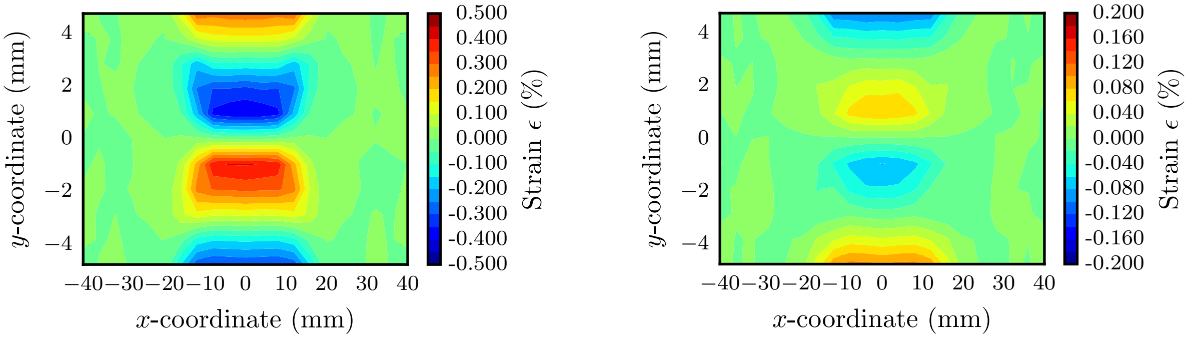

(a) Optimized $\varepsilon^{\mathrm{e}}_{xx}$

(b) Optimized $\varepsilon^{\mathrm{e}}_{yy}$

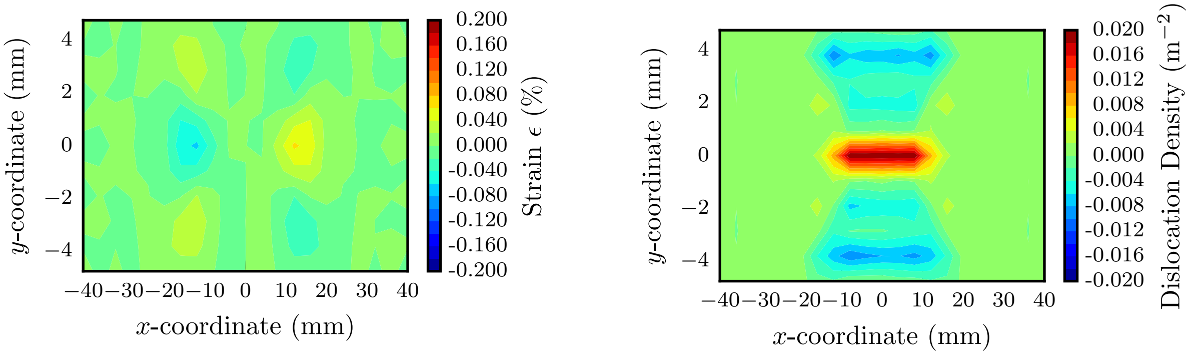

(c) Optimized $\varepsilon^{\mathrm{e}}_{xy}$

(d) Optimized $\tilde{\alpha}_{13}$ Distribution

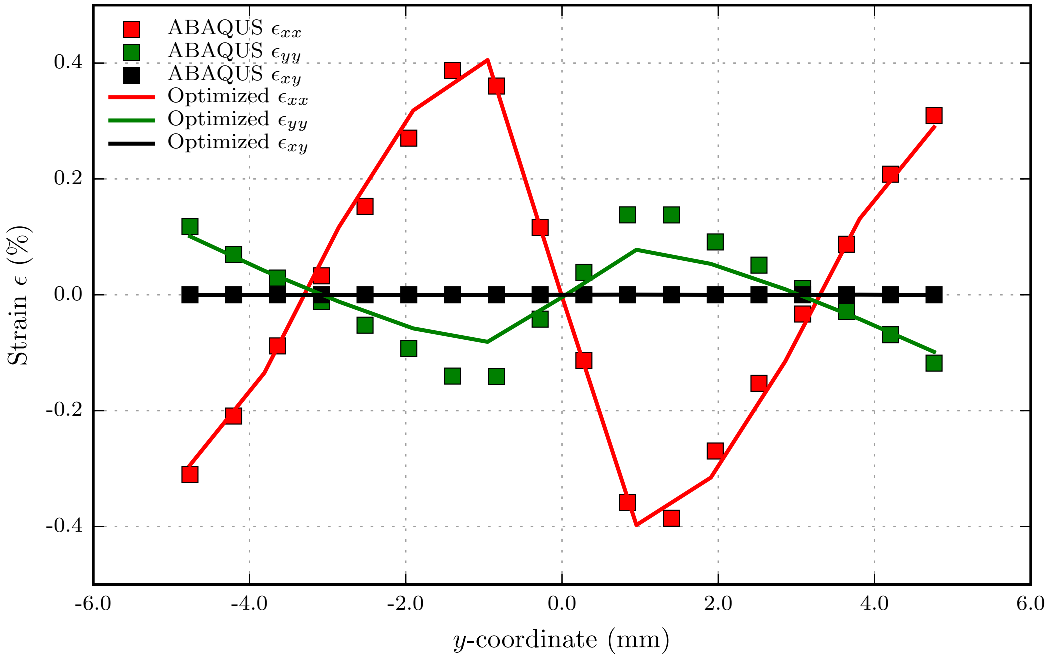

(e) Comparison of ABAQUS ε^{e} and Optimized ε^{e} Along $x = 0$

Figure 4.5 ABAQUS Optimization Results

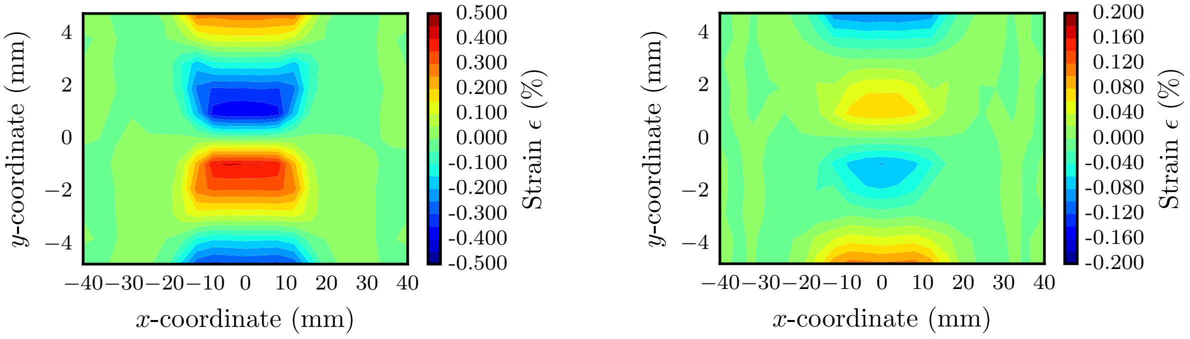

(a) Optimized $\varepsilon^{\mathrm{e}}_{xx}$

(b) Optimized $\varepsilon^{\mathrm{e}}_{yy}$

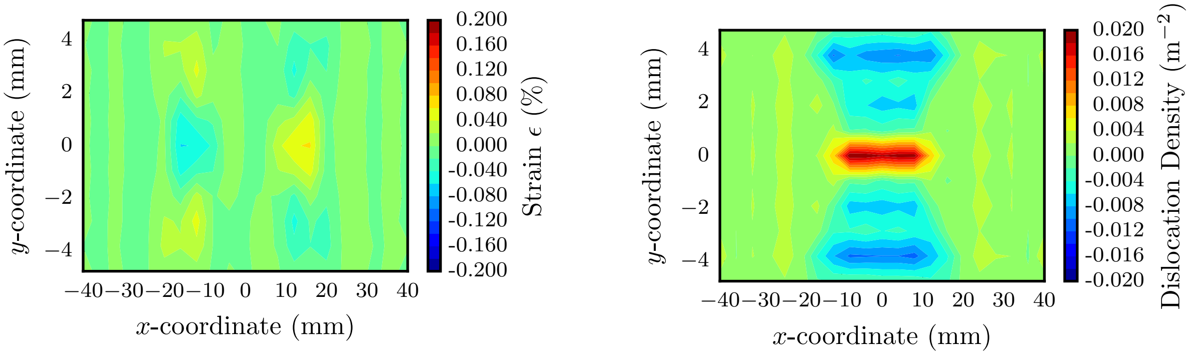

(c) Optimized $\varepsilon^{\mathrm{e}}_{xy}$

(d) Optimized $\tilde{\alpha}_{13}$ Distribution

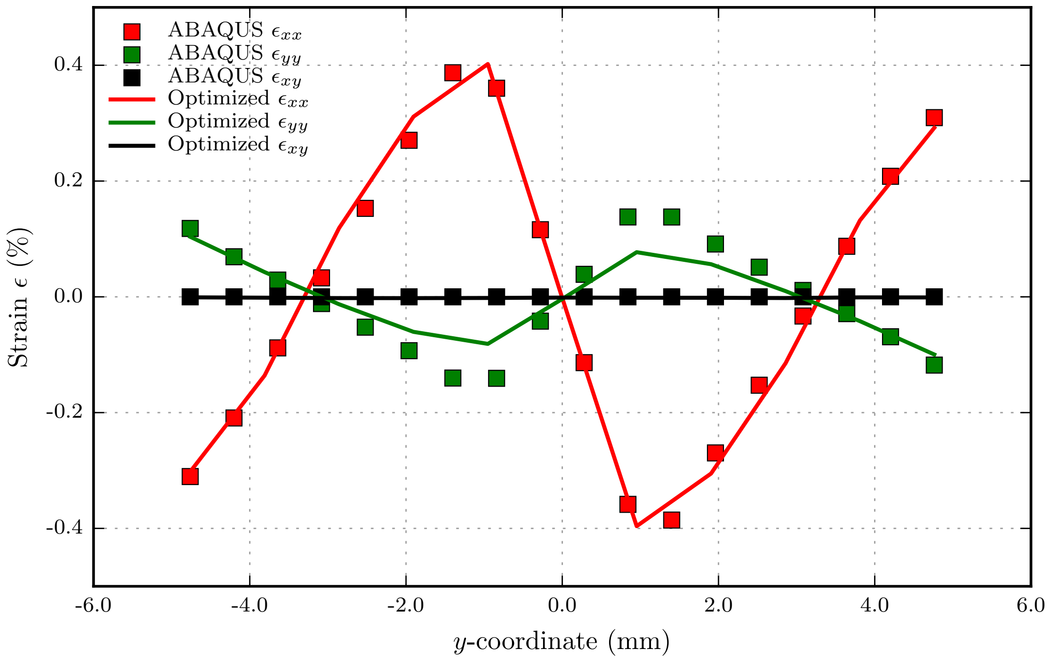

(e) Comparison of ABAQUS ε^{e} and Optimized ε^{e} Along $x = 0$

Figure 4.6 ABAQUS Comparing $\varepsilon^{\mathrm{e}}_{xx}$ Only Optimization Results

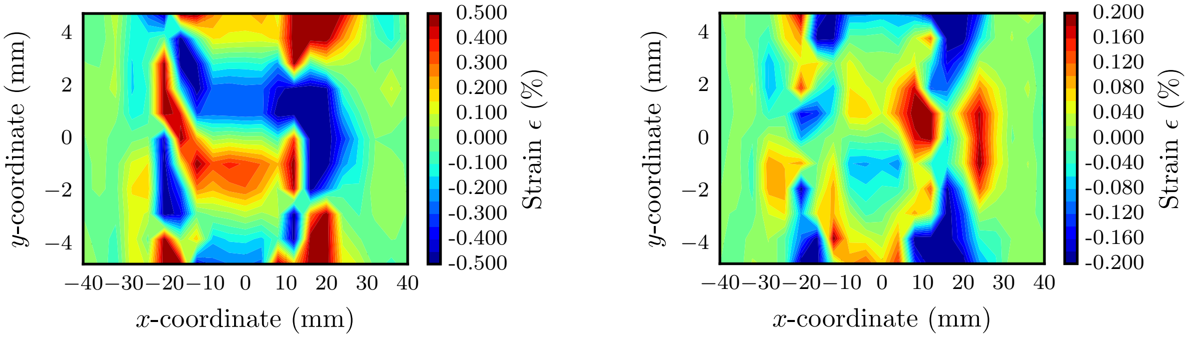

(a) Optimized $\varepsilon^{\mathrm{e}}_{xx}$

(b) Optimized $\varepsilon^{\mathrm{e}}_{yy}$

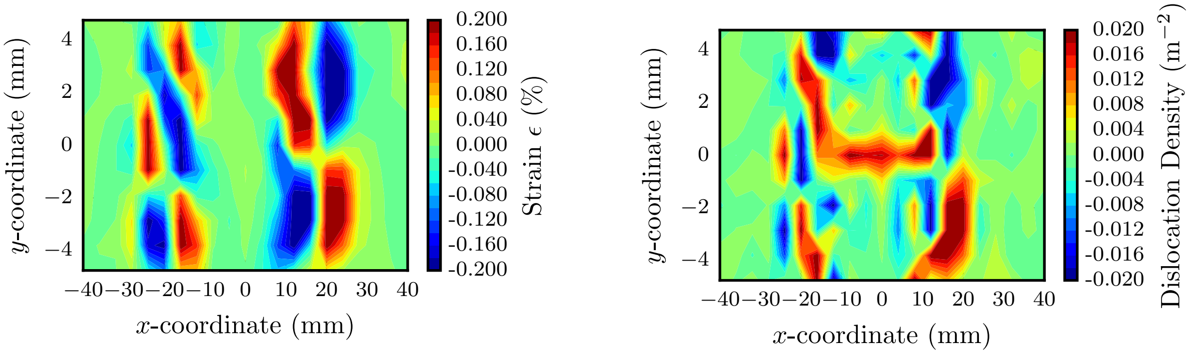

(c) Optimized $\varepsilon^{\mathrm{e}}_{xy}$

(d) Optimized $\tilde{\alpha}_{13}$ Distribution

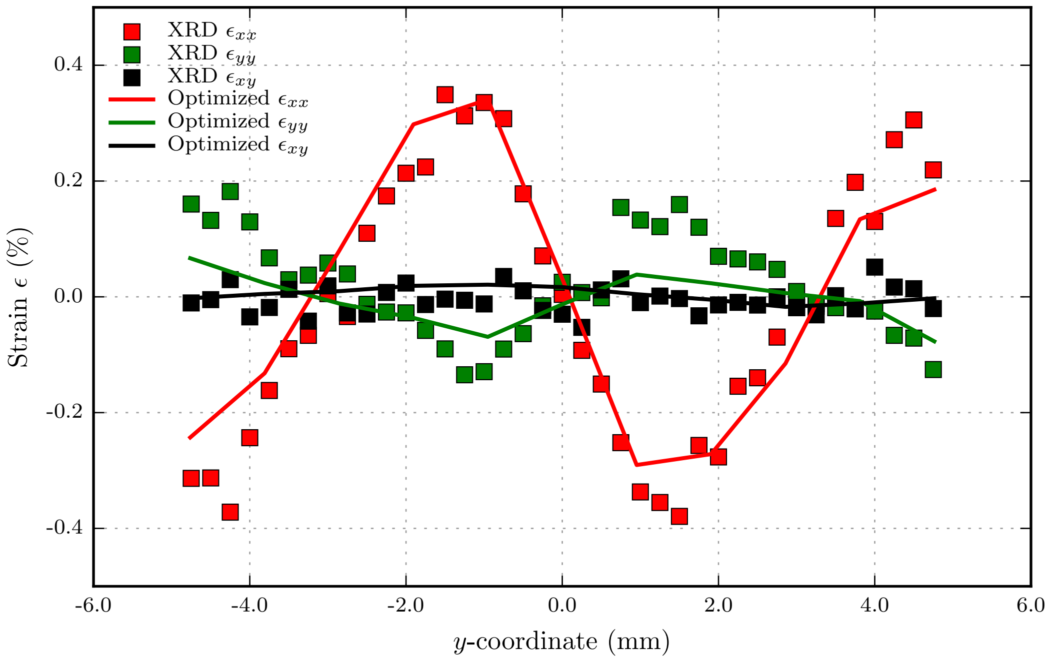

(e) Comparison of XRD ε^{e} and Optimized ε^{e} Along $x = 0$

Figure 4.7 AA7075 XRD Measurements Optimization Results

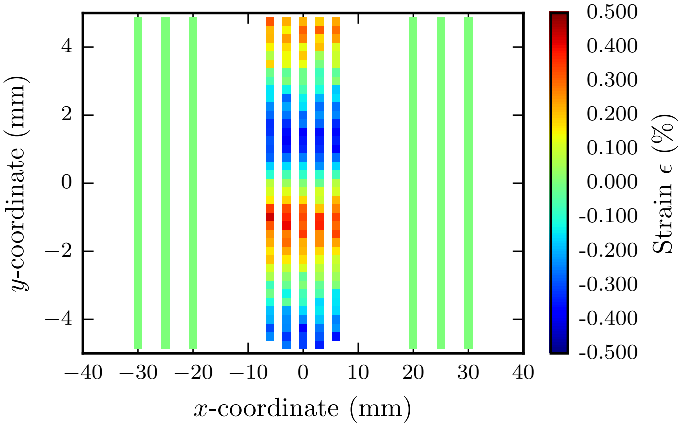

(a) Zeros Added to $\varepsilon^{\mathrm{e}}_{xx}$ Measurements

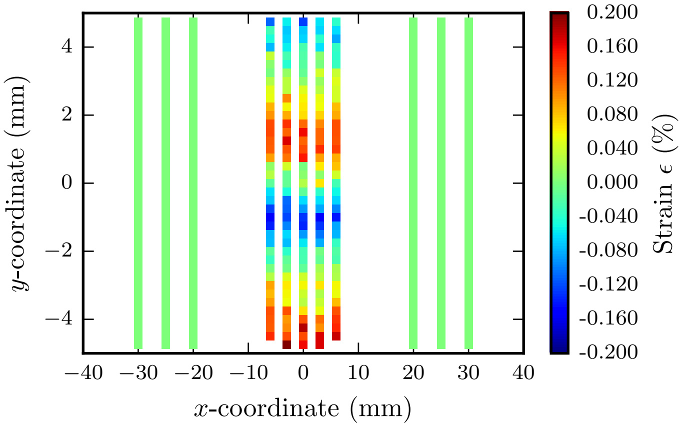

(b) Zeros Added to $\varepsilon^{\mathrm{e}}_{yy}$ Measurements

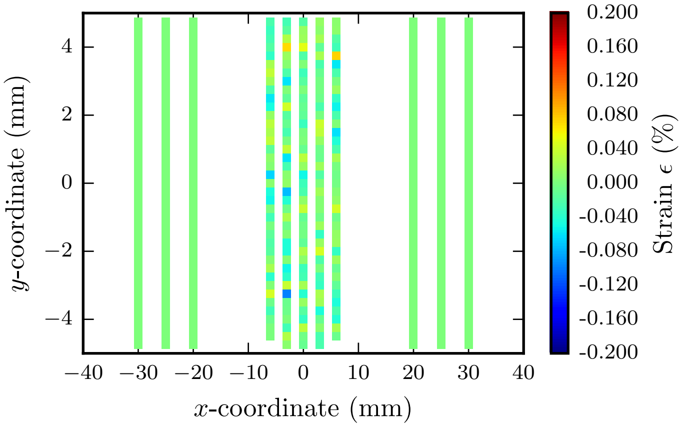

(c) Zeros Added to $\varepsilon^{\mathrm{e}}_{xy}$ Measurements

Figure 4.8 Zeros Added to AA7075 XRD Measurements

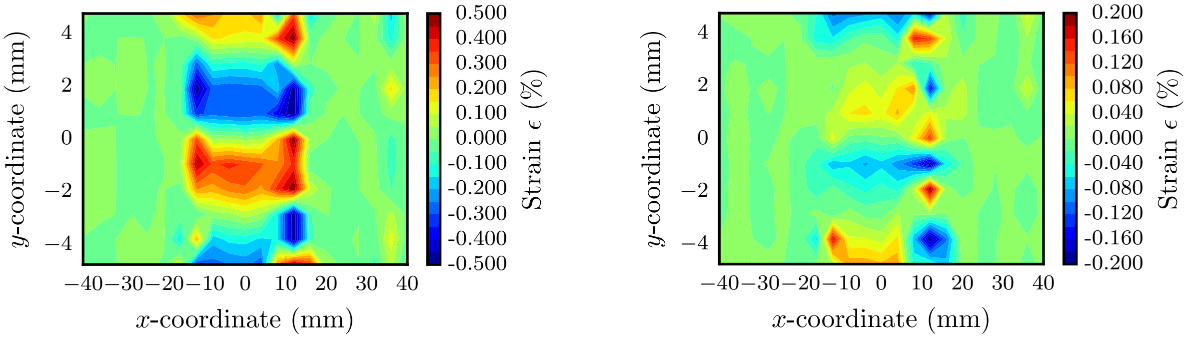

(a) Optimized $\varepsilon^{\mathrm{e}}_{xx}$

(b) Optimized $\varepsilon^{\mathrm{e}}_{yy}$

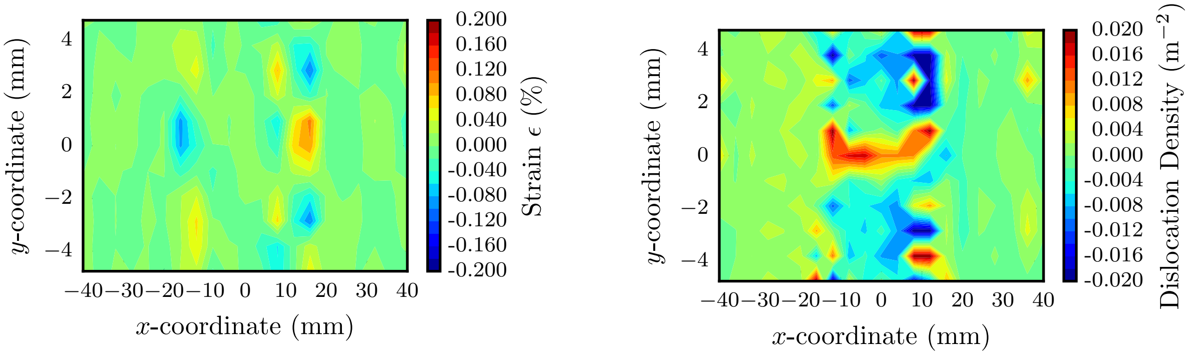

(c) Optimized $\varepsilon^{\mathrm{e}}_{xy}$

(d) Optimized $\tilde{\alpha}_{13}$ Distribution

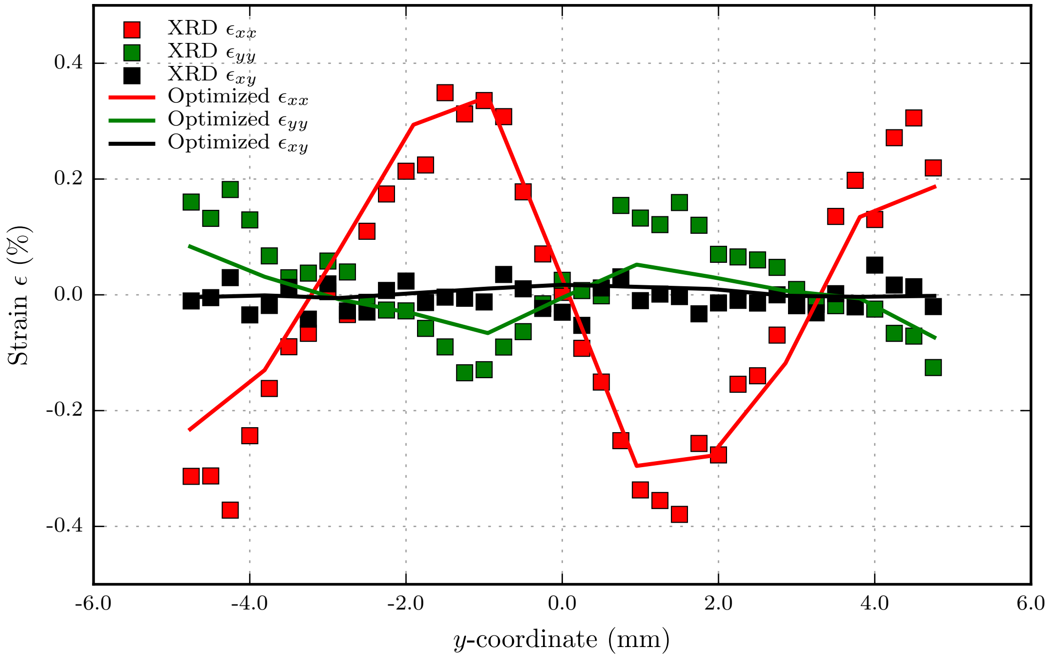

(e) Comparison of XRD ε^{e} and Optimized ε^{e} Along $x = 0$

Figure 4.9 AA7075 XRD Measurements With Added Zeros Optimization Results

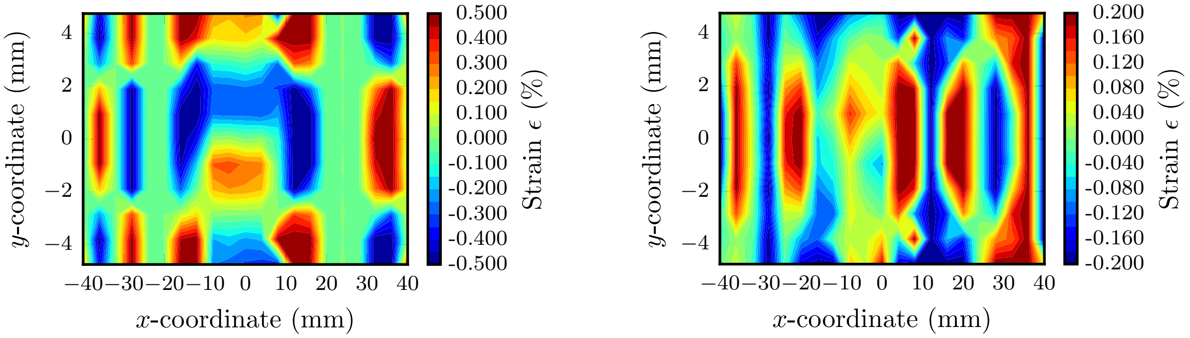

(a) Optimized $\varepsilon^{\mathrm{e}}_{xx}$

(b) Optimized $\varepsilon^{\mathrm{e}}_{yy}$

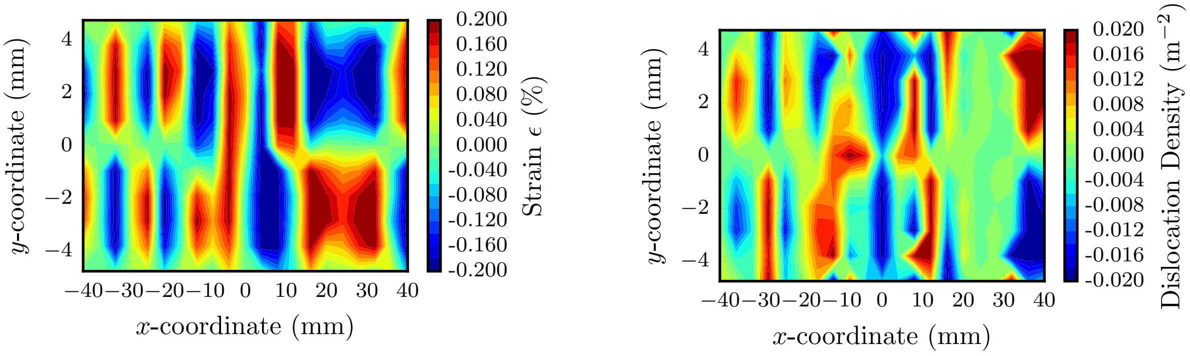

(c) Optimized $\varepsilon^{\mathrm{e}}_{xy}$

(d) Optimized $\tilde{\alpha}_{13}$ Distribution

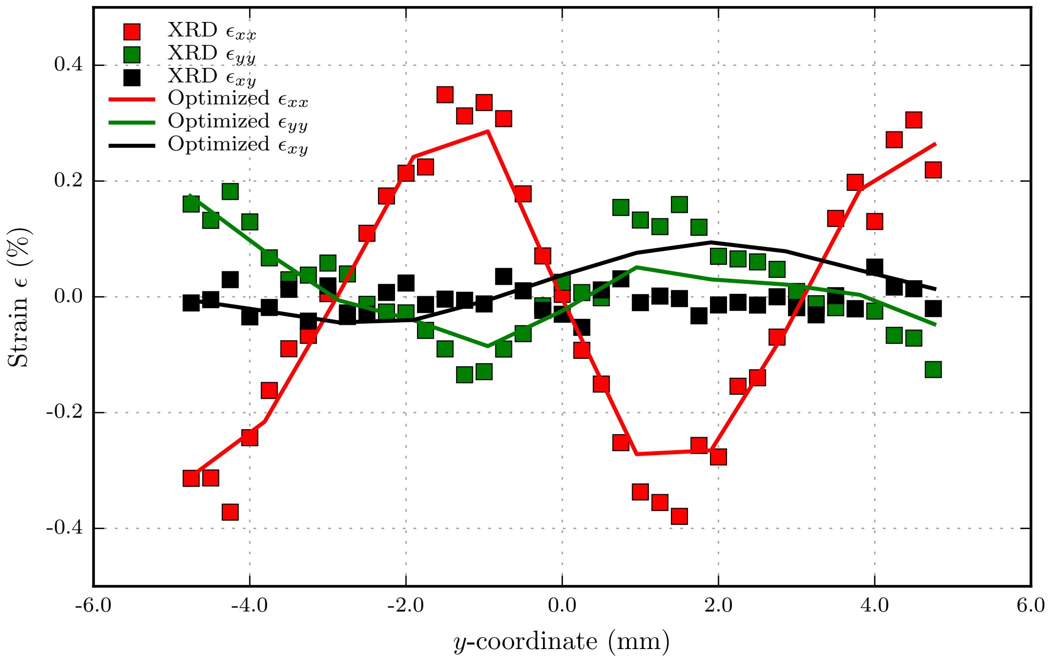

(e) Comparison of XRD ε^{e} and Optimized ε^{e} Along $x = 0$

Figure 4.10 AA7075 XRD Measurements With Added Zeros Comparing $\varepsilon^{\mathrm{e}}_{xx}$ Optimization Results

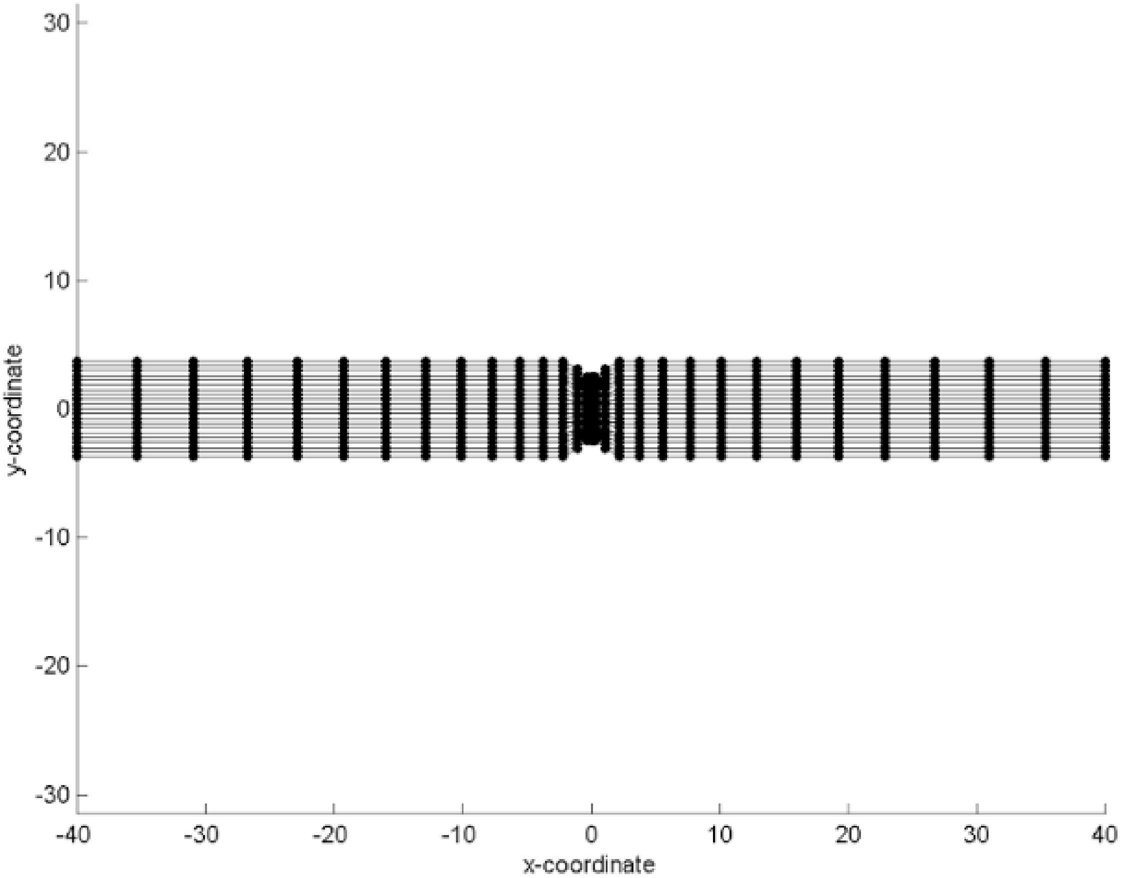

Figure 4.11 Mesh Used for Ti-64 Continuum Dislocation Calculations

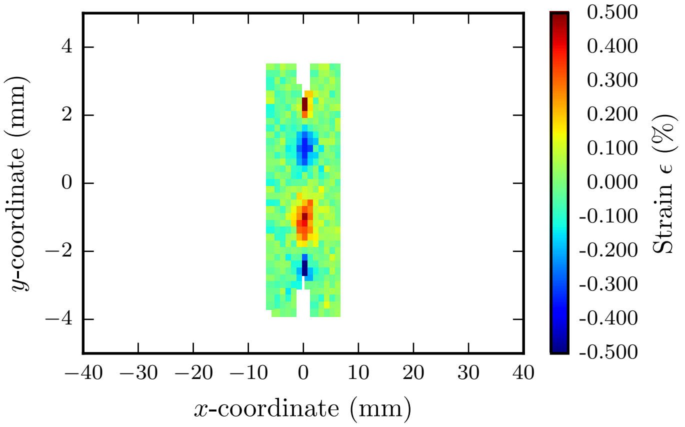

(a) $\varepsilon^{\mathrm{e}}_{xx}$ Measurements

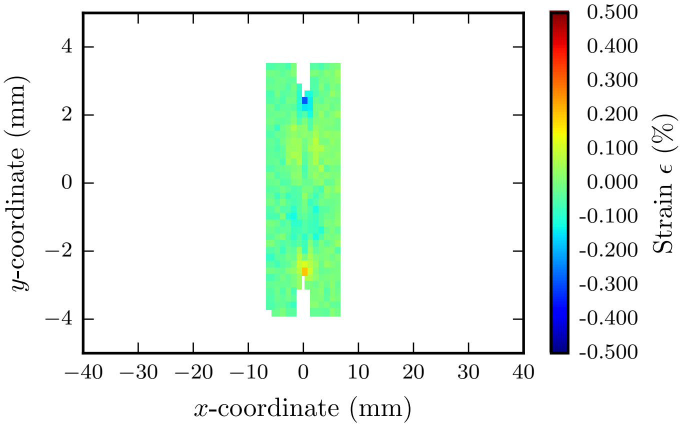

(b) $\varepsilon^{\mathrm{e}}_{yy}$ Measurements

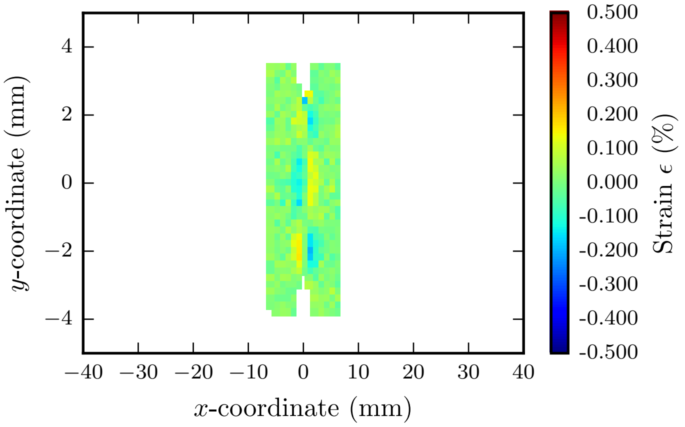

(c) $\varepsilon^{\mathrm{e}}_{xy}$ Measurements

Figure 4.12 Ti-64 XRD Measurements

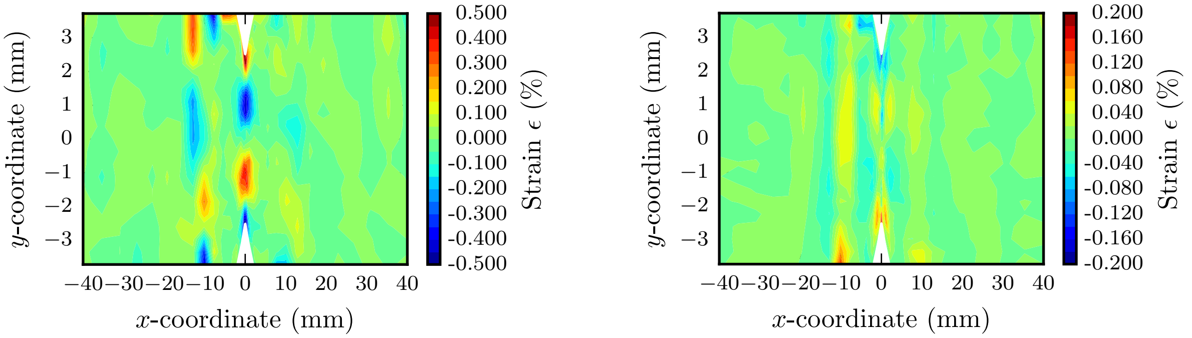

(a) Optimized $\varepsilon^{\mathrm{e}}_{xx}$

(b) Optimized $\varepsilon^{\mathrm{e}}_{yy}$

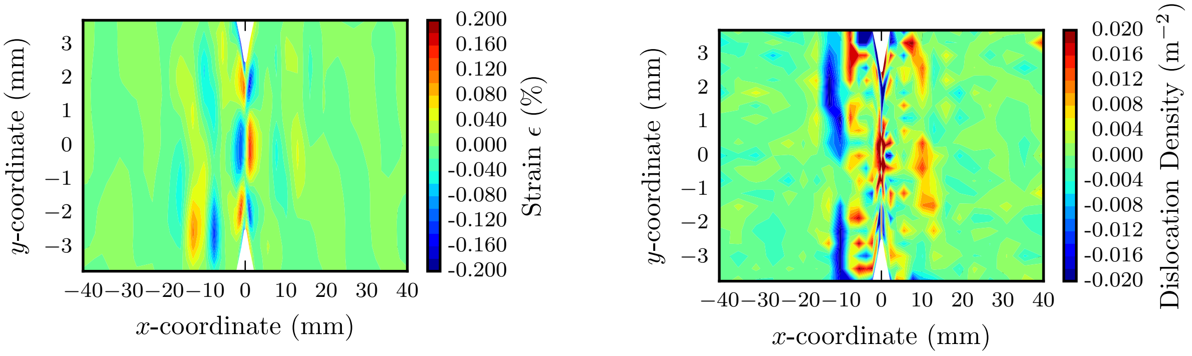

(c) Optimized $\varepsilon^{\mathrm{e}}_{xy}$

(d) Optimized $\tilde{\alpha}_{13}$ Distribution

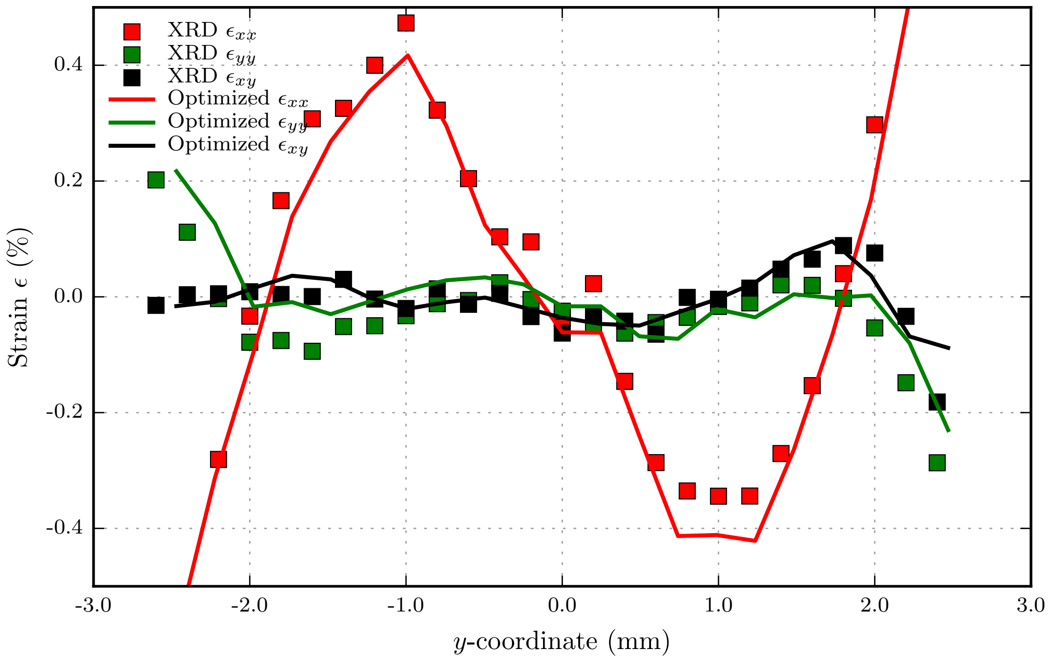

(e) Comparison of XRD ε^{e} and Optimized ε^{e} Along $x = 0$

Figure 4.13 Ti-64 XRD Measurements Optimization Results

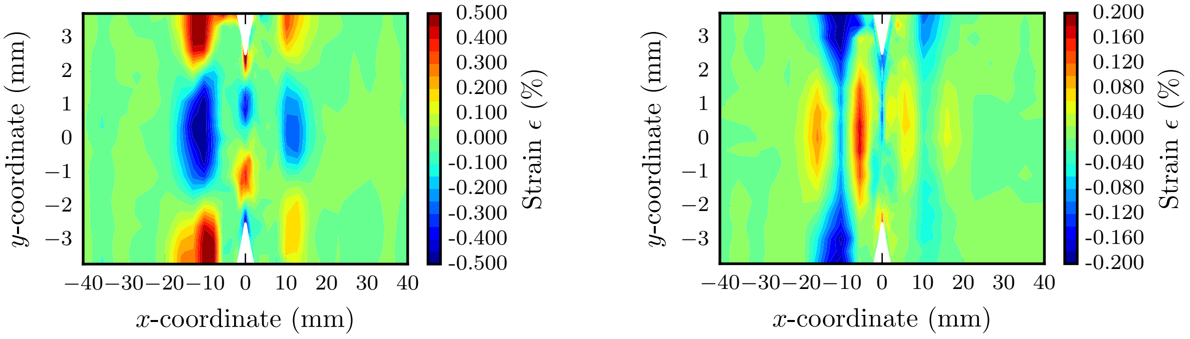

(a) Optimized $\varepsilon^{\mathrm{e}}_{xx}$

(b) Optimized $\varepsilon^{\mathrm{e}}_{yy}$

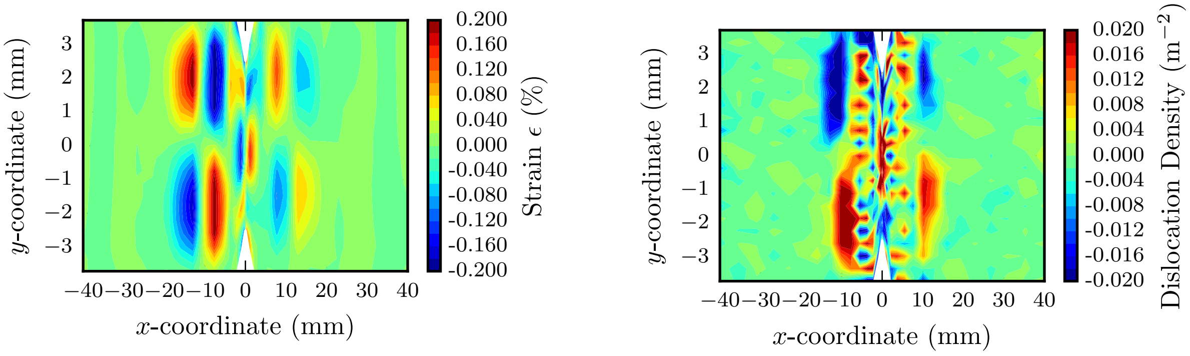

(c) Optimized $\varepsilon^{\mathrm{e}}_{xy}$

(d) Optimized $\tilde{\alpha}_{13}$ Distribution

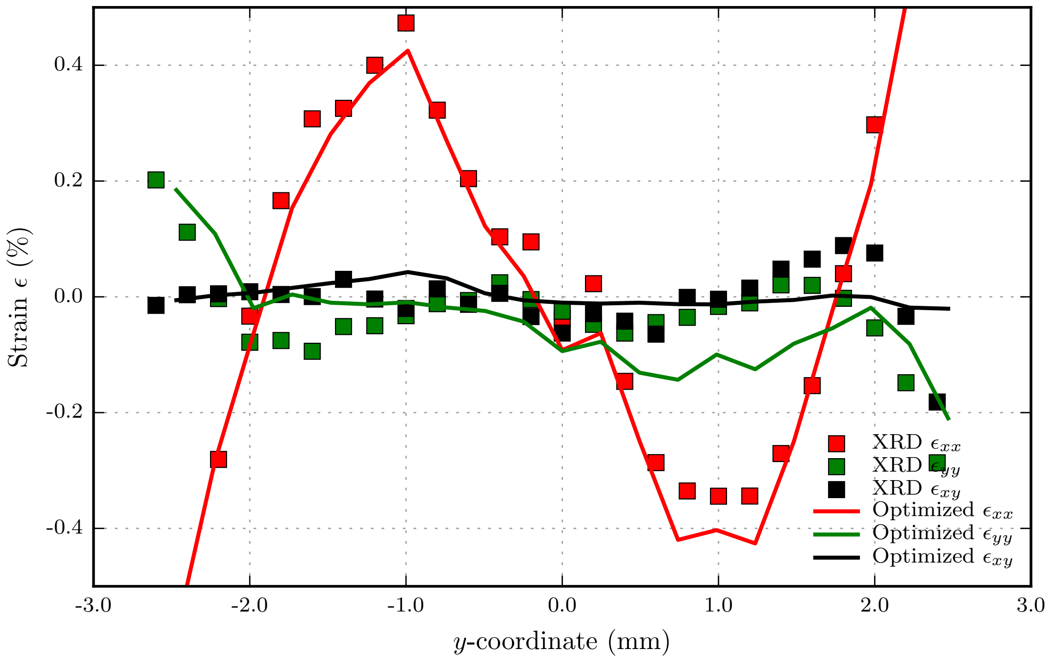

(e) Comparison of XRD ε^{e} and Optimized ε^{e} Along $x = 0$

Figure 4.14 Ti-64 XRD Measurements Comparing $\varepsilon^{\mathrm{e}}_{xx}$ Only Optimization Results

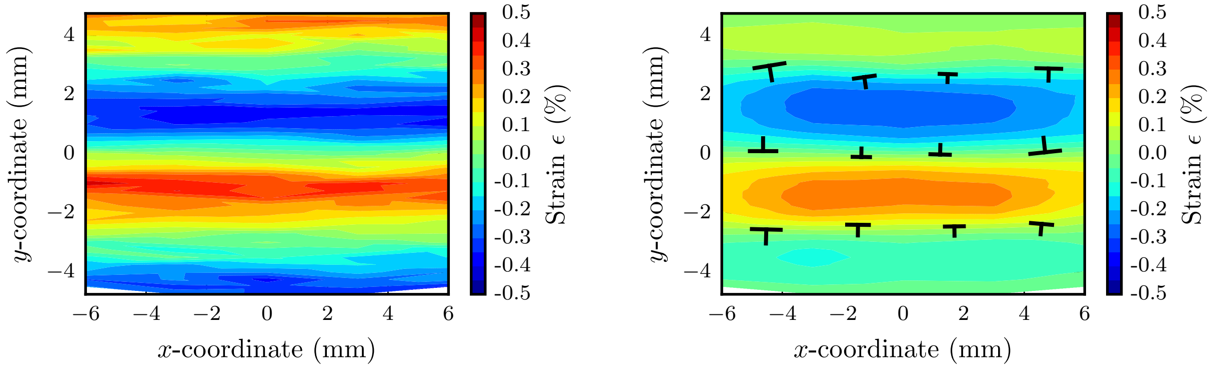

(a) XRD Measured $\varepsilon^{\mathrm{e}}_{xx}$

(b) Optimized $\varepsilon^{\mathrm{e}}_{xx}$

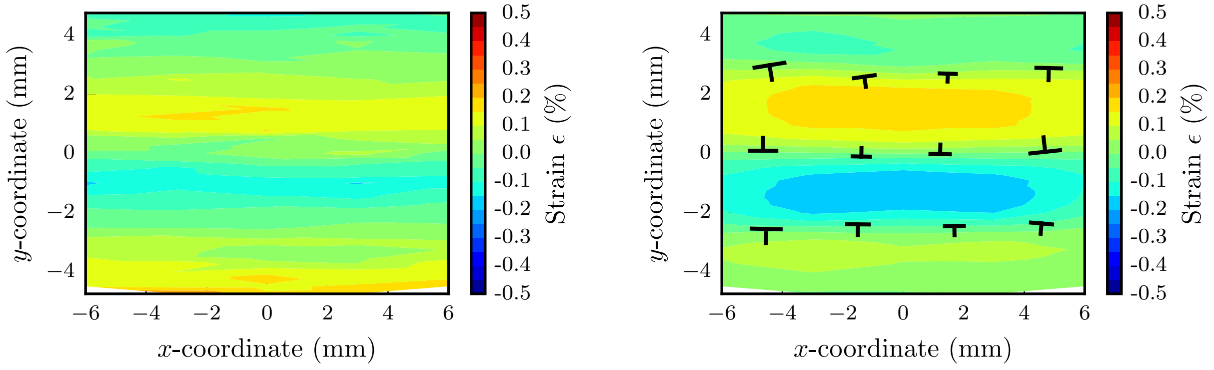

(c) XRD Measured $\varepsilon^{\mathrm{e}}_{yy}$

(d) Optimized $\varepsilon^{\mathrm{e}}_{yy}$

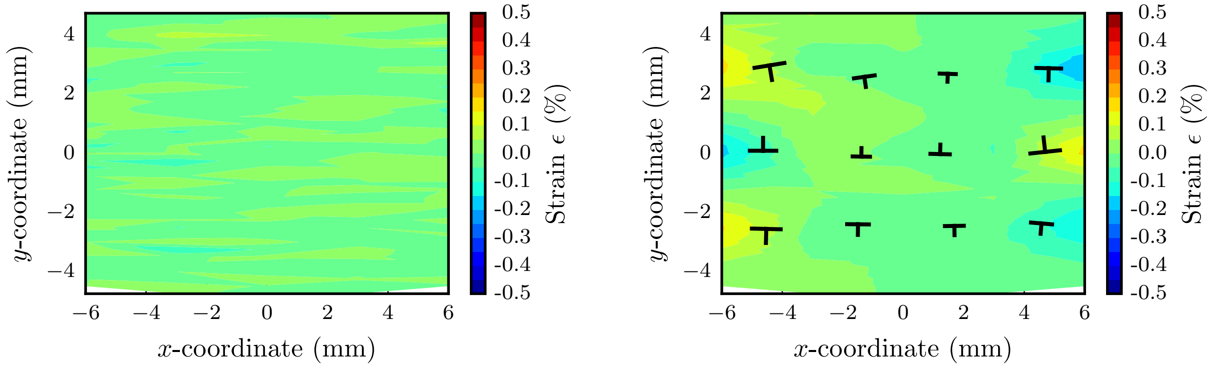

(e) XRD Measured $\varepsilon^{\mathrm{e}}_{xy}$

(f) Optimized $\varepsilon^{\mathrm{e}}_{xy}$

Figure 4.15 AA7075 Discrete Dislocation Optimization Results

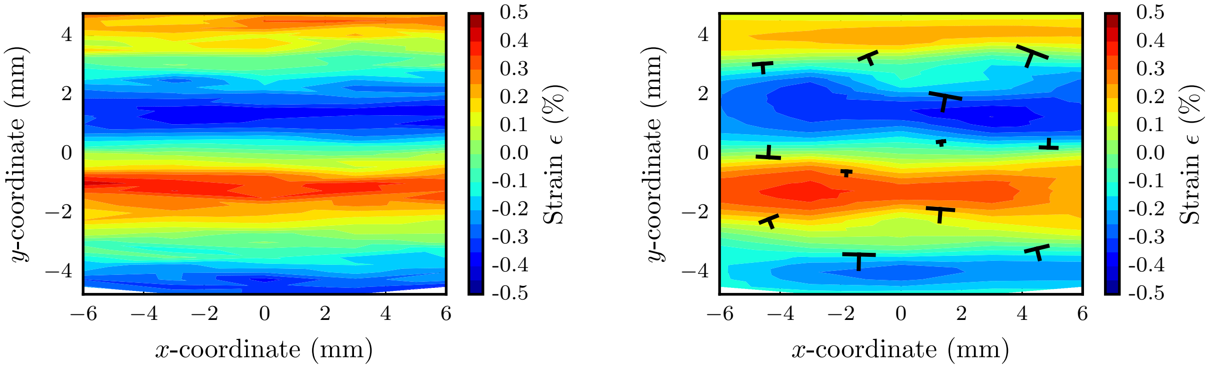

(a) XRD Measured ε^{e}_{xx} (b) Optimized ε^{e}_{xx}

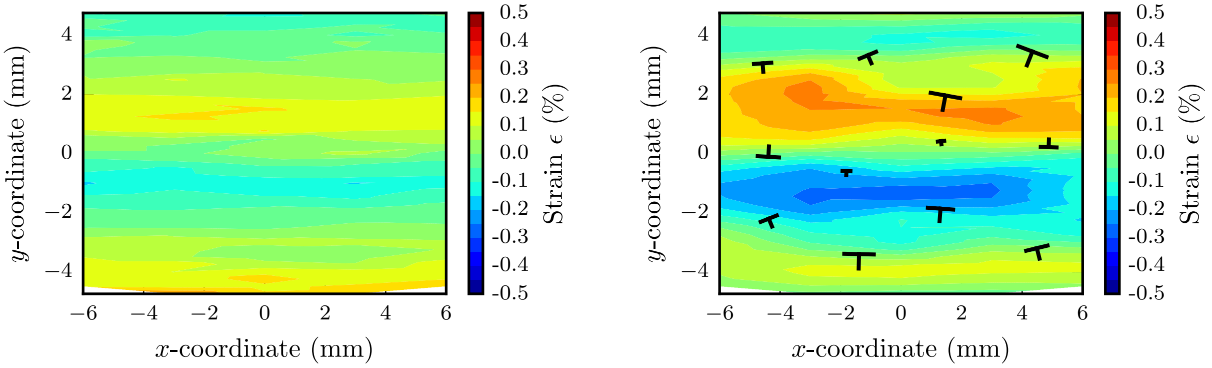

(c) XRD Measured ε^{e}_{yy} (d) Optimized ε^{e}_{yy}

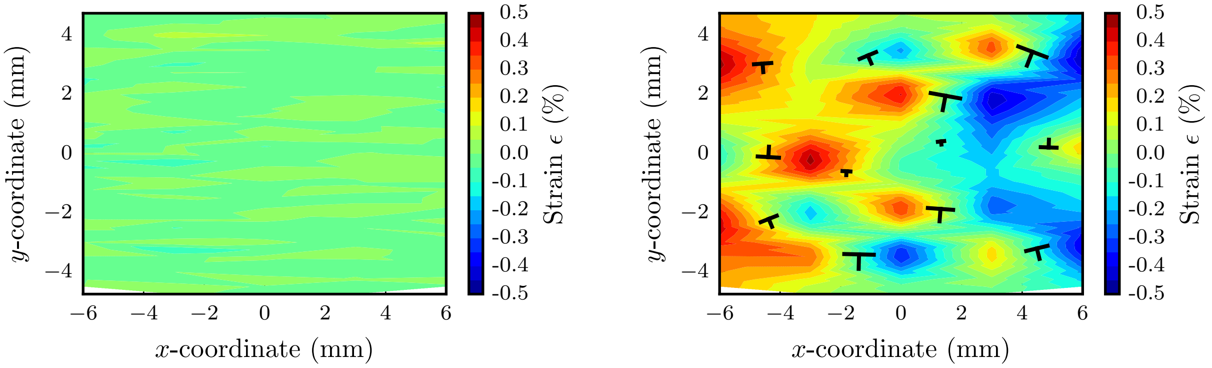

(e) XRD Measured ε^{e}_{xy} (f) Optimized ε^{e}_{xy}

Figure 4.16 AA7075 Discrete Dislocation Comparing ε^{e}_{xx} Only Optimization Results

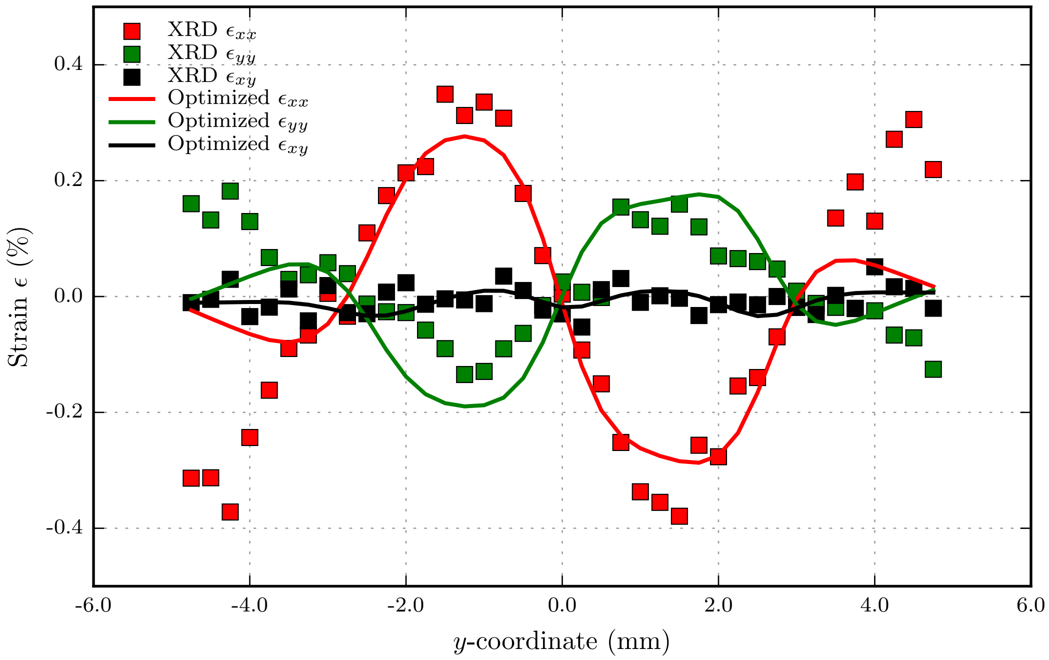

Figure 4.17 Comparison of Measured and Optimized Strains from Discrete Dislocation Optimization

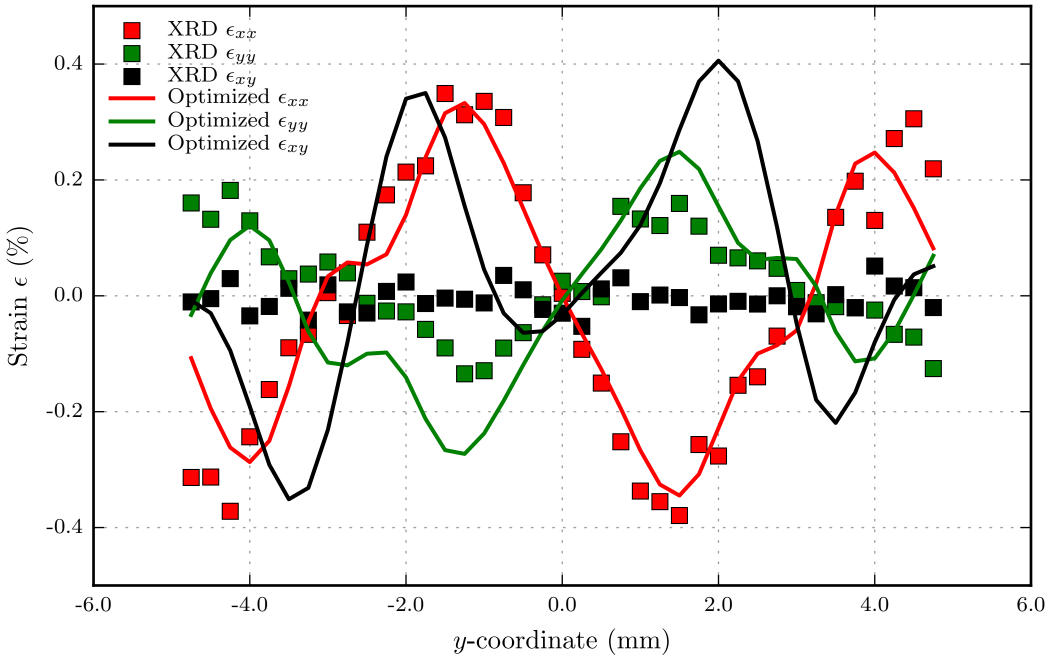

Figure 4.18 Comparison of Measured and Optimized Strains from Discrete Dislocation Optimization, Only ε^{e}_{xx} Compared

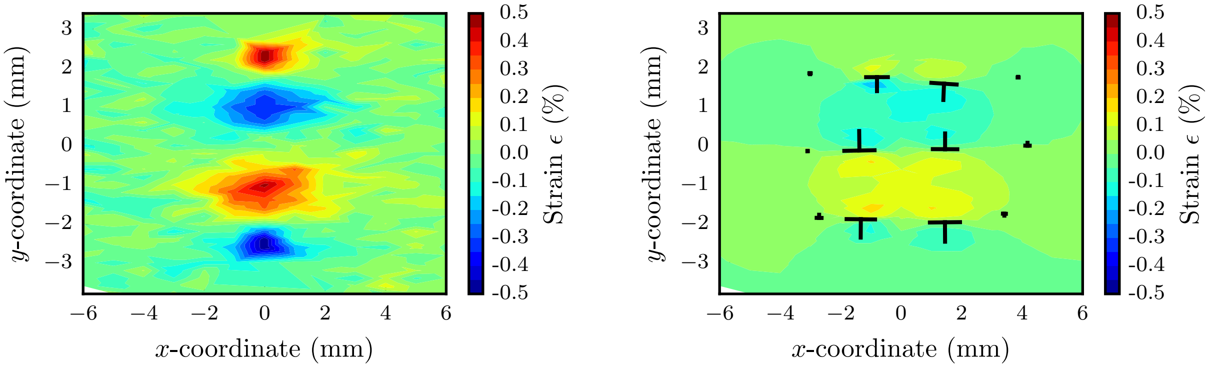

(a) XRD Measured ε^{e}_{xx}

(b) Optimized ε^{e}_{xx}

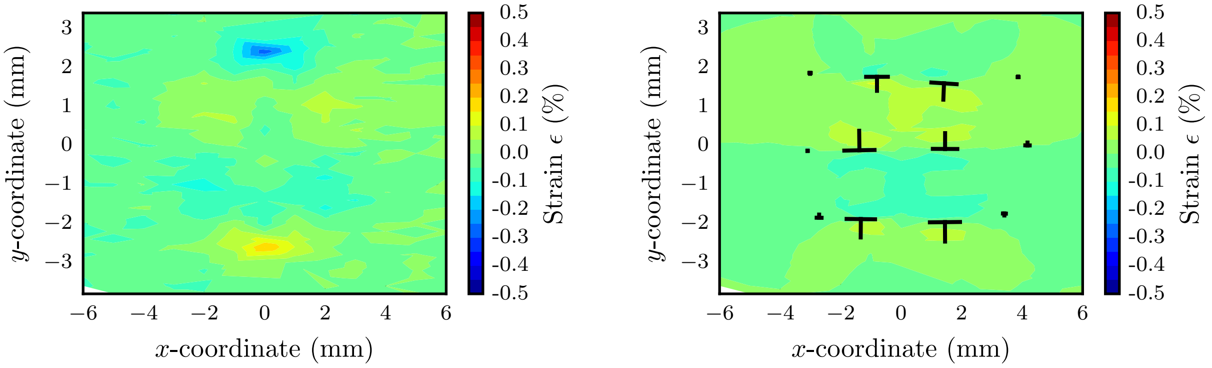

(c) XRD Measured ε^{e}_{yy}

(d) Optimized ε^{e}_{yy}

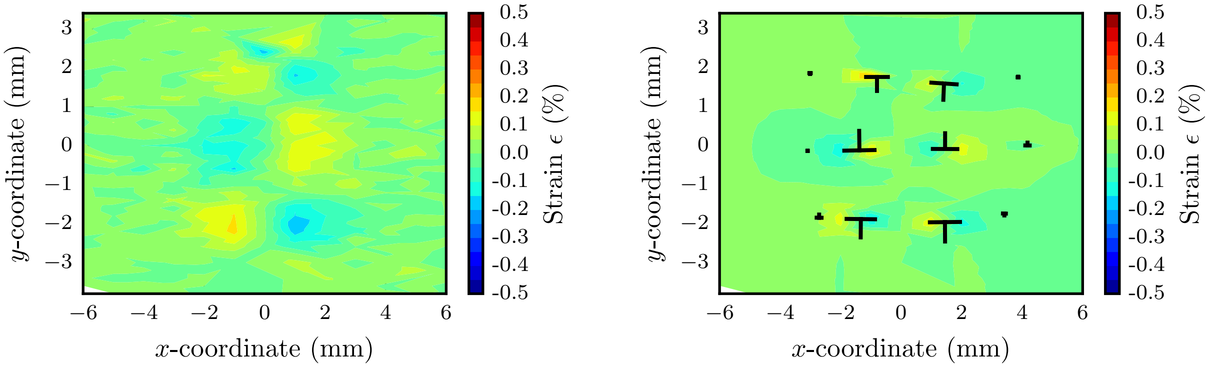

(e) XRD Measured ε^{e}_{xy}

(f) Optimized ε^{e}_{xy}

Figure 4.19 Ti-64 Discrete Dislocation Optimization Results

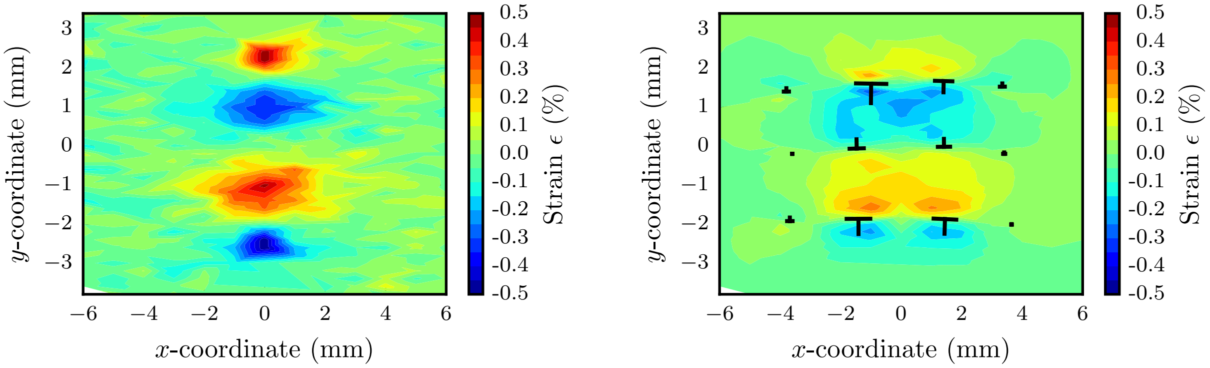

(a) XRD Measured $\varepsilon^{\mathrm{e}}_{xx}$ (b) Optimized $\varepsilon^{\mathrm{e}}_{xx}$

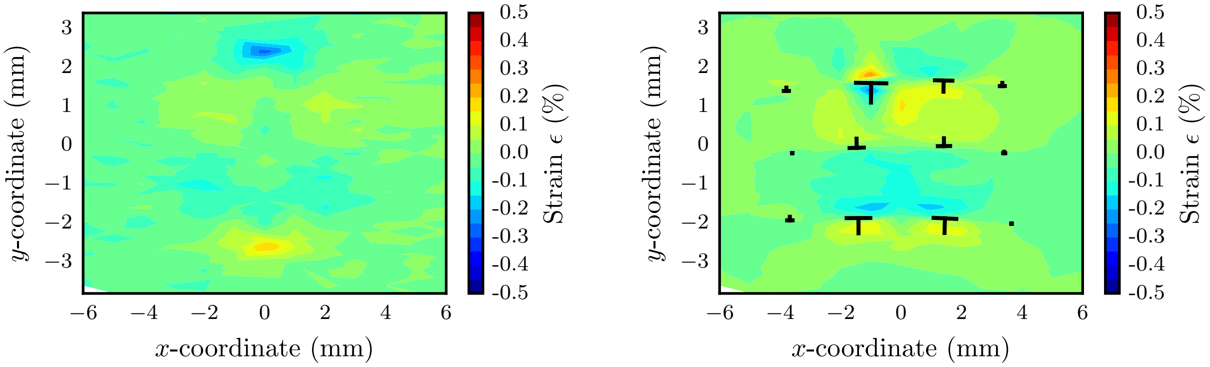

(c) XRD Measured $\varepsilon^{\mathrm{e}}_{yy}$ (d) Optimized $\varepsilon^{\mathrm{e}}_{yy}$

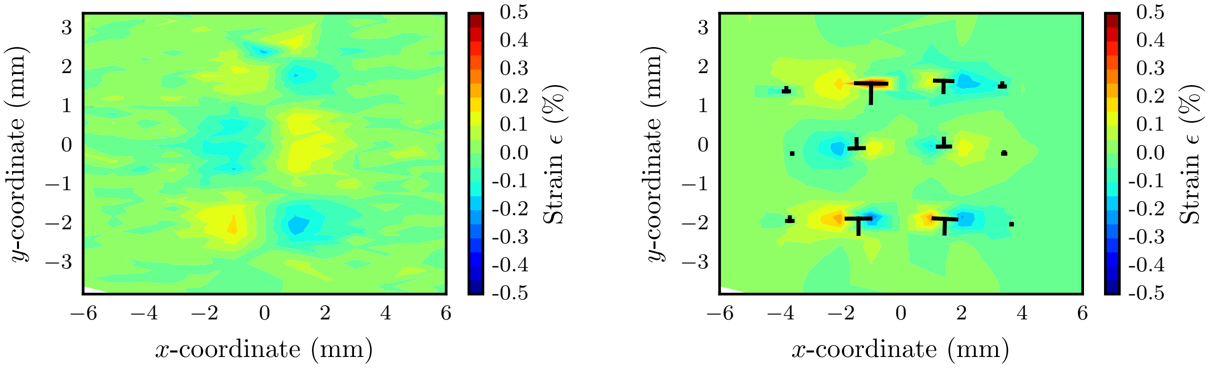

(e) XRD Measured $\varepsilon^{\mathrm{e}}_{xy}$ (f) Optimized $\varepsilon^{\mathrm{e}}_{xy}$

Figure 4.20 Ti-64 Discrete Dislocation Comparing $\varepsilon^{\mathrm{e}}_{xx}$ Only Optimization Results

CHAPTER 5: CONCLUSION

Understanding the residual stress state of processed metals is crucial to accurately predict their fatigue life. Residual stresses, or those present in the absence of applied loads, are caused by arrangements of crystalline defects referred to as dislocations. Dislocations introduce elastic strains into a crystal lattice by shifting material. XRD measurements are ideally suited for measuring residual stresses, since they are non-destructive and only sensitive to elastic strain. A continuum dislocation formulation has been presented that allows elastic strains to be calculated from known dislocation density distributions. This work aims to develop a technique for reducing the number of necessary XRD measurements needed to fully characterize the residual stress state. Instead of measuring the entire strain field, only essential regions that characterize the strain behavior are measured. An inverse problem is then solved to determine an optimal dislocation density distribution whose calculated strain field matches the XRD measurements. The optimal dislocation distribution is then used to solve two BVPs; first for the incompatible elastic distortion field and then for the displacement field. Finally, the stress field in the entire sample can be calculated from the displacement field.

The proposed technique was explored in a four-point bending experiments using both AA7075 and Ti-64 samples. Continuum and discrete techniques for modeling dislocations were explored and compared. The continuum approach is much more complicated to understand and develop in code, however, realistic boundary conditions are respected. The discrete approach is much simpler, but does not enforce proper boundary conditions and can only be used under the plane strain assumption. Thus, a trade off exists that should be explored for each specific application. If a quick answer is desired and strains are low or unimportant near the boundaries, the discrete technique may be a reasonable choice. If an accurate answer is desired and strains are high or important near the boundaries, the continuum technique should be employed.

The ability of a dislocation strain field to match all components of a measured residual strain field provides further evidence that dislocations are the underlying mechanism in residual stress. This concept was verified by determining a dislocation distribution whose strain field matched residual strains predicted from an ABAQUS simulation. The optimal dislocation distribution had a physical parallel to regions of positive and negative edge dislocations. Further optimizations explored the behavior of the technique as measurement locations and strain components were withheld from the objective function. It was determined that so long as enough measurements were taken such that the essence of the strain behavior was captured, the optimization algorithm was able to determine a dislocation arrangement whose calculated strain field reasonably matched the measurements. In the case of bending, multiple strain components that capture the overall behavior of the strain field are necessary to produce a reasonable match between measured and calculated strain across the entire sample.

REFERENCES

[1] Amit Acharya. Personal communication.

[2] Amit Acharya. A model of crystal plasticity based on the theory of continuously distributed dislocations. *Journal of the Mechanics and Physics of Solids*, 49(4):761–784, 2001.

[3] Aerospace Specification Metals Inc. *Aluminum 7075-T6; 7075-T651.*

[4] Aerospace Specification Metals Inc. *Titanium Ti-6Al-4V (Grade 5), Annealed.*

[5] ALCOA. *Alloy 7075 Plate and Sheet.*

[6] J. V. Bernier, N. R. Barton, U. Lienert, and M.P. Miller. Far-field high energy diffraction microscopy: A tool for intergranular orientation and strain analysis. *Journal of Strain Analysis for Engineering Design*, 46(7):527–547, 2011.

[7] William D. Jr. Callister and David G. Rethwisch. *Materials Science and Engineering An Introduction*. John Wiley & Sons, Inc., 111 River Street, Hoboken, NJ 07030-5774, eighth edition, 2010.

[8] P. Chadwick. *Continuum Mechanics: Concise Theory and Problems*. Dover Publications, Inc., Mineola, New York, 1999.

[9] M. Croft, V. Shukla, E.K. Akdoğan, N. Jisrawi, Z. Zhong, R. Sadangi, A. Ignatov, L. Balarinni, K. Horvath, and T. Tsakalakos. In situ strain profiling of elastoplastic bending in ti-6al-4v alloy by synchrotron energy dispersive x-ray diffraction. *Journal of Applied Physics*, 105:093505, 2009.

[10] Bob. He. *Two-Dimensional X-Ray Diffraction*. John Wiley & Sons, Inc., 111 River Street, Hoboken, NJ 07030-5774, 2009.

[11] A.K. Head, S.D. Howison, J.R. Ockendon, and S.P. Tighe. An equilibrium theory of dislocation continua. *SIAM Review*, 35(4):580–609, 1993.

[12] R. Keivani, M. Jahazi, T. Pham, A. R. Khodabandeh, and M. R. Afshar. Predicting residual stresses and distortion during multisequence welding of large size structures using fem. *The International Journal of Advanced Manufacturing Technology*, 73(1):409–419, 2014.

[13] Ekkehart Kröner. General continuum theory of dislocations and proper stresses. *Archive for Rational Mechanics and Analysis*, 4:273–334, 1960.

[14] Ekkehart Kröner. On the physical reality of torque stresses in continuum mechanics. *International Journal of Engineering Science*, 1(2):261–278, 1963.

[15] Gerd Lütjering and James C. Williams. *Titanium*. Springer Science+Business Media, New York, NY, second edition, 2007.

[16] Kurt M. Marshek and Robert C. Juvinall. *Fundamentals of Machine Component Design*. John Wiley & Sons, Inc., 111 River Street, Hoboken, NJ 07030-5774, 4th edition, 2006.

[17] I.C. Noyan and J.B. Cohen. *Residual Stress*. Springer Science+Business Media, New York, NY, 1987.

[18] Bing Pan, Kemao Qian, Huimin Xie, and Anand Asundi. Two-dimensional digital image correlation for in-plane displacement and strain measurement: A review. *Measurement Science and Technology*, 20(6):062001, 2009.

[19] E.C. Reed and J.A. Viens. The influence of surface residual stress on fatigue limit of titanium. *Journal of Engineering for Industry - Transactions of the ASME*, 82(1):76–78, 1960.

[20] Anish Roy and Amit Acharya. Finite element approximation of field dislocation mechanics. *Journal of the Mechanics and Physics of Solids*, 53(1):143–170, 2005.

[21] Hiroyuki Sasahara. The effect on fatigue life of residual stress and surface hardness resulting from different cutting conditions of 0.45%c steel. *International Journal of Machine Tools and Manufacture*, 45(2):131–136, 2005.

[22] Michael A. Sutton, Jean-José Orteu, and Hubert W. Schreier. *Image Correlation for Shape, Motion and Deformation Measurements*. Springer Science+Business Media, New York, NY, 2009.

[23] G.A. Webster and A.N. Ezeilo. Residual stress distributions and their influence on fatigue lifetimes. *International Journal of Fatigue*, 23(1):375–383, 2001.

[24] Johannes Weertman. *Dislocation Based Fracture Mechanics*. World Scientific Publishing Co. Pte. Ltd., 5 Toh Tuck Link, Singapore 596224, 1996.

[25] P.J. Withers and H.K.D.H. Bhadeshia. Residual stress part 1 - measurement techniques. *Materials Science and Technology*, 17(4):355–365, 2001.

APPENDIX A: XRD STRAIN CALCULATION PYTHON CODE

```python
import numpy as np
import numpy.linalg as la
from scipy.optimize import leastsq

########################################################################################################
# User Inputs
########################################################################################################
dark_path                 = '/media/kswartz92/Swartz/chess/ti64_notched/1081/ff/ff_02650.ge2'
data_path                 = '/media/kswartz92/Swartz/chess/ti64_notched/1091/ff/ff_02660.ge2'
detector_dist             = 4261.26         # pixels
true_center               = [1021.42, 1027.24] # [row, column] of detector image center in pixels (shifted by 1 for python index)
E                         = 113800          # elastic modulus (MPa)
v                         = 0.342           # poisson's ratio
radius                    = 500             # ring radius in pixels
dr                        = 25              # half of ring width in pixels
err_max                   = 0.5             # 2 norm of error / 2 norm of data
min_amp                   = 200             # minimum acceptable peak amplitude
two_theta_0               = 0.11661487      # unstressed two_theta value
num_vecs                  = 360             # number of diffraction vectors to fit peaks
dgamma                    = np.radians(0.1) # size of azimuthal patch analyzed in each peak fit

########################################################################################################
# Functions
########################################################################################################


def ge2_reader(path, header_size=4096, image_size=2048):
    FID        = open(path, 'r')
    image_1d   = np.fromfile(FID, dtype=np.uint16)
    FID.close()

    num_images = (image_1d.shape[0] - header_size) / image_size**2
    images     = np.array(image_1d[header_size:].reshape(num_images,image_size,image_size), dtype=float)

    return images
```

```python
def gaussian(x, param):
    peakCtr, fwhmL, fwhmR, amp = param

    xL        = x[x<=peakCtr]
    NLG       = (xL-peakCtr)**2
    DLG       = 2*(fwhmL)**2
    LG        = amp*np.exp(-NLG/DLG)
    xR        = x[x>peakCtr]
    NRG       = (xR-peakCtr)**2
    DRG       = 2*(fwhmR)**2
    RG        = amp*np.exp(-NRG/DRG)

    return np.hstack([LG,RG])

def residualsG(param, x, y):
    return y - gaussian(x, param)

def get_peak_fit_indices(peak, ctr=0.5, lo=0.2, hi=0.8):
        peakCtr   = int(round(len(peak)*ctr))
        loCut     = int(round(len(peak)*lo ))
        hiCut     = int(round(len(peak)*hi ))

        return peakCtr, loCut, hiCut

def fitPeak(x, y, peakCtr0, fwhm0=10, amp0=3000):
        param0    = [peakCtr0, fwhm0, fwhm0, amp0]
        param_opt = leastsq(residualsG, param0, args=(x, y), full_output=1)[0]
        fit       = gaussian(x, param_opt)
        err       = la.norm( residualsG(param_opt, x, y), 2.0) / la.norm(y, 2.0)

        return fit, param_opt, err

def RemoveBackground(x, y, loCut, hiCut):
        x_bg      = np.concatenate([ x[x<loCut], x[x>hiCut] ])
        y_bg      = np.concatenate([ y[x<loCut], y[x>hiCut] ])
        coeff     = np.polyfit(x_bg, y_bg, 1.0)
        background = np.polyval(coeff, x)
        yClean    =  y - background

        return yClean, background
```

```
########################################################################################################
# Strain Calculation
########################################################################################################

# read in dark image
dark_image                 = DataReader.ge2_reader(dark_path)

# average dark images
if len(dark_image.shape) > 1:
    dark_image             = np.mean(dark_image, axis=0)

# read in detector image
image                      = DataReader.ge2_reader(data_path)[0] # only using first image
image                     -= dark_image                     # subtract dark image

# generate coordinates of each pixel and calculate radius and vector angle
x, y                       = np.meshgrid(np.arange(image.shape[1], dtype=float), np.arange(image.shape[0],
     dtype=float))
x                         -= true_center[1]
y                         -= true_center[0]
rad                        = np.sqrt( x**2 + y**2 ) # covert x,y coordinates into r,omega coordinates
gamma                      = np.arctan2(y, x)       # covert x,y coordinates into r,omega coordinates

# initialize storage arrays
vec_gamma                  = np.linspace(-np.pi+(dgamma/2), np.pi-(dgamma/2), num=num_vecs)
two_theta                  = np.zeros(num_vecs)
peak_amps                  = np.zeros(num_vecs)
peak_errs                  = np.zeros(num_vecs)

# loop through each diffraction vector
for i_vec in range(num_vecs):

    # grab slice of detector pixels that are within domega of desired omega
    img_slice                = image[np.abs(gamma-vec_gamma[i_vec]) < dgamma]
    r_slice                  =   rad[np.abs(gamma-vec_gamma[i_vec]) < dgamma]

    # grab section of slice that is within dr of ring radius
    img_slice                =  img_slice[np.abs(r_slice-radius) < dr]
    r_slice                  =    r_slice[np.abs(r_slice-radius) < dr]

    # sort selected pixels values by radial coordinate
```

```
    sorted_indices            = np.argsort(r_slice)
    sorted_r                  =  r_slice[sorted_indices]
    sorted_peak               = img_slice[sorted_indices]

    # fit peak to sorted selected pixel values
    ctr_ind, lo_ind, hi_ind   = PeakFitting.get_peak_fit_indices(sorted_peak)
    peak_bg_rm, _             = PeakFitting.RemoveBackground(sorted_r, sorted_peak, sorted_r[lo_ind],
        sorted_r[hi_ind])
    peak_fit, p_opt, err      = PeakFitting.fitPeak(sorted_r, peak_bg_rm, sorted_r[ctr_ind])

    # calculate 2 theta
    opp                       = p_opt[0]
    adj                       = detector_dist
    two_theta[i_vec]          = np.arctan(opp/adj)

    # store peak amplitude and relative error
    peak_amps[i_vec]          = p_opt[3]
    peak_errs[i_vec]          = err

# determine which points to use in analysis
use                       = np.ones((num_vecs), dtype=bool)
use[peak_errs > err_max]  = False
use[peak_amps < min_amp]  = False

theta_0                   = two_theta_0 / 2
theta                     = two_theta / 2

# only use peak fits that met filtering criteria
vec_gamma                 = vec_gamma[use]
theta                     = theta[use]

# true strain definition
normal_strains            = np.log( np.sin(theta_0) / np.sin(theta) )

# strain rosette equation
A                         = np.zeros((vec_gamma.shape[0], 3))
A[:, 0]                   = (1+np.cos(2*vec_gamma)) / 2
A[:, 1]                   = (1-np.cos(2*vec_gamma)) / 2
A[:, 2]                   = np.sin(2*vec_gamma)
rhs                       = normal_strains / np.cos(theta)**2 # project snormal strains onto sample x1-x2 plane
exx, eyy, exy             = la.lstsq(A, rhs)[0] # solve linear least squares problem
```

APPENDIX B: DISCRETE DISLOCATION STRAIN CALCULATION PYTHON CODE

```
import numpy as np


def get_image_dis(free_surface, xc, yc, b, t):

   # orientation and location of free surface
   coord, surf_loc = free_surface

   # vertical free surface
   if coord == 'x':
      xi          = 2*surf_loc - xc
      yi          = yc
      bi          = b
      ti          = np.pi - t

   # horizontal free surface
   if coord == 'y':
      xi          = xc
      yi          = 2*surf_loc - yc
      bi          = b
      ti          = -t

   return xi, yi, bi, ti



def superpose_strain_field(exx, eyy, exy, xc, yc, b, t, x, y, mat_props):

      # unpack material properties
      E, G, v     = mat_props

      # calculate components in dislocation coordinate system (rotate coordinates by theta)
      x1        =  np.cos(t)*(x-xc) + np.sin(t)*(y-yc)
      x2        = -np.sin(t)*(x-xc) + np.cos(t)*(y-yc)
```

```
        # calculate strain components
        e11       = ( (G*b) / (2*np.pi*E*(1-v)) ) * ( ( (x1**2*x2)*(2*v**2-1*v-3) ) + ( (x2**3)*(2*v**2+v-1) )
             ) / ( (x1**2+x2**2)**2 )
        e22       = ( (G*b) / (2*np.pi*E*(1-v)) ) * ( ( (x1**2*x2)*(2*v**2+3*v+1) ) + ( (x2**3)*(2*v**2+v-1) )
             ) / ( (x1**2+x2**2)**2 )
        e12       = (   b  / (4*np.pi*(1-v)) ) * ( x1*(x1**2-x2**2) ) / ( (x1**2+x2**2)**2 )

        # rotate coordinates by -theta
        exx      += (e11*np.cos(t)**2) + (e22*np.sin(t)**2) - (2*e12*np.sin(t)*np.cos(t))
        eyy      += (e11*np.sin(t)**2) + (e22*np.cos(t)**2) + (2*e12*np.sin(t)*np.cos(t))
        exy      += ((e11-e22)*np.sin(t)*np.cos(t)) + (e12*(np.cos(t)**2-np.sin(t)**2))

        return exx, eyy, exy



def calculate_strain(params, x, y, free_surfaces, mat_props):
    """ function calculates the superposed elastic stress/strain fields from input discrete dislocations in an
         infinite plate with plane strain assumption

    inputs:
    params             : 1d array with lists of (x-positions, y-positions, Burgers vector maginitudes, and
         orientations) dislocation parameters
    x                  : nd array of x coordinates where stress/strain field is to be calculated
    y                  : nd array of y coordinates where stress/strain field is to be calculated
    free_surfaces      : list of free surfaces (example entry: ['x',4.0])
    mat_props          : list of material properties containing [elastic modulus, shear modulus, poisson's
         ratio]

    outputs:
    exx                : array of xx normal strain values at data points given by x and y arrays
    eyy                : array of yy normal strain values at data points given by x and y arrays
    exy                : array of xy shear strain values at data points given by x and y arrays """

    # unpack parameters
    n_dis       = params.shape[0]//4    # number of dislocations
    xd          = params[0*n_dis : 1*n_dis]
    yd          = params[1*n_dis : 2*n_dis]
    bd          = params[2*n_dis : 3*n_dis]
    td          = params[3*n_dis : 4*n_dis]
```

```
# initialize stress/strain arrays
exx, eyy, exy = np.zeros(x.shape), np.zeros(x.shape), np.zeros(x.shape)

# sum up contribution from each dislocation
for i_dis in range(n_dis):

    # superpose strain field from dislocation
    exx, eyy, exy = superpose_strain_field(exx, eyy, exy, xd[i_dis], yd[i_dis], bd[i_dis], td[i_dis], x, y,
         mat_props)

    # superpose strain fields from image dislocations
    for surface in free_surfaces:

        xi, yi, bi, ti = get_image_dis(surface, xd[i_dis], yd[i_dis], bd[i_dis], td[i_dis])
        exx, eyy, exy = superpose_strain_field(exx, eyy, exy, xi, yi, bi, ti, x, y, mat_props)

return exx, eyy, exy
```